Temperature Dependent Angle-Resolved Photoemission Study of the Valance Bands of Single Crystal Iridium

by

Hassane Darhmaoui

A Thesis Presented to the

FACULTY OF THE COLLEGE OF GRADUATE STUDIES

KING FAHD UNIVERSITY OF PETROLEUM & MINERALS

DHAHRAN, SAUDI ARABIA

In Partial Fulfillment of the
Requirements for the Degree of

MASTER OF SCIENCE

In

PHYSICS

June, 1990

Order Number 1355732

Temperature dependent angle-resolved photoemission study of the valence bands of single crystal iridium

Darhmaoui, Hassane, M.S.

King Fahd University of Petroleum and Minerals (Saudi Arabia), 1990

U·M·I
300 N. Zeeb Rd.
Ann Arbor, MI 48106

TEMPERATURE DEPENDENT ANGLE-RESOLVED PHOTOEMISSION STUDY OF THE VALENCE BANDS OF SINGLE CRYSTAL IRIDIUM

BY

HASSANE DARHMAOUI

A Thesis Presented to the

FACULTY OF THE COLLEGE OF GRADUATE STUDIES

KING FAHD UNIVERSITY OF PETROLEUM & MINERALS

DHAHRAN, SAUDI ARABIA

In Partial Fulfillment of the

Requirements for the Degree of

MASTER OF SCIENCE

In

PHYSICS

JUNE 1990

KING FAHD UNIVERSITY OF PETROLEUM & MINERALS

DHAHRAN, SAUDI ARABIA

COLLEGE OF GRADUATE STUDIES

This thesis, written by **HASSANE DARHMAOUI** *under the direction of his Thesis Advisor, and approved by his Thesis Committee, has been presented to and accepted by the Dean of the College of Graduate Studies, in partial fulfillment of the requirements for the degree of* **MASTER OF SCIENCE IN PHYSICS.**

Thesis Committee

O. B. Dabbousi
Chairman (Professor O. B. DABBOUSI)

Recep Avci
Member (Dr. R. AVCI)

Member (Dr. M. A. SALIM)

Department Chairman

Dean College of Graduate Studies

Date : 25-6-90

بسم الله الرحمن الرحيم

"و قل رب ارحمهما كما ربياني صغيراً"

Dedicated to :

My mother and To the memory of my father.

ACKNOWLEDGEMENTS

Praise to Allah, Lord of the words, the Almighty, with whose gracious help it was possible to accomplish this work.

Acknowledgement is due to King Fahd University of Petroleum and Minerals for support of this research.

I wish to express my sincere thanks and gratitude to Dr. Z. Hussain, my thesis committee chairman, and Professor O. Dabbousi, my thesis committee co-chairman, for their encouragement, guidance and assistance in carrying out this work.

My thanks are due to Dr. R. Avci. and Dr. M. Salim, my thesis committee members, for their invaluable suggestions and comments.

I am thankful for the help and assistance in my experimental work to Dr. M. Salim and Mr. P. Sobingsobing. I also wish to thank Dr. A. Al-Haidari, my academic advisor, for his continuous support, Dr. A. Hussein for his help in the computer plotting programmes, Dr. J. Noffke and Dr. L. Fritsche for supplying the theoretical data on Iridium energy-bands.

Finally I wish to thank my family and all my friends for their support and encouragement during my stay at KFUPM.

TABLE OF CONTENTS

LIST OF TABLES

FIGURES CAPTIONS

خلاصة الرسالة

اسم الطالب الكامـــل : دغماوي حسن

عنوان البحـــث : دراسة تاثير درجة الحرارة على الألكترونات المنبعثة من نطاق التكافؤ لبلورات الأريديوم الأحادية بإستخدام التحليل الزاوي لمطيافية الألكترونات .

مجـــال التخصص : فيزياء .

تاريخ الدرجة العلمية : ٢ يونيو ١٩٩٠م .

لقد تم إستعمال التحليل الزاوي لمطيافية الألكترونات للحصول على أطياف نطاق التكافؤ لبلورات الأريديوم الأحادية عند درجات حرارية مختلفة (من ١٢٠ - ٦٣٠درجة كلفن) لزوايا إنبعاث عمودية وغير عمودية على سطح العينة بإستخدام الأشعة السينية المنبعثة من قطب الماغنسيوم (Mg_{K_α}) . وقد تم إستعمال انحلال زاوي بمقدار ±١ر١هذه الأطياف أظهرت إعتماداً قوياً على درجة الحرارة مع تغيرات كبيرة عند درجة ١٢٠ كلفن . وقد أستخدم نموذج شفشيك Shevchik لإستخلاص مركبات الإنبعاث المباشر والغير المباشر من المعلومات التي تم الحصول عليها عند درجات الحرارة المختلفة. و لقد تبين أن هذا النموذج لايعطي تماسكا تاما بحيث ان مركبة الإنبعاثات غير المباشرة تختلف عن كثافة الحالات لمادة الا ريديوم . أما مركبات الإنبعاثات المباشرة فلا تزال تتضمن بعضا من شدة الإنبعاثات غير المباشرة ؛ لكن التغيرات الطيفية من مركبات الإنبعاث المباشر تتفق إتفاقاً شبه كمي مع توقعات نموذج الإنبعاث المباشر البسيط الذي يفترض ألكترون حر في حالة التشتت النهائية وعنصر مصفوفي ثابت .

درجة الماجستير في العلوم
جامعة الملك فهد للبترول والمعادن
الظهران - المملكة العربية السعودية
يونيو ١٩٩٠م

THESIS ABSTRACT

NAME OF STUDENT : *HASSANE DARHMAOUI*

TITLE OF STUDY : *TEMPERATURE DEPENDENT ANGLE-RESOLVED PHOTOEMISSION STUDY OF THE VALENCE BANDS OF SINGLE CRYSTAL IRIDIUM.*

MAJOR FIELD : *PHYSICS*

DATE OF DEGREE : *JUNE, 1990*

Temperature dependent angle-resolved x-ray photoemission valence bands spectra have been obtained from Iridium (111) single crystal using Mg K_α excitations and emission both normal and non-normal to the surface. The temperature was varied from 120K to 630K and a high angular resolution of $\leq \pm 1.1^\circ$ was used. These spectra show strong temperature dependence with dramatic changes occuring at 120K. Data obtained at different temperatures are used to deconvolute direct transition (DT) and non-direct transition (NDT) components via Shevchik's model. This model is found not to give full self consistency. The NDT components are different from the density of states and the DT components still include some residual intensity due to NDT. However, the spectral variations of the DT components agree semi-quantitatively with the predictions of a simple bulk DT model assuming free electron final state dispersion and constant matrix elements.

MASTER OF SCIENCE DEGREE

KING FAHD UNIVERSITY OF PETROLEUM AND MINERALS

Dhahran , Saudi Arabia

June 1990

CHAPTER I

INTRODUCTION

The energy band structure, i.e., the wave-vector dependence of the electronic energies $E(\vec{k})$, is one of the most fundamental information about the electronic structure of solids. The band structure description is very useful when discussing the basic physical and chemical properties of solids that involves valence-band electrons such as electrical conductivity, magnetism, optical properties, etc...

Angle-resolved photoelectron spectroscopy (AR-PES) has proven to be the technique of choice for studying the valence-band structure of solids [1,2] . With AR-PES, it is possible to deduce both energy and directional, or momentum, information through an analysis of the ejected photoelectrons. The angle-resolved photoelectron experiment, consists of irradiating the sample under investigation with nearly monoenergetic photons and measuring kinetic energies of the electrons that are ejected along specific directions. In this way information on both : electron's energy and its wave-vector, $\vec{k}$, (the latter being related to the propagation direction) are obtained.

Photons with an energy of about 1 Kev are well suited (as will be discussed in chapter 2) for the mapping of the energy bands of solids using this AR-PES technique. This method has been shown to provide a direct method for mapping the valence electronic levels of transition metal single crystals [3,4,5]. Moreover, thermal disorder effects are found to play an important role in this energy regime. Thus, even at room temperature strong temperature dependences has been observed in photoemission spectra [4,5].

The temperature dependence of the valence band photoemission spectra at high photon energies was first discussed theoretically by Shevchik [7]. Shevchik showed that vibrational effects weaken the wave-vector conservation requirement and that phonon disorder almost completely destroys $\vec{k}$ conservation in the X-ray photoelectron spectroscopy (XPS) regime in most materials at room temperature. Thus, XPS spectra would have two contributions from direct ($\vec{k}$ conserving) transitions (DT) and from phonon-assisted, non-direct, transitions (NDT). Shevchik based his analysis on the theory of X-ray diffraction and the assumption of uncorrelated lattice vibrations, whereby the atoms are assumed to move independently of one another. The relative magnitude of the DT and NDT components are related to the Debye-Waller factor, W(T), of the element under investigation. The Debye-Waller factor is defined as:

$$W(T) = \exp\left(-\Delta k^2 < U^2(T) >\right) \qquad (1\text{-}1)$$

Here $\Delta k = g$, and g is the magnitude of the reciprocal lattice vector involved in the DT and $<U^2(T)>$ is the temperature dependent mean squared atomic displacement.

The resultant expression for the photocurrent is:

$$I(E,T) = W(T)I_{DT}(E) + (1 - W(T))I_{NDT}(E), \qquad (1\text{-}2)$$

where I_{DT} is the DT component of the spectrum and I_{NDT} is the NDT component of the photocurrent. Both components are assumed to be independent of temperature. Equation (1-1) indicates that the Debye Waller factor decreases in magnitude as the Temperature is increased. Thus, from equation (1-2) we see that the NDT contribution to the total photocurrent increases with temperature and that the magnitude of the Debye Waller factor provides an estimate of the fraction of the transitions which are direct.

Thermal effects in photoemission were first observed experimentally by Williams et al [8]. Nowadays it is well established that an increase in the specimen temperature leads to enhancement of phonon-assisted NDT signal

Hussain et al, R.C White et al have used the Shevchik model to extract empirical DT and NDT components in the emission spectra of a Tungsten single crystal in specific direction [4,9,10]. In fitting their data, a model incorporating free electron final states and constant matrix elements proved to be quite successful in describing the directional and photon

energy dependence of the DT components in Angle-resolved X-ray photoelectron spectroscopy (AR-XPS) spectra from the valence bands of Tungsten. However, in later work [10] on the same element they found that the temperature dependence of the NDT components is not as simple as assumed in earlier analysis. This has lead to the inclusion of some of the NDT intensity in the DT component.

Thus, from these works it may be concluded that the NDT process is the principal limiting factor of energy band mapping in this energy regime. Hence, the investigation of the temperature dependence in other materials seems to be indicated. Higher energy and angular resolutions as well as decreasing angular acceptance broadening effects in photoemisson spectra seem to be required to permit much more precise determination of the energy, E, and the wave-vector $\vec{k}$ [10]. Wide temperature range including low temperatures are also indicated for better separation of DT and NDT components. At such low temperatures NDT effects are expected to almost totally disappear.

The work presented in this thesis, follows these earlier works in studying temperature dependence of valence bands of a new element. In this thesis we use an Iridium(111) single crystal and the AR-XPS technique. We vary the temperature of the sample from 120K to 630K. The liquid Nitrogen cooling is used to achieve the low temperatures reported in this thesis. Angular resolution is also improved in our work by mounting a micro-channel plate in the spectrometer in such a way that all trajectories of the mean emission direction are within an angle $\leq \pm 1.1°$.

For this type of experiments, samples must be microscopically clean and in single crystal form. These requirements are achieved by a combination of pre-analysis preparation and in-situ cleaning. The orientation and alignment of the sample axes are also critical. In our experiment, we use Low energy electron diffraction (LEED) technique to check sample surface ordering and as a first approximation orienting of the sample axes. The alignment of the sample axes with respect to the micro-channel plate (which is the same as the entry lens axis of the analyzer) was calibrated using X-ray photoelectron diffraction (XPD) patterns of the Ir4f core-level signals as a function of polar and azimuthal angles.

In this thesis we start with a presentation, in chapter II, of the different models used in the data analysis. The DT model of Braid et al [11,12] for interpreting AR-PES in the XPS regime is presented. In this model rigorous wave-vector and energy conservations are required for allowed transitions. Shevchik's model is used for the extraction of the DT and NDT components from spectra. Recent theoretical study by Sagurton [13,14] in which correlated lattice vibration are included and sums over all phonon modes are made, is also summarized. The different experimental techniques used in our experiment, i.e. AR-PES, LEED, XPD, and their underlying principles, are presented briefly in chapter III. The experimental procedures used as well as the preparation of Ir(111) sample, its cleaning and characterization, are explained in chapter IV. The data acquisition and handling procedures as well as theoretical calculations are explained in chapter V. In chapter VI, the angle-resolved valence-band

spectra, at different temperatures, are presented. The results are correlated with the DT model. The final chapter provides a summary and conclusions drawn from the present work.

CHAPTER II

THEORETICAL BACKGROUND

2.1 INTRODUCTION

2.1.1 Three-step Model:

In order to obtain an approximate correlation between the measured photoelectron energy distribution and the density of electronic states in solids, Berglund and Spicer [15] proposed a "three-step" model. In this model the photoemission process is decomposed into three steps with each step considered as independent.

(*a*) In the first step an electron absorbs the energy of photon of sufficiently high energy and is excited into a final state above the Fermi level.

(*b*) The second step is one of the transport of electrons to the surface. The electrons may undergo inelastic scattering during this transport process which will result in an altering of their energy and momentum.

(*c*) The third step is of the escape of the electrons across the surface barrier into vacuum.

The three-step model has had considerable success in interpreting experimental data. The first step of the model, is treated quantum mechanically, involves excitation of photo-electrons from filled initial states to empty states of higher energy via momentum conserving transitions. When electromagnetic radiation enter a sample, the associated perturbation is given by an interaction Hamiltonian of the form:

$$H' = \vec{A}\cdot\vec{P} + \vec{P}\cdot\vec{A} \qquad (2\text{-}1)$$

where $\vec{A}$ is the electromagnetic vector potential and $\vec{P}$ the linear momentum operator. The surface field term $\vec{P}\cdot\vec{A}$, in H', is usually assumed to be small or zero [16,17]. The perturbation H' can lead to photoexcitation of electrons between initial states Φ_i and final states Φ_f. The probability of excitation is given by Fermi's Golden Rule:

$$P_f \propto \sqrt{E_f}\, |<\Phi_f(\vec{r})|H'|\Phi_i(\vec{r})>|^2\, \delta(E_f(\vec{k}) - E_i(\vec{k}) - h\nu) \qquad (2\text{-}2)$$

where the initial and final states of the electron are taken to be wave functions of the unperturbed solid . The delta function in eq.(2) imposes the energy conservation restriction. The momentum conservation is implicit in the form for E($\vec{k}$) where $\vec{k}$ is the same throughout. Thus, the "internal" energy distribution of the photoexcited electrons can be written as:

$$N_{int}(E,h\nu) \propto \sum_{f,i} \int_{\vec{k}} |<\Phi_f(\vec{r})|H'|\Phi_i(\vec{r})>|^2\, \delta(E_f(\vec{k}) - E_i(\vec{k}) - h\nu)\, \delta(E - E_f(\vec{k}))\, d^3k \qquad (2\text{-}3)$$

All possibilities for an electron to be excited from band $E_i(\vec{k})$ to band $E_f(\vec{k})$ that conserve the momentum, $\vec{k}$, are summed. However, final states with E_f equalling an energy E are selected.

To correlate the internal distribution $N_{int}(E,h\nu)$ with the measurable external energy distribution $N_{ext}(E,h\nu)$ one has to consider the second and the third steps namely, the propagation of the excited electrons to the surface and their escape from the solid into the vacuum. An escape function $T(E_j,\vec{k})$ which describes the probability for an excited electron in the state $E_j(\vec{k})$ to reach the surface and leave the solid is generally introduced [18,19]. Thus:

$$N_{ext}(E,h\nu) = N_{int}(E,h\nu)\, T(E_j,\vec{k}) \qquad (2\text{-}4)$$

In the XPS regime the energies and mean free path are high enough to permit one to assume that the emission involves pure bulk states and to set T = 1.0 for all angles except for grazing angles [20].

2.1.2 Photoelectron energy distribution:

Based on the three-steps model, described above, the general form of the photoelectron energy distribution N(E,hν) is obtained from Eq.(2-4) as:

$$N_{ext}(E,h\nu) \propto \sum_{f,i} \int_{\vec{k}} |<\Phi_f(\vec{r})|H'|\Phi_i(\vec{r})>|^2\, \delta(E_f(\vec{k}) - E_i(\vec{k}) - h\nu)\, \delta(E - E_f(\vec{k}))\, T(E_j,\vec{k})\, d^3k \qquad (2\text{-}5)$$

For energies in the XPS regime and an experimental geometry of finite detection angle, Eq.(2-5) can be written as [20-22]:

$$\int_{\vec{k}_i}\int_{\vec{k}_{f_{obs}}} d^3\vec{k}_i d^3\vec{k}_f \,|<\Phi_f(\vec{r})|\vec{A}\cdot\vec{\nabla}|\Phi_i(\vec{r})>|^2\,\delta(\vec{k}_f-\vec{k}_i-\vec{K}_{h\nu}-\vec{g})\,\delta(E_f-E_i-h\nu)\,\delta(E-E_i) \tag{2-6}$$

where $\vec{A}\cdot\vec{\nabla}$ is the relevant operator for the radiation, $\vec{k}_f$ is the final-state wave vector expressed in an extended zone scheme, $\vec{k}_i$ is the initial-state wave vector expressed in a reduced zone scheme, $\vec{g}$ is a unique bulk reciprocal lattice vector connecting the two wave vectors, $\vec{K}_{h\nu}$ is the wave vector associated with the radiation $|\vec{K}_{h\nu}| = \omega/c$, E_f is the final energy of the excitations as measured inside the crystal and E_i is the initial energy from which excitations occurs. The delta functions represent the requirement of energy and momentum conservations in the excitation process. The wave vector conservation condition contains a $\vec{K}_{h\nu}$ which can be neglected in comparison with the reduced-zone dimensions in experiments at energies below 200 eV. The photon wave vector, $\vec{K}_{h\nu}$, cannot be neglected, however, in typical XPS measurements [3,5]. For example, in the case where excitations energy is ≈ 1.5 keV, $|\vec{K}_{h\nu}| \approx (0.35\text{-}0.40)2\pi/a$ and $|\vec{k}_f| \approx (10)2\pi/a$, where $2\pi/a$ is the approximate size of the Brillouin zone (BZ). Thus $\vec{K}_{h\nu}$ cannot be neglected with respect to $\vec{k}_i$, as $|\vec{k}_i| \leq 2\pi/a$.
The $\vec{k}_f$ integral is taken over observed $\vec{k}_f$ values whose directions span the limited solid angle of the experimental geometry. The integral in $\vec{k}_i$ is over all occupied initial states.

To evaluate Eq.(2-6), or to generate a theoretical photoelectron energy distribution, accurate wave functions for both the initial and the final states are required. While such information in the form of theoretical band

structure calculations, is available for the initial state, the description of the final state represents a major problem, since, in general such calculations are not tested for accuracy or not available. At high excitation energies, however, such as those in XPS, the assumption of a free-electron like final state inside the crystal gives good agreement with experiment.

2.2 DIRECT TRANSITION MODEL:

This model was first proposed by Braid et al [11,12] for interpretation of angle-resolved XPS spectra. In their calculations, rigorous wave-vector and energy conservations conditions are imposed on allowed transitions. The matrix elements, $<\Phi_f(\vec{r})|\vec{A}\cdot\vec{\nabla}|\Phi_i(\vec{r})>$, in Eq.(2-6) were assumed to be constant for all allowed transitions and for a final-state wave function a free-electron like final state was assumed. This assumption is much more valid in the X-ray energy regime.

This model is too simplified, for, it does not include all the physical ingredients of an exact theory. Yet, the model was quite successful in describing the directional and photon energy dependence of DT components in AR-UPS [23], AR-XPS spectra [4,9]. Subsequently , the model has been used to map band structures of metals and semiconductors [9,23,24-26]. In the following subsections we will review some of the important features of this model.

2.2.1 Wave-vector and Energy Conservation

The energy and wave-vector conservations used in the bulk DT model are:

$$E_f = E_i + h\nu \tag{2-7}$$

$$\vec{k}_f = \vec{k}_i + \vec{K}_{h\nu} + \vec{g} \tag{2-8}$$

where various terms have the same meanings as described for Eq.(2-6). The nature of $\vec{k}-$ conservation for a typical XPS transition, is illustrated in Figure(II-1) which shows the Iridium Brillouin Zone, with a scale drawing of a $\vec{k}-$ conserving DT including wave vector $\vec{K}_{h\nu}$.

The finite solid angle of the cone of observation of the electron analyzer distributes the observed $\vec{k}_f$ values over a disk-like region in $\vec{k}$ -space with a radius of $\Delta k_\perp = k_f \tan\Delta\theta = 0.21(2\pi/a)$, where a is the Iridium lattice constant and $2\pi/a$ is the approximate BZ dimension. The disk can then be projected one or more $\vec{g}$ vectors to yield $\vec{k}_i$ that lies within the first Brillouin zone. Thus, the large value of $\vec{k}_f$ in XPS produces some degree of averaging of $\vec{k}_i$ via the finite disk sizes involved.

The magnitude of the excitation wave-vector $\vec{K}_{h\nu}$ for Mg K_α excitation used in our experiment is $0.39(2\pi/a)$, which is clearly non-negligible relative to the BZ dimensions. Its effect, on wave-vector conservation, is included by shifting all points of the $\vec{k}_f$ disk of the observed cone by $(-\vec{K}_{h\nu})$ as shown in Figure (II-1).

DIRECT TRANSITION IN XPS OF IRIDIUM

$$\vec{k}_i + \vec{g} = \vec{k}_f - \vec{K}_{h\nu}$$

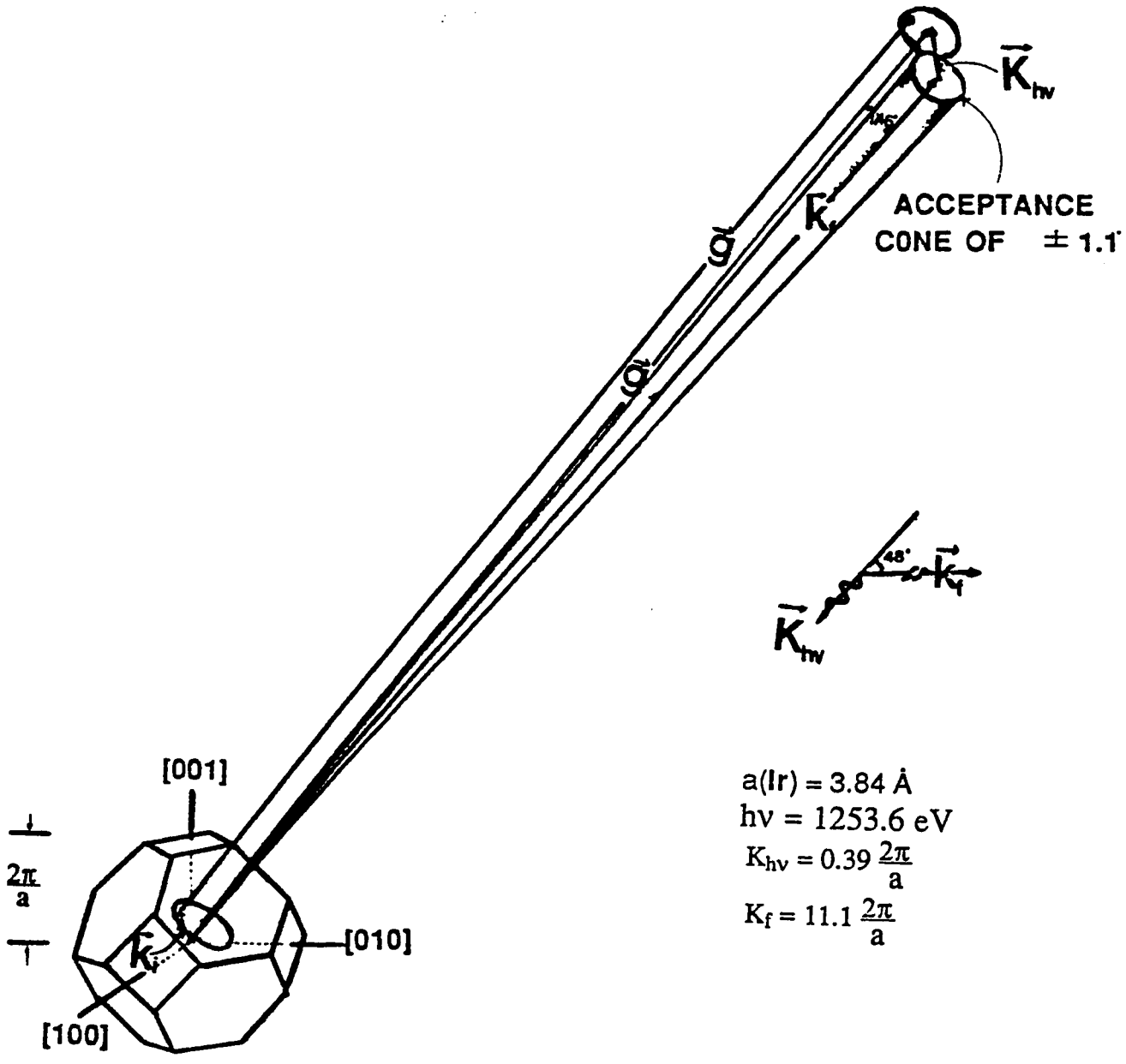

Fig. (II-1): Scale drawing of a $\vec{k}$ – conserving direct transition including photon wave vector $\vec{K}_{h\nu}$

2.2.2 Free-Electron final States:

For the high energies involved in X-ray excitations, the magnitude of $\vec{k}_f$ is very nearly constant over the full spectrum as judged against the BZ dimension within which $\vec{k}_i$ is to be located eventually. This is illustrated in the DT model by the assumption of photo-excited free-electron final state. It follows the free-electron dispersion:

$$E_f(\vec{k}_f) = (\hbar^2/2m^*)\,|\vec{k}_f|^2 + V_0 \qquad (2\text{-}9)$$

where m^* and V_0 are the effective mass and inner potential, respectively, to be determined from the bulk band structure. Equation (2-5) indicates that the excited final state has a parabolic free-electron like band in a constant inner potential V_0. Thus, the measurement of E_f by angle resolved photoemission yields $\vec{k}_f$ from Eq. (2-9) and E_i from Eq. (2-7). Then by Eq. (2-8) $\vec{k}_i$ is obtained since $\vec{K}_{h\nu}$ is known from the experimental geometry and $\vec{g}$ can usually be assessed. Therefore, one can infer E_i to determine the valence band structure in metals. In our study we do the inverse, i.e., we compare the experimental valence-band spectra with theoretical photoelectron energy distribution based on DT model.

2.2.3 Constant Matrix Elements:

In the simple DT model, the matrix elements $<\Phi_f(\vec{r})|\vec{A}\cdot\vec{\nabla}|\Phi_i(\vec{r})>$, are assumed to be constant for all transitions. Matrix-element effects play an important role in determining excitation probabilities. Yet, it is not clear

whether they are significantly important in producing the changes noted in the XPS valence band spectra for single crystals. Experimentally, it has been shown that those matrix elements are not very important in predicting valence band spectra in X-ray excitations [3,5].

2.3 ADVANTAGES OF THE USE OF X-RAYS FOR BAND-STRUCTURE INVESTIGATIONS:

As mentioned in Chapter I, the use of photon energies of $\sim$1 keV for band-structure investigation has some discrete advantages when compared to band mapping in the so-called band-structure regime. In the X-ray regime, the excitation energies are so high that one can assume the final state to be free electron like. This assumption is much more valid than in the case of lower energies. Due to the large excitation energies, is the negligible effects of surface scattering or surface Umklapp processes in this regime. An additional advantage, result of the large mean free path involved in XPS excitations, is a very small smearing effect in $\vec{k}_f$. This effect limits the wave function to a region of the order of the mean free path (Λ_e) along its propagation direction. From the uncertainty principle this will cause a smearing dictated by $\Delta k_f \approx 1/(2\Lambda_e)$. That is, a $\vec{k}_f$ disk such as that in Figure (II.1) will come to have an added thickness Δk_f along $\vec{k}_f$. In XPS such smearing is not very large compared to BZ dimensions. It has been verified that such smearing along the propagation direction does not significantly alter the predicted XPS spectra [3,5] while such effect is important in low energies (UPS) spectra.

2.4 THERMAL DISORDER AND NON-DIRECT TRANSITIONS:

2.4.1 Thermal effects on photoemission:

As the temperature of a sample is increased, several effects may occur in photoemission:

(a) Thermal disorder could weaken the $\vec{k}$ selection rule to cause transitions from other regions of the BZ to occur. These transitions, called Phonon-assisted NDT were first pointed by Shevchik [7] to become extremely important for most materials at room temperature in the XPS regime.

(b) The lattice dilation with temperature, coupled with more complex electron -phonon interaction, may alter the initial and final state energies and wave functions [14]. This effect does not seriously alter the energy of the electronic transition since the phonon energy is only a few tens of millielectron-volts (meV)[7,27].

It should be noted that, to date, there is no fully quantitative model involving all temperature effects. Only some different approaches have been applied to describing one or more of these effects [14]. In our study we will focus on the destruction of $\vec{k}$ conservation during photoexcitation through phonon-assisted NDT.

2.4.2 Non Direct Transition Model:

The direct transition wave-vector conservation requirement Eq.(2-8), can be written as:

$$\vec{k}_f - (\vec{k}_i + \vec{K}_{h\nu}) = \vec{g} \qquad (2\text{-}10)$$

this can be viewed, in a simple one-electron picture, as a diffraction law:

$$\Delta\vec{k} = \vec{k}_f - \vec{k}_i' = \vec{g} \qquad (2\text{-}11)$$

where the initial state, described by the momentum vector $\vec{k}_i'$, is the incident beam. $\vec{k}_i'$ involves the photon momentum $\vec{K}_{h\nu}$ and the bound electron (e.g. valence electron) crystal momentum $\vec{k}_i$ ($\vec{k}_i' = \vec{k}_{h\nu} + \vec{k}_i$). The final state of momentum $\vec{k}_f$ describes the scattered beam. Hence, the AR-P may be viewed as a scattering process. It follows, therefore, that the intensity of the direct transition peak should be expected to exhibit a temperature dependence governed by the Debye-Waller factor ($W(T) = \exp(-\Delta k^2 < U^2 >)$), as well as a dependence on energy, due to the change in $\Delta\vec{k} = \vec{g}$, with changing hν. Furthermore, the non-direct transition process in photoemission should correspond closely to X-ray thermal diffuse scattering (TDS) [28]. This correspondence between X-ray diffraction and AR-P is manifested in the photoexcitation matrix element which is found to be proportional to Eq.(2-12) below with the assumption of uncorrelated motion of the atoms [7].

$$\sigma_{if}(\vec{k}_f)\{[1 - W(T)] + W(T)\sum_{g}\delta(\Delta\vec{k} - \vec{g})\} \qquad (2\text{-}12)$$

here $\sigma_{if}(\vec{k}_f)$ is the photoinization cross section. The delta function in the second term correspond to the usual $\vec{k}$ conservation in crystals. This term is reduced in strength by the Debye-Waller factor. The first term in the above expression, however, has no restriction on momentum conservation and thus correspond to non-direct transition. Thus relating Eq. (2-12) to the total photoelectron energy distribution described by Eq. (2-6), the total photocurrent can be written as:

$$I(E,T) = W(T)\, I_{DT}(E) + [1 - W(T)]\, I_{NDT}(E) \qquad (2\text{-}13)$$

where I_{DT} is the DT component of the spectrum and I_{NDT} is the NDT component (both components are assumed independent of temperature). From this equation it is clear that the Debye-Waller factor represents the fraction of transitions that are direct. In the XPS regime, where the momentum of the photoelectron is large, the fraction of direct transitions is expected to be less because of the large $\vec{g}$ and resultant lower value of the Debye-Waller factor. The magnitude of the thermal displacements $<U^2(T)>$ and the Debye-Waller factors W(T) at different temperatures (from liquid Helium temperature (T=4K) to 1000K) for Iridium in the XPS regime for both Al K_α and Mg K_α and in the UPS regime for the Helium II line are given in Table 1. Inspection of this table shows that for Mg K_α radiation, Iridium has a large Debye-Waller factor, of 0.84, at liquid Nitrogen temperature (77K). Thus 84% of the transitions from Ir are expected to be direct. At room temperature, the fraction of DT is 65%. For higher temperatures NDT are dominants.

TABLE 1

Average thermal displacement ($<U^2>$) ; and Debye Waller factor W(T) for, Iridium, $4K \leq T \leq 1000K$ in XPS and UPS ranges*

T(K)	$<U^2>$ (10^{-18} cm^2)	AlKα (1486.6eV) W(T)	MgKα (1253.6eV) W(T)	HeII(40.8eV) W(T)
4	0.0450	0.84	0.87	0.995
77	0.0556	0.81	0.84	0.994
100	0.0596	0.79	0.82	0.993
120	0.0685	0.77	0.80	0.992
150	0.0811	0.73	0.77	0.991
200	0.0978	0.69	0.73	0.989
250	0.1171	0.64	0.68	0.987
295	0.1342	0.60	0.65	0.985
300	0.1362	0.59	0.64	0.985
350	0.1564	0.55	0.60	0.983
400	0.1764	0.50	0.56	0.981
450	0.1950	0.47	0.53	0.979
500	0.2167	0.43	0.50	0.977
550	0.2384	0.40	0.46	0.974
600	0.2601	0.37	0.43	0.972
650	0.2817	0.33	0.39	0.970
700	0.3034	0.31	0.37	0.968
750	0.3251	0.29	0.35	0.966
800	0.3467	0.26	0.33	0.963
850	0.3666	0.24	0.31	0.961
900	0.3882	0.22	0.28	0.959
950	0.4097	0.21	0.27	0.957
1000	0.4309	0.19	0.25	0.954

*The Debye temperature of Ir is taken from Ref. [33]: $\Theta_D = 420$ K.

In comparing experimental spectra, obtained at a particular temperature, with DT theory, one has to take into account phonon-assisted NDT effects. This is done by extracting the DT component from experimental spectra at two different temperatures, T_1 and T_2, using Eq. (2-13). The DT experimental component is then compared to the DT intensity as calculated by the DT model. Alternatively theoretical curves could be generated as follows: the intensities as predicted by the DT model ($I_{DT}(E)$) are multiplied by W(T) and added to the total density of state ($I_{DOS}(E)$) after the later has been weighted by (1-W(T)):

$$I_{theory}(E,T) = W(T)\, I_{DT}(E) + [1 - W(T)]\, I_{DOS}(E) \qquad (2\text{-}14)$$

In such calculations the DT intensities and the density of states are normalized such that the number of points in the first BZ used in calculating the total density of states is taken to equal the number of directions within this acceptance solid angle leading to DT emission.

2.4.3 Sagurton model:

Shevchik's model, discussed in the previous paragraph, assumed uncorrelated lattice vibrations. This model results in the simple form of the temperature dependence of the photocurrent given by Eq. (2-13). In Sagurton's model [14,32] however, correlated lattice vibrations are included, with summation over all phonon modes, in the calculation of the photoemission current. Correlated lattice vibrations are expected to

introduce NDT intensity that is strongly peaked about the simple DT point in the reduced zone. This is analogous to thermal diffuse scattering in X-ray diffraction [28-30] or electron diffraction [31] by crystal lattice. A synopsis of the unpublished results of Sagurton is given in references [14] and [32]. Here, only the final results of this model are given.

The inclusion of correlated lattice vibrations leads to a different overall form for Eq. (2-13).

$$I(E,T) = W(T)\, I^0_{DT}(E) + I^0_{NDT}(E,T) \qquad (2\text{-}15)$$

where the NDT component $I^0_{NDT}(E,T)$ is now temperature dependent and only the DT component is weighed by the Debye-Waller factor.
According to these results that are based on a more accurate treatment of phonon-induced NDT in photoemission, the empirical extraction of DT and NDT components from experimental data through Eq. (2-13) implies that the components thus obtained be related to the pure DT and NDT components according to the more complex relations:

$$I_{DT}(E) = I^0_{DT}(E) + I^0_{NDT,1}(E,T) \qquad (2\text{-}16)$$

$$I_{NDT}(E) = I^0_{NDT,2}(E,T) \qquad (2\text{-}17)$$

$$I^0_{NDT}(E) = I^0_{NDT,1}(E,T) + I^0_{NDT,2}(E,T) \qquad (2\text{-}18)$$

Thus the DT component, via Eq. (2-13), may contain a residual NDT contribution and the component I_{NDT} may be only part of the total NDT contribution to the photoelectron spectrum.

CHAPTER III

THE AR-PES, LEED AND XPD TECHNIQUES

3.1 AR-PES AND ENERGY BAND MAPPING :

3.1.1 Principle :

Photoelectron spectroscopy (PES) is an important analytical tool in the field of surface analysis. It has been used widely in the investigation of the electronic and atomic structure of solids and solid surfaces [1,16,34,35]. In essence, the technique involves analysis of electrons ejected from matter by incident radiation. The ejected electrons are the so-called photoelectrons. The kinetic energy (KE) of the photoelectrons is given by the Einstein relation [36] :

$$h\nu = BE + KE \qquad (3\text{-}1)$$

Where hν is the energy of the exciting photon and BE is the binding energy, or the ionization energy, of the electron in the material. Thus, with appropriate photon energies and analyzer settings, any bound electronic state can in principle be observed and studied.

Collecting the photoelectrons in some specified direction with respect to some fixed axes is called angle-resolved photoelectron spectroscopy (AR-PES), with this method one can study the spatial anisotropy of the emitted electrons. Traditionally, PES and AR-PES have been divided into two energy regimes: Ultraviolet photoelecton spectroscopy (UPS) and angle resolved ultraviolet photoelectron spectroscopy (AR-UPS). In this regime photon sources in the energy range of 5-40 eV from discharge lamps are used. X-ray photoelectron spectroscopy (XPS) and angle resolved photoelectron X-ray spectroscopy (AR-XPS) use higher energy sources such as Al K_α and Mg K_α, X-ray tubes in 1.2 - 1.5 keV energy range.

In some angle resolved experiments, the relative spatial orientations of the sample and the analyzer are important. Thus, either the sample or the analyzer must be able to rotate about at least one well defined axis. A typical experimental geometry is shown in Figure (III-1). Photons, of energy hv propagate toward the sample along direction $\vec{K}_{h\nu}$, making an angle $0_{h\nu}$ with the surface of the sample. The emitted photoelectrons are detected in direction $\vec{k}$ defined by the analyzer which subtends a solid angle Ω_0. The direction $\vec{k}$ makes an electron emission, or polar, angle 0 relative to the surface, an azimuthal angle φ and an angle α with the incidence direction of the photon.

For the experiment presented in this thesis, the photon source and the analyzer have a fixed value of the angle α of 48°. The variation in angle is thus achieved by a rotation of the sample about an axis parallel to the

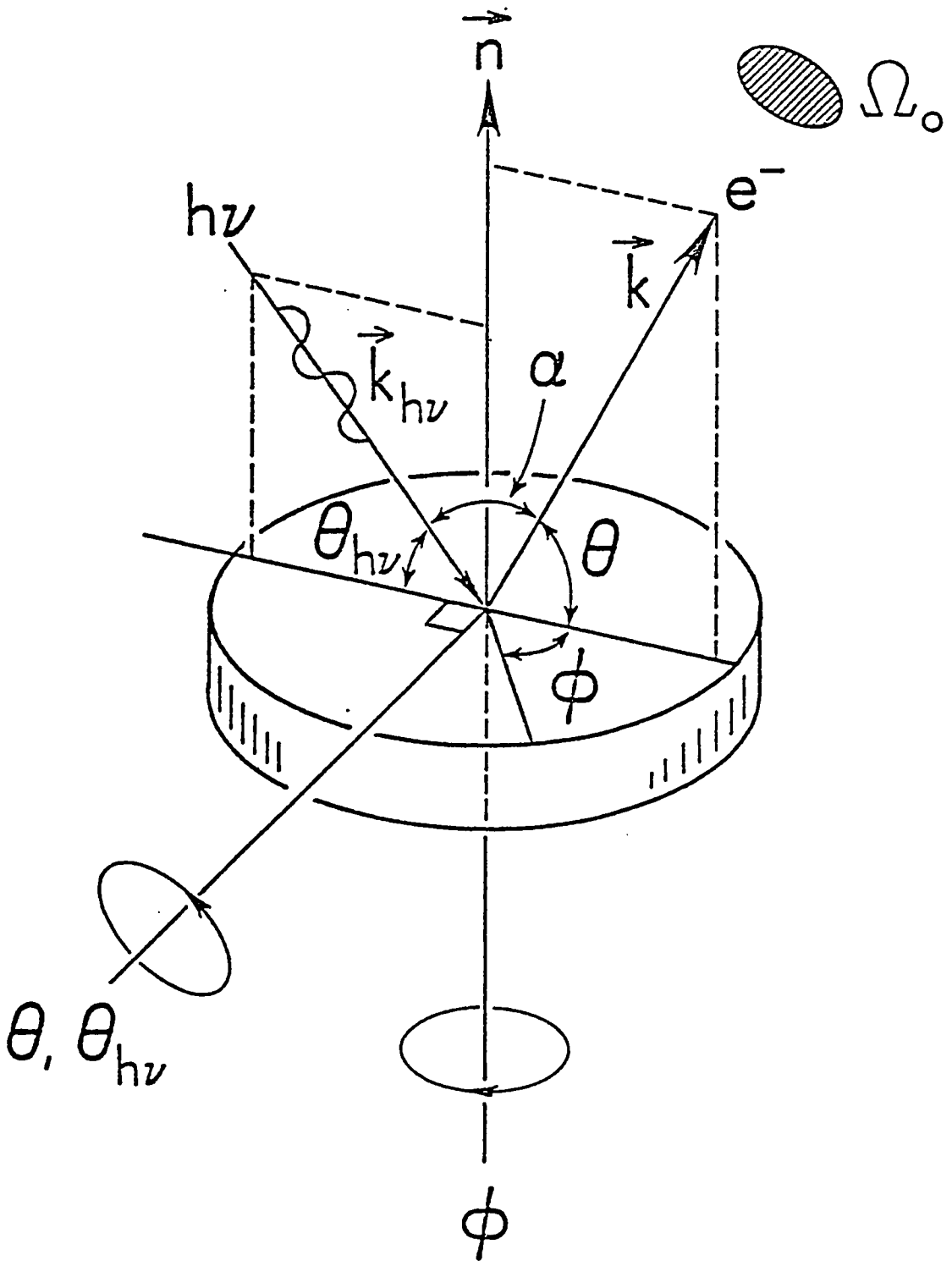

Fig. (*III-1*): General geometry for an angle resolved photoelectron spectroscopy experiment. Specimen rotations on the two perpendicular axes shown vary θ, φ, and $\theta_{h\nu}$ over the full allowed ranges. $\bar{n}$ is the surface normal

surface. This rotation results in variation of the angles 0 and 0_{hv}, thereby varying the emission angle, and azimuthal angle scans, performed by rotating the sample about the surface normal, $\vec{n}$, result in the variation in the angle φ with the electron emission angle remaining constant.

The study of valence-band structure in an AR-PES experiment is used to yield the BE, KE, and momentum $\hbar\vec{q}$ of the ejected photoelectron for each feature of the band .The energy is given by:

$$hv = BE + KE = BE + \frac{\hbar q^2}{2m} \qquad (3\text{-}2)$$

And from momentum conservation, we have:

$$\vec{k}_f = \vec{k}_i + \vec{K}_{hv} + \vec{g} \qquad (3\text{-}3)$$

where $\vec{k}_f$ and $\vec{k}_i$ are the crystal momenta of the final and initial electronic states, respectively, $\vec{K}_{hv}$ is the photon momentum and $\vec{g}$ is a reciprocal lattice vector. $\vec{k}_i$ is then determined since $\vec{k}_f$ is obtained from the measurement of $\vec{q}$ by AR-PES. $\vec{K}_{hv}$ is known from the experimental settings and $\vec{g}$ can usually be assessed. Therefore, with AR-PES, both energy and momentum of a given electronic state of the solid can be determined.

3.1.2 Requirements:

For angle-resolved experiments of this kind the orientation and alignment of the sample axes with respect to the analyzer and excitation

source is critical. One needs to define the position of the sample axes very well. Also, in as much as the valence band is very sensitive to contaminations and surface defects, the sample should be of high purity and have well ordered and clean surface. Valence band measurements should also be performed with a high resolution analyzer to permit the detection of minute characteristics in the band.

A problem that arises in high-energy photoemission , 1.2-1.5KeV, is the $\vec{k}$ broadening associated with the finite angular acceptance of the analyzer. This broadening causes the direct transitions to be smeared out over a disc-like region in the reduced Brillouin zone, thereby limiting the ability to study bands at well-defined zone points. In this energy regime, this contribution to $\vec{k}$ is considerably larger than that due to electron inelastic mean free path [3,5,10,37].

Hence, from the above discussion, we can summarize the experimental requirements for this study as:

*Good definition of the position of the sample with respect to the excitation source and analyzer.

*Well ordered surface of high purity well cleaned sample.

*High resolution analyzer.

*High angular resolution (the acceptance angle of the spectrometer should be very small to permit a good definition of the ejected electrons' momenta and also to permit localizing the DT's to a very-well-defined region in the Brillouin Zone).

3.2 LEED AND XPD TECHNIQUES:

The techniques of low energy electron diffraction (LEED) and X-ray photoelectron diffraction (XPD) are used in our study to check the atomic ordering of the Iridium surface and to calibrate the alignment of the sample axes with axis of the entry lens of the analyzer. The following is a brief description of these two techniques.

3.2.1 LEED :

The technique of LEED has developed into one of the best known and most widely applied techniques for accurate surface measurements [29,38,39]. In LEED experiments, electrons impinge on single-crystalline surface complex and scatter off of the various two-dimensionally ordered layers. The electron waves are diffracted by the surface into angles governed by the two-dimensional momentum conservation relation:

$$\vec{k}'_{\parallel} = \vec{k}_{\parallel} + \vec{g}_{\parallel} \tag{3-4}$$

and the energy conservation:

$$k'_{\perp} = \left(\frac{2mE}{\hbar^2} - k'^2_{\parallel}\right)^{1/2} \tag{3-5}$$

where $\vec{k}_{\parallel}$, $k_{\perp}$ ($\vec{k}'_{\parallel}$, $k'_{\perp}$) are the components of the incident (scattered) electron's momentum parallel and perpendicular to the surface, E is the kinetic energy of the electron away from the surface, and $\vec{g}_{\parallel}$ is a surface reciprocal lattice vector [29].

In LEED the electron energy range is 20 eV ≤ E ≤200 eV. In this energy range, the elastic component of the reflected current is sensitive to the

outermost layers of the surface. Thus LEED is used extensively to make initial characterization of the order at a surface.

3.2.2 XPD :

XPD is a surface structural technique based on the same physical process as photoemission spectroscopy . In XPD, however, the integrated peak intensity of a particular core-level is recorded as a function of either photon energy or angle. The photoelectron intensity varies as a function of these variables because scattering of the photoemitted electron from atoms in the vicinity of the emitter causes interference oscillations in the amplitude of the final state wave function [35,40-42].

The measured photoelectron intensity can be written as:

$$I(\vec{k}) = |\Psi^0(\vec{k}) + \Psi^1(\vec{k})|^2 \qquad (3\text{-}6)$$

where $\Psi^0(\vec{k})$ is the final state wave for the photoexcitation without scattering and $\Psi^1(\vec{k})$ is the final state wave for the photoexcitation with scattering. Thus, $\Psi^0(\vec{k})$ represents the part of the electron wave which reaches the detector in the direction $\vec{k}$ without interacting with any atoms and is termed as the direct wave. The function $\Psi^1(\vec{k})$ represents the part of the electron wave which undergoes scattering with an atom before reaching the detector and is termed the scattered wave. The scattered wave can be thought of as a sum of all possible scattering events from a single scattering to multiple scattering. The oscillations measured in XPD can then be seen as the result of interference between Ψ^0 and Ψ^1 and the interference of the scattered waves with each other .

There are basically two different types of XPD. The first type is the normal photoelectron Diffraction (NPD): In NPD the analyzer and sample are fixed and one measures the intensity variation of a core-level photoelectron peak as a function of photon energy. The range of photon energy is a few tens of an eV to several hundred eV's above threshold [43]. The second type is called the azimuthal/polar photoelectron diffraction. In this type of XPD the photon energy is fixed and one measures the intensity variation of core-level photoelectron peaks with azimuthal angle at several fixed polar angles or alternatively with variation of the polar angle at fixed azimuthal angles [44,45].

XPD patterns can be used as finger prints, to derive very useful information about samples. In our experiment we use the azimuthal/polar XPD method to specify the orientation of the crystal in the system to a precision of better than 1°. This method is based on the fact that the substrate photoelectron emission along low-index directions in the crystal is generally associated with pronounced peaks in the XPD patterns. This peaking along low index directions can be qualitatively explained in terms of Kikuchi bands associated with different sets of low-index planes [46].

CHAPTER IV

EXPERIMENTAL TECHNIQUES

4.1 EXPERIMENTAL APPARATUSES:

4.1.1 General Description :

The experiments reported in this thesis were performed on a Vacuum Generators (VG)-Scientific ESCALAB MK2 spectrometer. This spectrometer has the capabilities for doing angle resolved spectroscopy as well as a large number of surface analytic techniques to carry out complete surface analysis of a sample under the same experimental conditions in one instrument [47]. The system consists of five different chambers. Figure (IV-1) shows a line drawing of the system, Figure (IV-2) is a photograph of the instrument. The main analysis vessel is made of mu-metal to reduce magnetic field in the analysis chamber to about 2 mGauss, it is equipped with a dual, aluminum-magnesium, anode, a hemispherical electrostatic energy analyzer (also made of mu-metal), adjustable inlet and outlet slits, two Einsel lenses and three independent detectors to provide high efficiency detection.

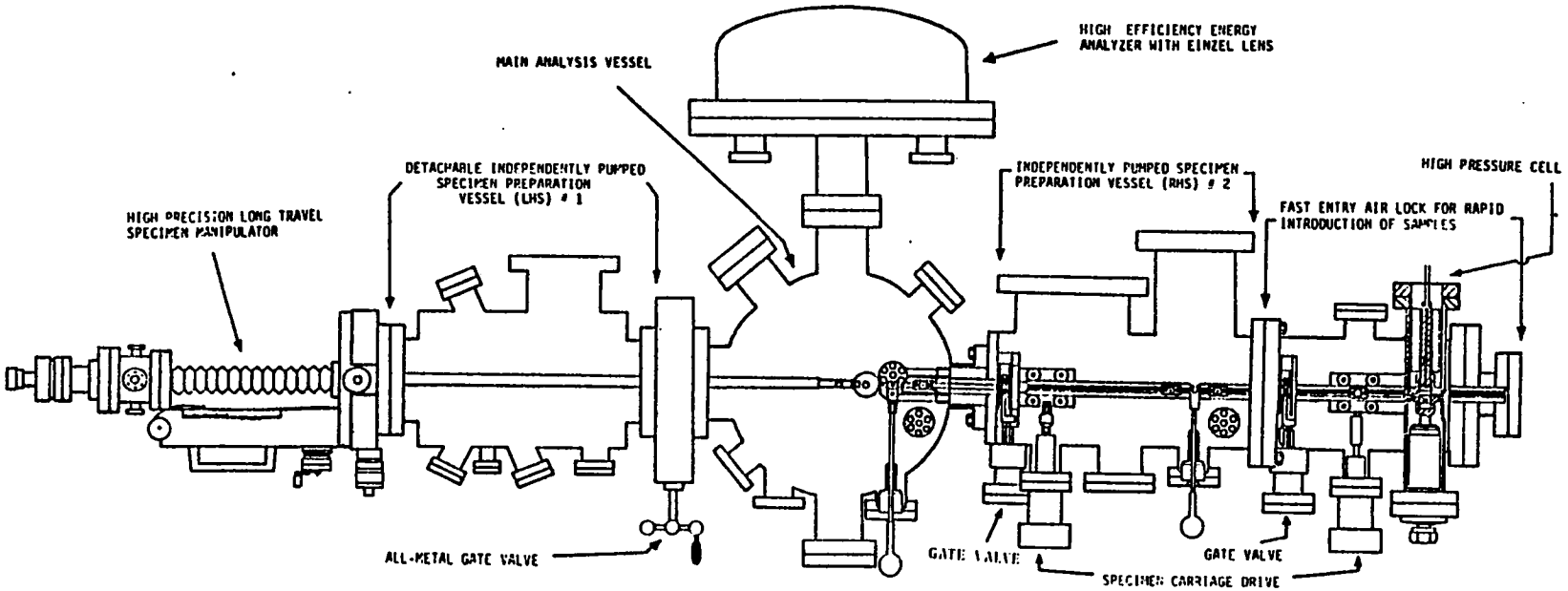

SCHEMATIC DESIGN OF PHOTOELECTRON SPECTROMETER

Fig. (*IV-1*): Schematic drawing of the overall Vacuum Generators (VG) scientific ESCALAB MK2

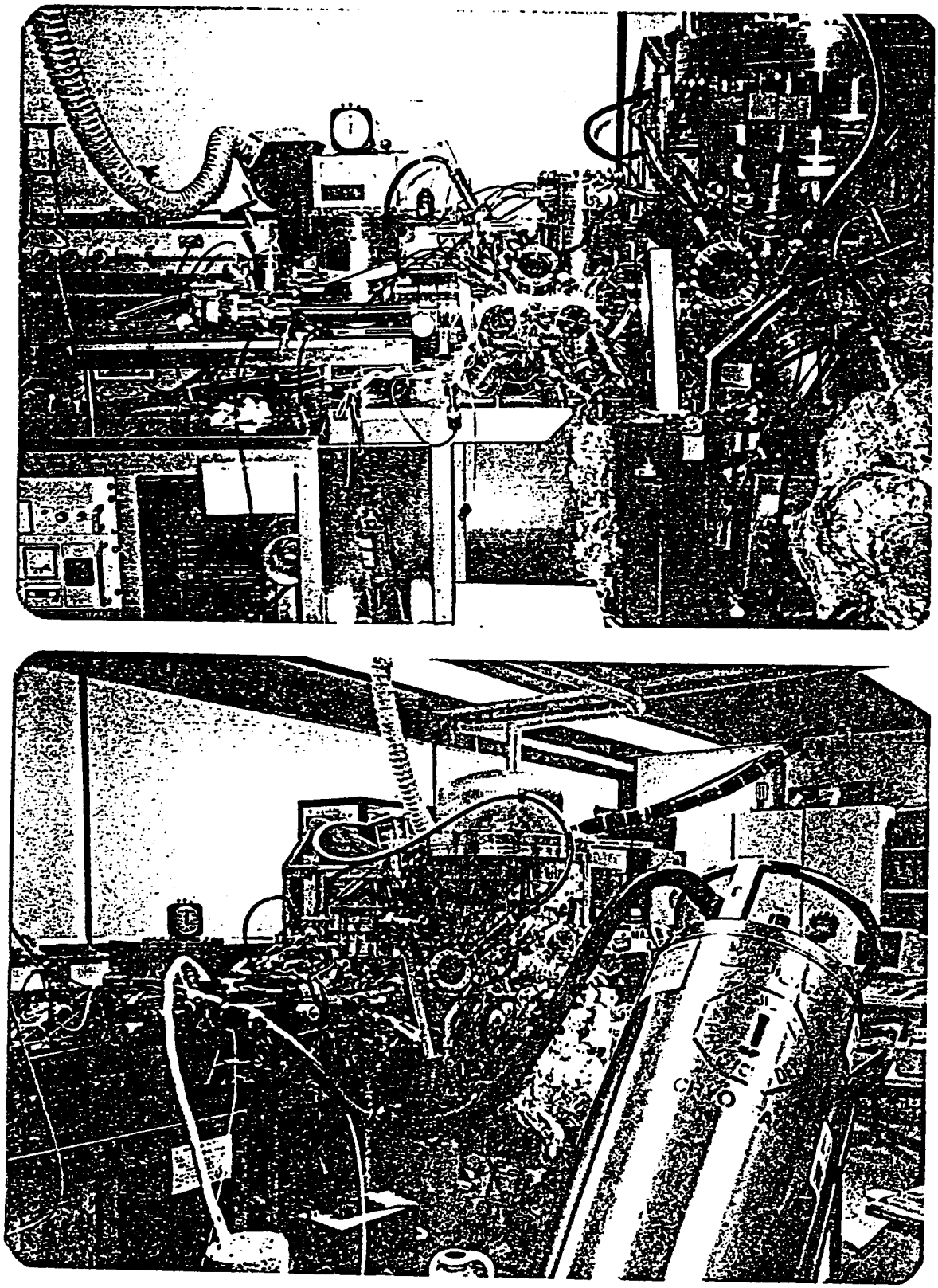

Fig.(IV-2): Overall photograph of the system in Figure: (IV.1) as viewed from the front

The main chamber is also equiped with an X-ray monochromator with 0.5 meter Rowland circle and twin anode (Al,Ag) X-ray source, an ultraviolet radiation source, an electron gun, a differentially pumped Ion gun, an electron flood gun and a low energy electron monochromator.

In the left hand side (LHS) preparation chamber, all preliminary sample preparation (cleaning and surface ordering determination) is performed. The chamber , can be isolated from the main chamber through an all metal gate valve . This chamber is equiped with various facilities for sample preparation: a sputtering ion gun, bakeable gas admission system, a quadrupole mass analyzer and a reverse view LEED system (Varian model RVL 640 with power supply model 474). This chamber is also equiped with a high precision manipulator with both polar and azimuthal angle rotation of the sample as well as capabilities for keeping the sample at a desired temperature in the range of 100K-2000K. A linear travel of up to 600mm carries the sample, after preparation, into the main chamber analysis for final surface analysis. Figure (IV-3) shows a photographic view of the specimen end of the manipulator.

The other three chambers, the right hand side (RHS) preparation chamber, the fast entry airlock and the high pressure gas cell insure quick transfer of samples to the experimental vessel without breaking the ultra-high vacuum (UHV). They are also equiped with various instruments for special sample in-situ preparation.

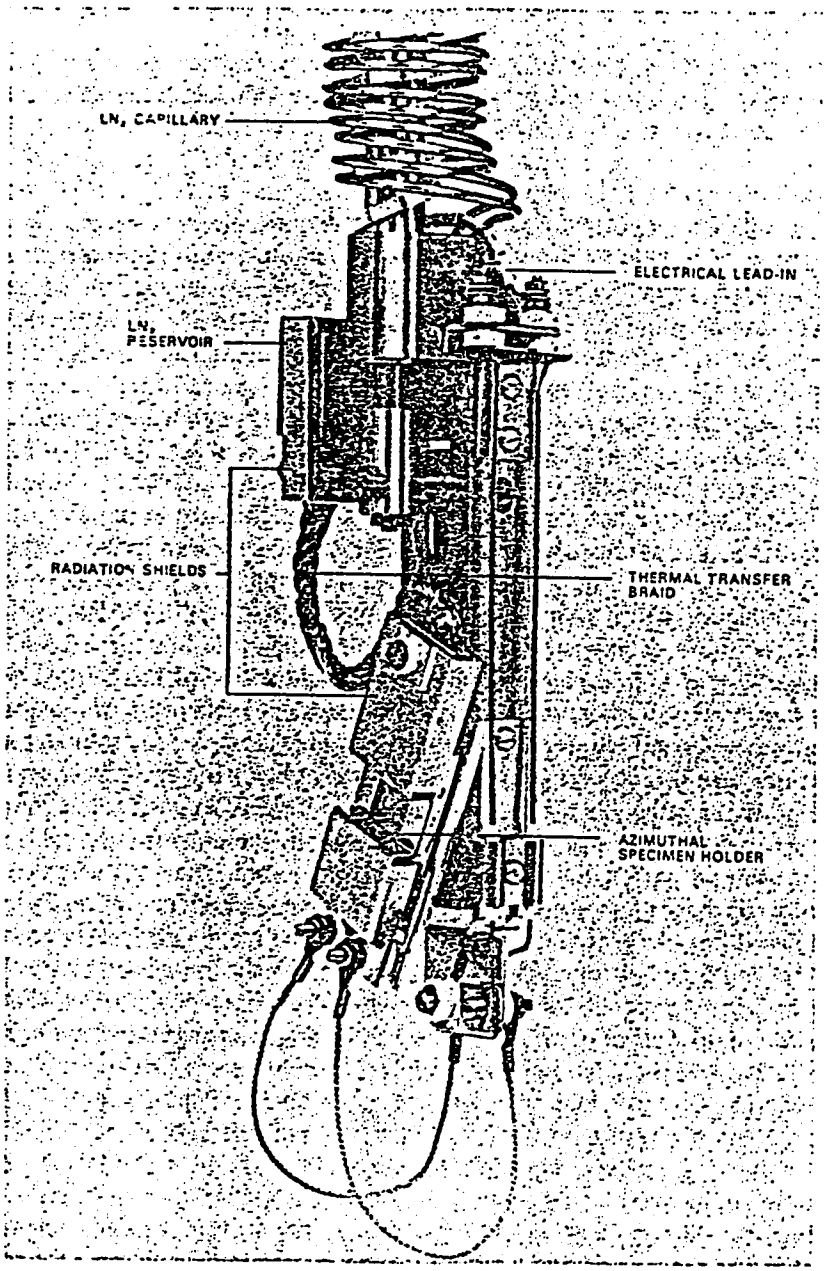

Fig.(IV-3): Photograph of the combined heating and cooling stage for the sample treatment. Heating is provided by conduction from an insulated hot filament under the substrate surface on which the specimen is mounted. Cooling is achieved by conduction along a copper braid fixed to a tank through which liquid nitrogen is passed. The stage is mounted on the shaft of a high precision long travel manipulator.

The system comprises UHV oil free pumping (four ion pumps, three titanium sublimation pumps and three turbomolecular pumps) to insure base pressures of the order of 10^{-11} mbar in the system. Pressure measurements are done with BAYARD-ALPERT ionization gauges with IGC 26 ION GAUGE and LEYBORD-HERAEUS IONIVAC IM 510 controllers.

A dedicated micro-computer (PDP 11/73) performs system control and data acquisition and processing. The PDP computer has an RSX11-M multi-user operating-system with complete data processing software (which includes smoothing, peak fitting, background and sattelite subtraction in addition to many other functions). Also connected to the system are a high speed HP plotter and EPSON printer and ploter.

4.1.2 Analyzer Operation and Calibration :

The electron energy analyzer, the major component of the whole system, is a concentric hemispherical analyzer (CHA). This type of analyzers is the most often used for electron energy analysis, particularly when high energy resolution and directional sensitivity is required [48,34]. Figure (IV-4) shows a cross-sectional view of the electron spectrometer with all the major elements from the specimen to the detector. The analyzer is made of mu-metal to reduce the earth's magnetic field. The analyzer is based on 150 mm mean radius spherical sector, and acts as a narrow pass filter letting through only electrons with energy $H \times D$ eV, where D is the potential difference between inner and outer hemispheres

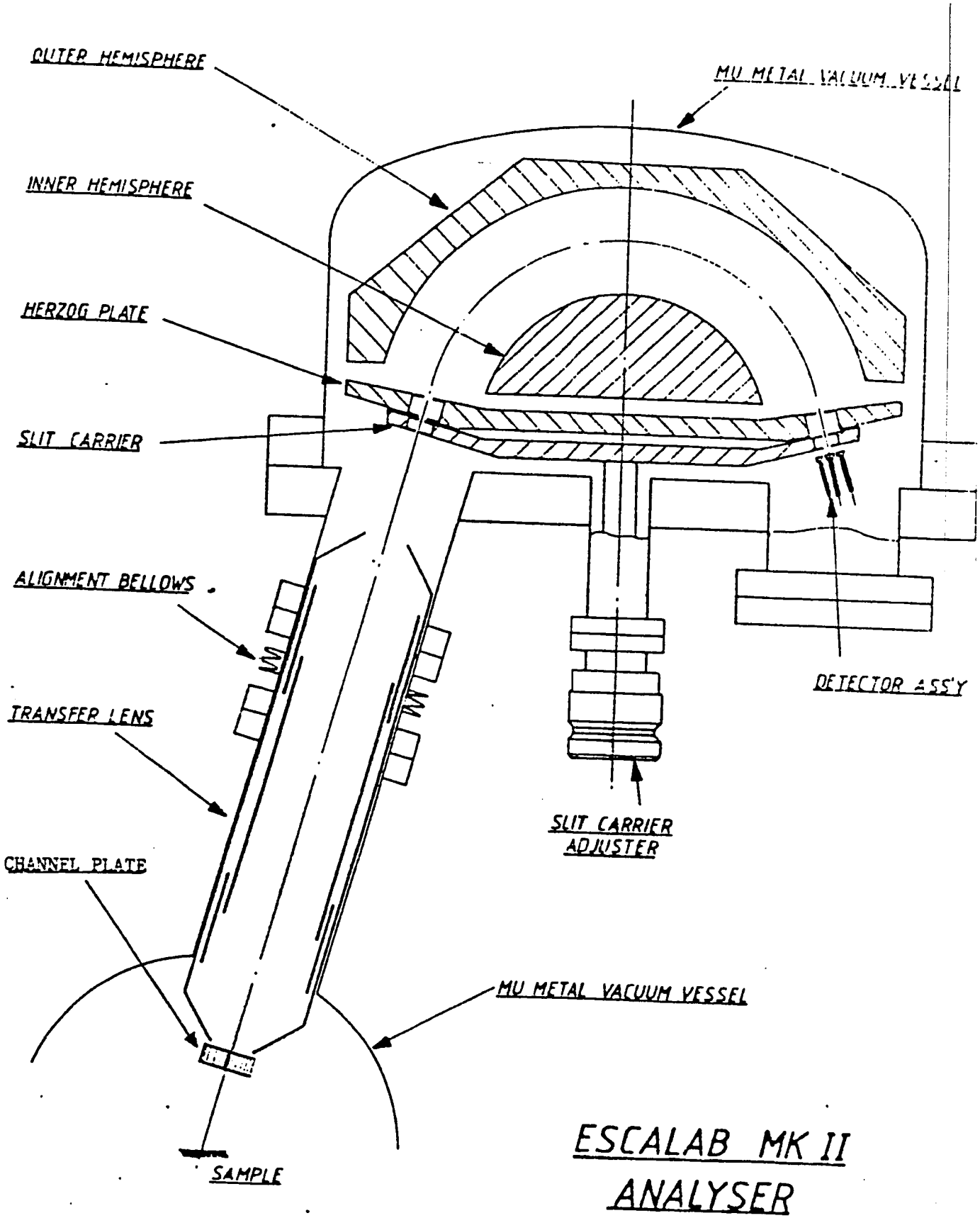

Fig.(IV-4): Overall cross section of the VG-scientific ESCALAB MK2 electron optical system, showing all of the major elements from the specimen to the detector.

and H is a constant determined by the physical characteristics of the analyzer. The electrons transmitted from the sample to the analyzer by the electrostatic lens are retarded by an amount R (eV) in energy before entering the analyzer. The kinetic energy, KE, with which an electron leaves the sample with respect to the vacuum level is recorded as:

$$KE = H - D + R + \Phi$$

(Φ is the work function of the spectrometer).

The analyzer can be operated in two retarding modes: one of the modes is the constant relative resolution (CRR) mode in which the electrons are decelerated by a constant ratio from the initial kinetic energies. In the second mode, the electrons are decelerated to a constant pass energy with which the resolution would be constant over the entire spectrum. This mode is termed constant analyzer energy (CAE) or constant energy transmission (CAT). Retardation is accomplished through two Einsel lenses. All controls of the operating functions of the analyzer are performed by the PDP11/73 computer.

The energy scale of the spectrometer was calibrated using the photoelectron lines [49]: Cu $2p_{3/2}$ = 932.67 eV, Cu $3p_{3/2}$ = 74.90 eV, and Au $4f_{7/2}$ = 83.98 eV.

In our experiment the analyzer is operated in the constant resolution mode with a pass energy of 10 eV for all valence band spectra and 20 eV for contamination check XPS spectra. The exit slit is $6 \times 10\ mm^2$. The analyzer energy resolution is 0.9 eVat this pass energy.

4.1.3 Excitation Source :

The excitation source used is a soft X-ray source with dual anodes allowing the use of either magnesium or aluminum K_α (Al K_α or Mg K_α), radiation lines by simple external switching of anodes.The X-ray source is of the type shown in Figure (IV-5) It basically consists of two filaments, for electron bombardment, and two anode surfaces one of Magnesium and the other of Aluminum. The source is operated with the filaments near earth potential and the anodes at a positive potential of up to 15 keV.

Both the Al K_α (1486.6 eV) and Mg K_α (1253.6 eV) lines were used for the different XPS analysis of our sample. However only Mg K_α radiation was used for valence-band spectra because its line has a narrower width of 0.7eV -compared to 0.85eV [50,51] for Al K_α. The added width of Al K_α line would decrease the energy resolution of the valence band spectra. Also the effect of the photon wave vector $\vec{K}_{h\nu}$ in the k conservation relation Eq. (2-8) is smaller for Mg K_α. Moreover, the Debye Waller factor given in Eq. (1-1) is slightly higher for Mg K_α which results in an increase of the DT component in AR-XPS valence-band spectra (see table 1).

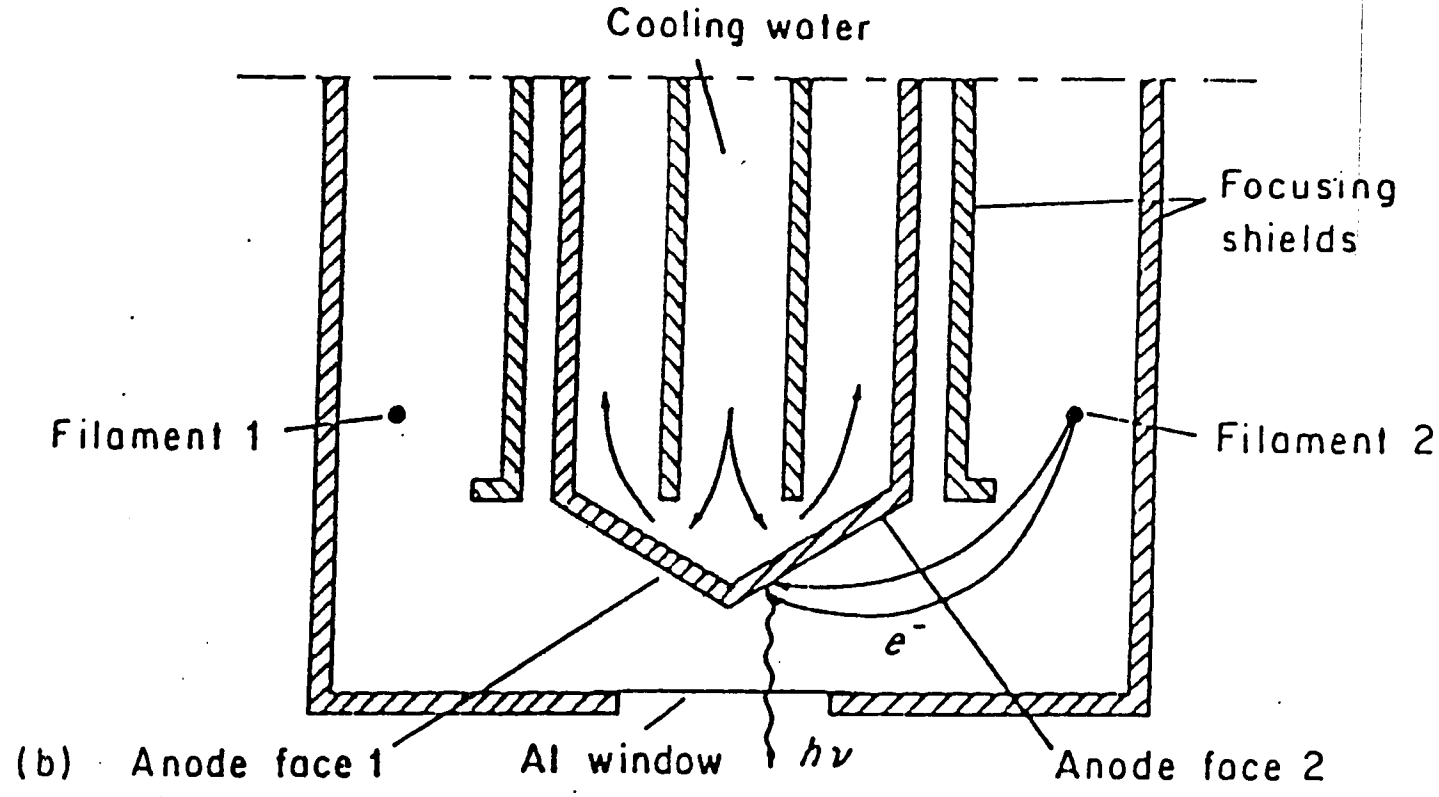

Fig.(IV-5): Soft x-ray source with dual anode, allowing use of either magnesium or aluminum K_α radiation by simple external switching without the need to break the vacuum in going from one to another. The anode has a trapered end with two inclined faces on which films of magnesium or aluminum, are deposited.

4.1.4 High Precision Manipulator :

A Varian high precision long travel (HPLT) manipulator is used to position the Iridum sample for sample preparation, in the LHS chamber, and for the photoemission measurements in the main chamber (Figure (IV-3)). A travel of up to 600 mm (Z-direction) allows the sample to be moved from the first chamber to the following chamber. The resolution in the Z-direction is 0.01mm and repeatability is 0.1mm. The motion in the X- and Y-directions are up to 20mm with a resolution o 0.005mm and repeatability of 0.01mm. A full 360° rotary polar motion and 180° azimuthal motion are possible with resolutions better than 1°. The manipulator also has capabilities for keeping the sample at a desired temperature between 100K-2000K.

i) Heating :

Heating is achieved through conduction from an insulated hot filament (cathode) under the substrate surface (Tantalum foil) on which the specimen is mounted. This anode, and hence the sample, are raised to a voltage V (up to 1kV) and a hot filament supplies electrons for bombardment. The cathode is of thoria coated iridium wire. The anode, cathode support tray, specimen clamps and screws are of molybdenum. The anode and cathode are supported and thermally insulated by alumina. The heater is assembled onto a stainless steel backing plate and is connected to an electron beam power supply and temperature controller. A different power supply is used for heating the filament when doing

experiments at high temperatures.This power supply is set in such a way as to give a constant current to the cathode insuring that the sample is always well grounded.

Two Chromel-Alumel thermocouples, one fixed near the sample and the other 1.5cm away, are used to measure the temperatures of the sample at various stages of the experiment.

ii) Cooling :

Cooling is achieved by conduction along a short length of Copper braid that joins a liquid nitrogen reservoir to the specimen plate. The liquid nitrogen reservoir has a cooled copper surface which is in direct contact with the liquid nitrogen and is electrically and thermally isolated from the body of the manipulator, on which it is mounted. Liquid nitrogen is conveyed inside the vacuum system through a co-axial feedthrough which is connected to the liquid nitrogen reservoir by a coil of small bore stainless steel tubing.

When doing experiments at low temperatures, pressurized dewars are used to feed liquid nitrogen to the manipulator. When this facility is not available, a gravity feed set up is used instead. The gravity feed set up is constructed from an expanded polysterene dewar pierced for a copper tube that connects to the liquid nitrogen feedthrough. A small vaccum pump is used evacuate nitrogen through the outlet. The consumption of liquid nitrogen is lower using the second method. However, the use of pressurized dewars is more convenient. Care should be taken to prevent

the possibility of blockage occuring in the tubes due to the formation of ice crystals which tend to form when the open gravity feed dewar is used. A temperature of approximately 120K was achieved in most of the cases within 20 to 30 minutes.

4.1.5 Channel plate characterization and mounting:

As was mentioned in paragraph 3.1.2, the acceptance angle of the analyzer should be very small in AR-XPS valence-band studies (less than 1°). Methods of achieving such resolutions have been discussed in detail in previous studies [52-54]. Of these methods, is the use of multiple apertures or apertured zoom lenses before the analyzer entry, and channel-cut collimator before entry into any of the electron optics. We used this method in our study. A recent paper by White et al [55] discusses the characterization of different types of channel arrays both experimentally and theoretically. The channel array used in our experiment is a glass channel plate in a hexagonal close-packed configuration. This channel array has the properties of not distorting spectral features or background, maximizing intensity for a given well defined angular resolution desired and reducing, in relative magnitudes, very low energy secondary electrons intensities [56]. The detected intensity, however, is decreased by as much as a factor of 50 of the intensities with fully opened inlet slit.

The glass channel plate was mounted on an externally movable holder placed in a field-free region in front of the electron lenses. The axis of the very small parallel hexagonal tubes in the channel plate was oriented with

respect to the holder slit axes (which is the same as the lens axes) through the use of laser beam. A typical configuration of such hexagonal-close-packed array of cylindrical tubes is schematically illustrated in Figure (IV-6). The diameter-to-length ratio, d_o/L_o, for the tubes rigorously limits the maximum angular deviations from the tube axes to $\pm\alpha_{max} = \pm\tan^{-1}(d_o/L_o)$. The measured dimensions of the channel-plate used here are: $d_o = 10.7\mu m$, $L_o = 0.54mm$, thus the maximum angular deviation is $\pm\alpha_{max} = \pm 1.1^{\circ}$. Retardation of the photoelectrons to 10 eV before analysis may also result in some loss of intensity due to enhanced deflection angles. Therefore, the effective angular acceptance is less than $\pm 1.1^{\circ}$ and is, more likely, less than 1° as required for this type of study. As an illustrative example of the effect of increased angular resolution on Iridium AR-XPS spectra due to the addition of such channel plate array, Figure (IV-7) compares spectra at temperature T = 120K, Mg K_α excited, from Ir(111) at normal incidence obtained with (a) the $\pm 1.1^{\circ}$ channel plate in place and, (b) with only the standard lenses-entry aperture which approximately limits the acceptance angles to $\pm 6.0^{\circ}$. The differences between these two spectra are striking. The small acceptance angles curve show clearly the presence of two peaks at ~1eV and ~5eV, whereas the high acceptance angle curve shows a flat region instead of a peak at ~1eV and the magnitude of the second peak is reduced considerably. A shoulder like peak at ~3.5eV is also seen in the high resolution, low acceptance angle, curve. This feature is not present in the low resolution, high acceptance angle, spectrum.

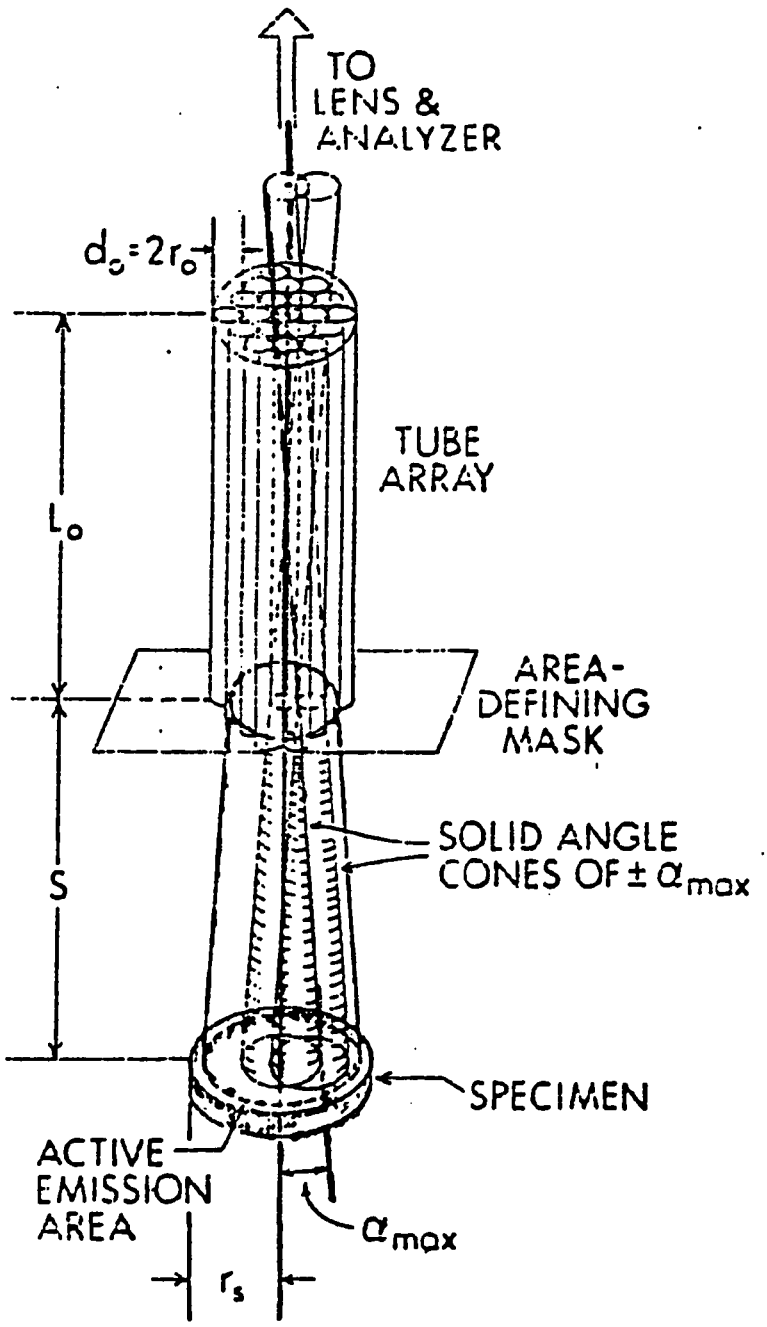

Fig.(IV-6): Schematic view of a hexagonal close-packed channel array. Shown are the different parameters and method of angle definition.

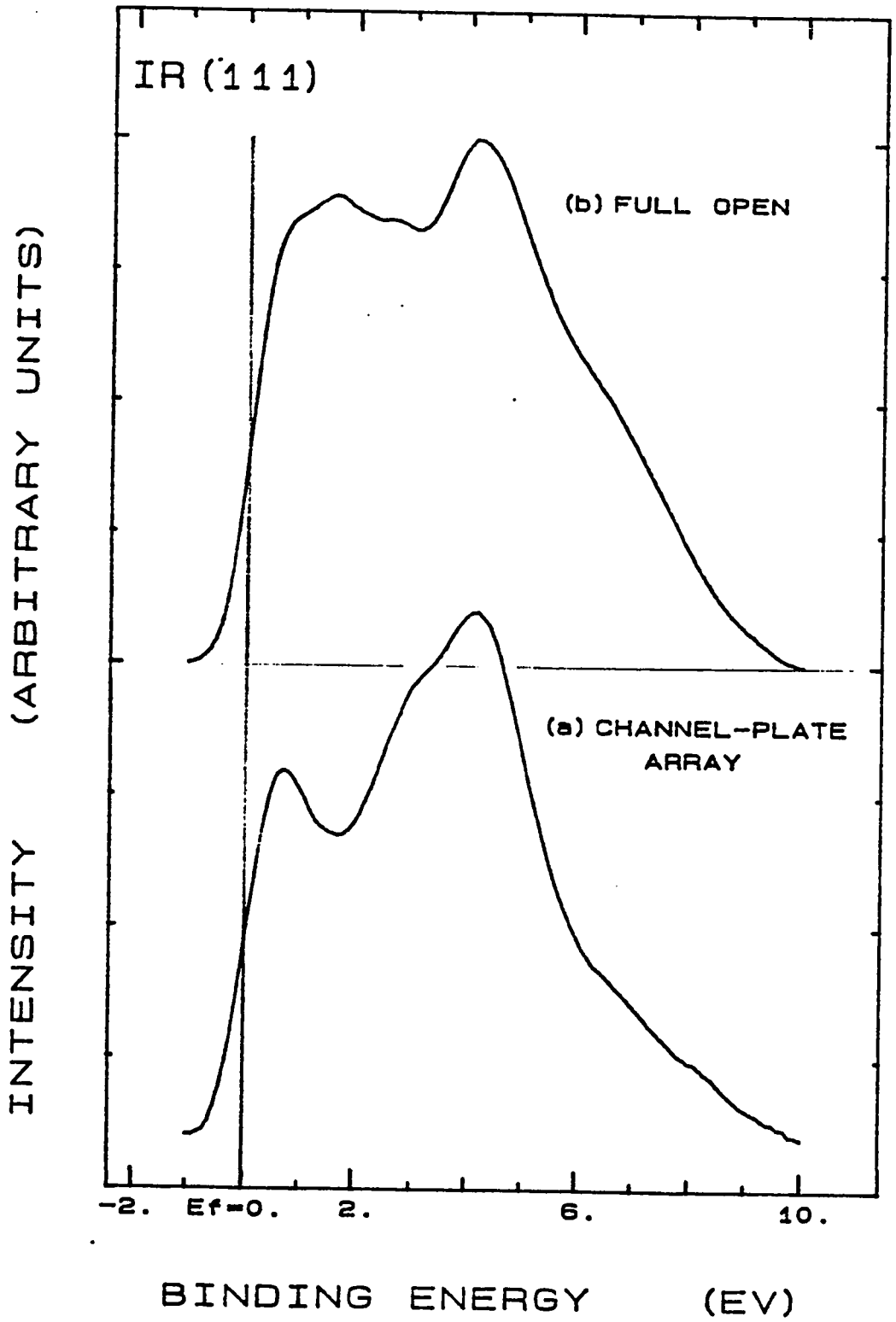

Fig.(IV-7): The effect of increased angular resolution on Mg K_α -excited spectra from Ir(111) at 120K. In (a), a channel plate array of $\pm 1.1^\circ$ angular resolution is used, and in (b), the standard lens-entry aperture of $\pm 6^\circ$ is the only angle-defining device.

4.2 EXPERIMENTAL TECHNIQUES:

4.2.1 Vacuum :

To study photoemission from clean surfaces, it is necessary to perform the photoemission experiment in ultra high vacuum. In our experiment, a base pressure of 5×10^{-11} mbar and of 2×10^{-10} mbar are achieved in the main and LHS chambers, respectively, after 16 hours of bake out at 180°C -200°C. During the first 8-hours of the bake out the system was pumped by tubomolecular pumps. The pressures in the chambers would be about 2×10^{-6} mbar at the end of this stage. The second 8-hours of the bake out, ion pumps, with concurrently cycled titanium sublimation pumps, are used. The chambers' base pressure after this stage is about 5×10^{-7} mbar. After turning the heaters off, the pressure in the chambers drops off quickly as the chambers cool down. Following the bake out, series of outgassing steps including the outgassing of all filaments and of the sample itself is carried out. After another 8 hours the chambers pressure reaches the pressures of 5×10^{-11} mbar and 2×10^{-10} mbar in main and preparation chambers, respectively.

4.2.2 Sample preparation and cleaning:

A high purity Iridium sample (99.999%) was cut and polished down to 0.25μm. The methods used in this part of the sample's preparation were explained in details by Chan et al [56]. The orientation of the crystal with respect to its (111) direction was checked by the Laue back-reflection

technique. The sample gave well defined Laue spots and the front surface exhibited a smooth mirror-like finish after polishing. The shape of the sample is an oval with the larger diameter of about 7mm . The sample thickness is 1.5mm .

The sample was mounted on a Tantalum foil plate which was fixed onto the manipulator. The mounting consisted of clipping the sample from its sides to the plate with small strips of tantalum which were spot welded to the plate.Tantalum was used for its high purity (99.9%), temperature compatibility and its thermal expansion coeficient which is similar to that of Iridium. The plate has a hole just below the sample to allow for better heating by the filament heater underneath.

After the specimen was placed in the spectrometer , impurities of carbon, oxygen and their compounds were the only contaminations detected on the surface of the sample. Figure (IV-8(a)) shows an overall XPS spectrum of Iridium with Mg K_α radiation, with the impurities present during the initial stages of the experiment labelled. LEED patterns taken at this stages were fuzzy. The first in-situ cleaning process was sputtering of the surface with 2 keV Argon ions. For Argon ion bombardment, the LHS preparation chamber is isolated from the main chamber by closing the all-metal valve, and filled with 5×10^{-6} mbar of argon (Ar) gas through a precision leak valve.

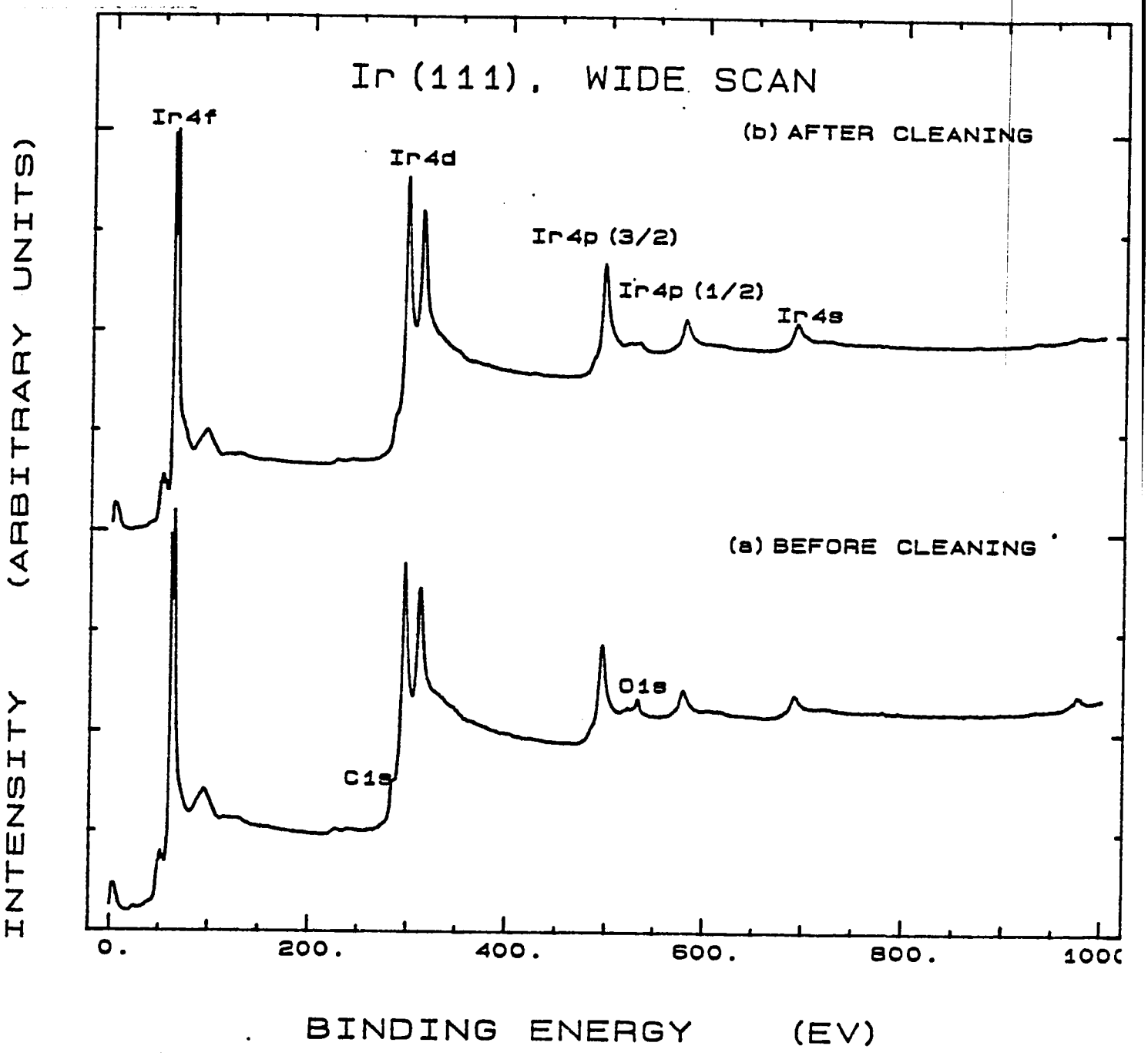

Fig.(IV-8): Comparison of XPS overall spectra with Al K_α excitation from Iridium (111) before (a) and after (b) sample cleaning in UHV. The clean surface spectrum in (b) indicates that essentially all impurities were removed by the cleaning process.

The Ar atoms are ionized by an electron gun (Varian model 981-2043) built inside of the Varian sputter gun, and accelerated to 2 keV and steered by biasing tubes and plates in the gun. Afterwards, the argon is pumped out to once again achieve the 10^{-10} mbar base pressure in the preparation chamber. Next, the sample is annealed to about 1100K. The Ar^+ bombardment and annealing were done in repeated cycles. The first cycles, Ar^+ bombardment was done at grazing angles of incidence 30° – 40° degrees for half an hour. LEED patterns improved notically after each cycle. A ring-like structure in the LEED pattern at this stage shown in Figure (IV-9(a)) is due to graphite formation on the sample as reported by Grant [57] and Kuppers et al [58]. This was hard to remove through only sputtering and annealing alone. An oxidation treatment was necessary to remove residual carbon. The treatment consisted of oxidizing the carbon on the surface to carbon monoxide (CO) which is removed by flashing the sample to higher temperatures. In this operation, the sample was heated to about 1100K in a background pressure of 5×10^{-8} mbar of pure oxygen (99.99 %) for 5 minutes. During oxidation, the LHS chamber is slightly opened to the ion pump to ensure a fresh flow of oxygen pressure through the balance of the leak rate from the oxygen bottle and pumping rate by the ion pump. Heating is performed through the floating of the sample to about 0.6 kV and heating the nearby filament to supply electrons for beam bombardment .

After heating in oxygen, the sample is flashed to a high temperature of ~1400K in UHV to remove the oxide layer formed during cleaning and to

anneal the surface.

The surface is then analized using LEED and XPS to monitor surface order and cleanliness. A well developed crystal surface characterized by sharp LEED spots as shown in Figure (IV-9(b)) have been achieved after several full cycles of the above treatment. Figure (IV-8(b)) shows the overall XPS spectrum of clean Iridium. Carbon and oxygen contaminations are reduced to a minimum as shown in Figures (IV-10) and (IV-11) where C1s and O1s core levels are investigated using XPS. The check experiment of this kind is always done at enhanced surface sensitivity (at grazing angles emission) to accurately inspect the complete surface cleanliness.

4.2.3 Sample Orientation:

The orientation of the sample is critical because one should know the position of the crystal axes with respect to the analyzer exactly in order to relate the experimental data to theoretical predictions.

A stereographic projection for cubic crystals on (111) plane is shown in Figure (IV-12). Each line defines a symmetry plane of the crystal and the planes are projected as dots. Knowledge of the position of only one of these lines with respect to the spectrometer and excitation source plane enables one to define the overall orientation of the sample. In that sense our main objective was to find the high symmetry horizontal line $[11\bar{2}]$ which contains low index planes (001), (111),... and (112).

(a)

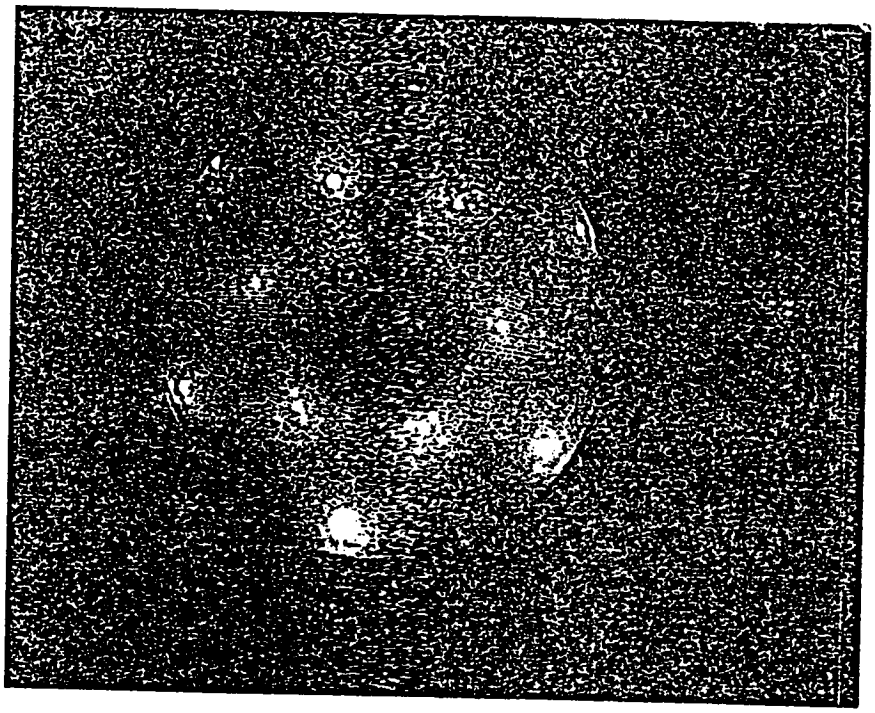

(b)

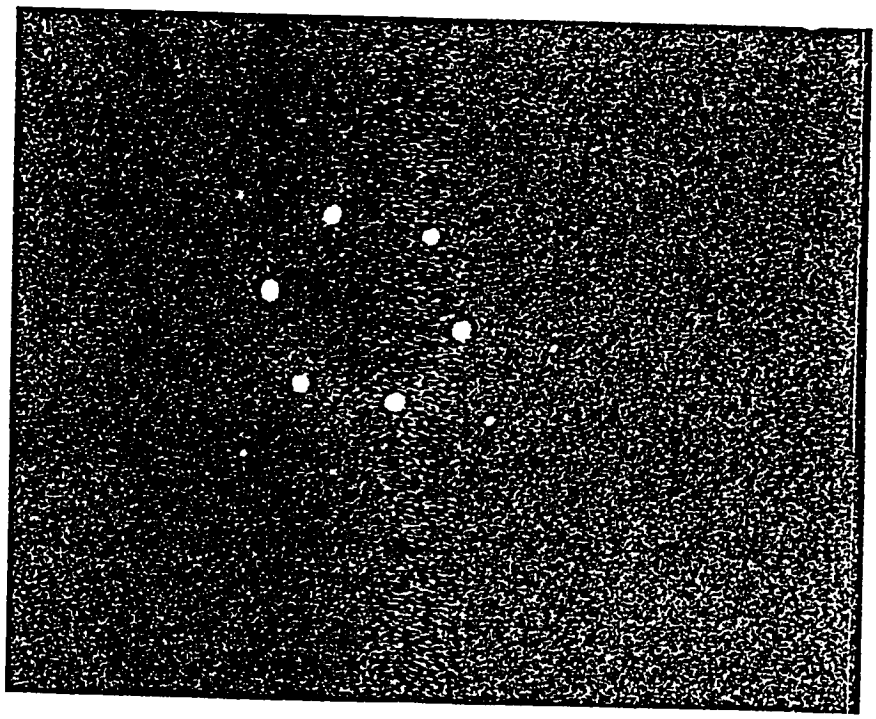

Fig.(IV-9): LEED patterns from Iridium (111) before (a) and after (b) oxidation treatment and annealing. In (a) the ring-like structure is due to graphite formation.

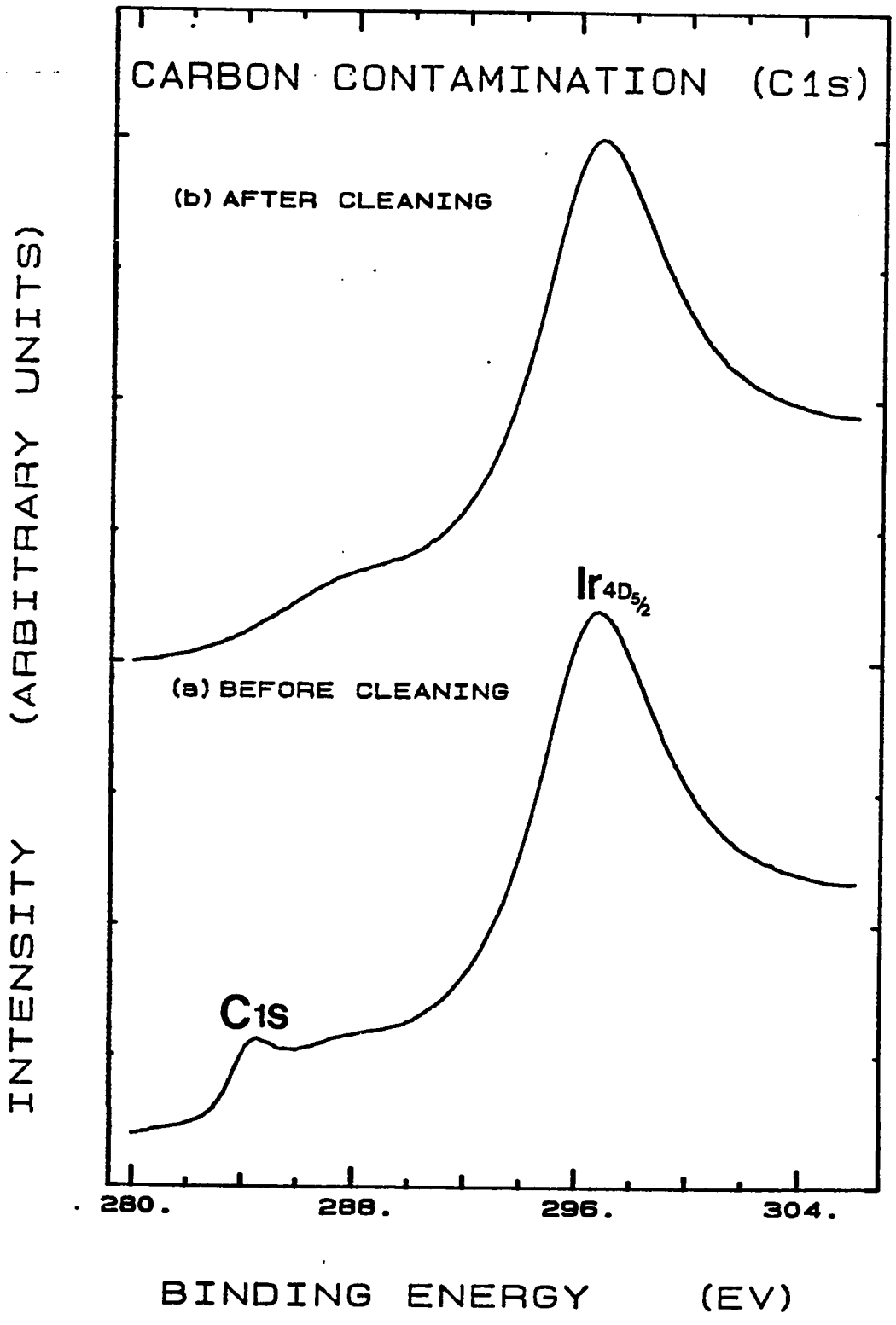

Fig.(IV-10): Photoemission spectra of C1s with Mg K_α excitation from Iridium (111) before (a) and after (b) sample cleaning. Both spectra are taken at enhanced surface sensitivity.

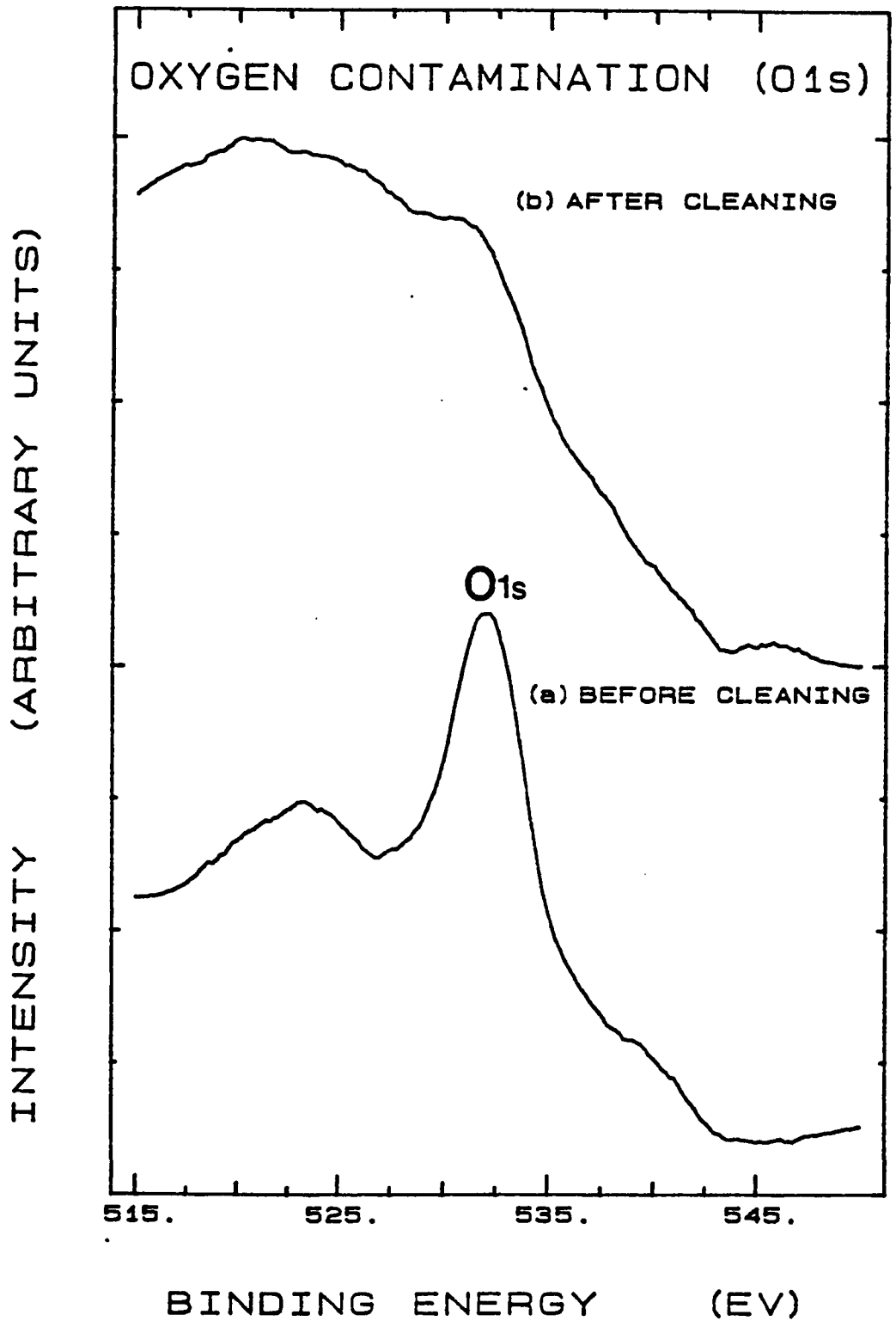

Fig.(IV-11): Same as Figure: (IV.10) but for O1s peak.

Our experimental geometry is thus refered to this line as shown in Figure (IV-13). Azimuthal scans are performed by rotating the sample about [111] direction. The azimuthal angle's origin, $\varphi = 0^{\circ}$, is taken to be along the $[11\bar{2}]$. The polar angle θ is measured with respect to the surface, such that 90° corresponds to emission perpendicular to the surface. Such orientation has been done in two stages: in the first stage the sample was oriented to within 0.25° of (111) plane as checked by Laue-back reflection method, and the low index plane (100) spot position was defined with respect to the external shape of the sample, i.e., the angle and direction to rotate the sample refering to its shape in order to find the (100) plane are defined. The second stage is the specification of the orientation of the crystal in the experimental system. First the sample is mounted on the manipulator according to Laue experiment information. LEED patterns are used to define and to calibrate the normal position of the sample in the chamber. This is done by positioning the sample normal to the beam of incident electrons of the LEED in a way that the diffracted electrons seen show good symmetry around the central point. After this stage, XPD is used. Azimuthal scans of the photoelectron intensity of the Ir4f core levels at polar angles near the position of the plane (100) as determined by the Laue experiment, followed by a set of polar scans for different fixed azimuthal angles to find the high symmetry low index $[11\bar{2}]$ line. Figure (IV-14) shows a sample of the final raw experimental XPD data for 40° azimuthal scan of Ir4f photoelectron intensity at polar angle corresponding to (100) position. In Figure (IV-15), a polar scan of Ir4f photoelectron intensity

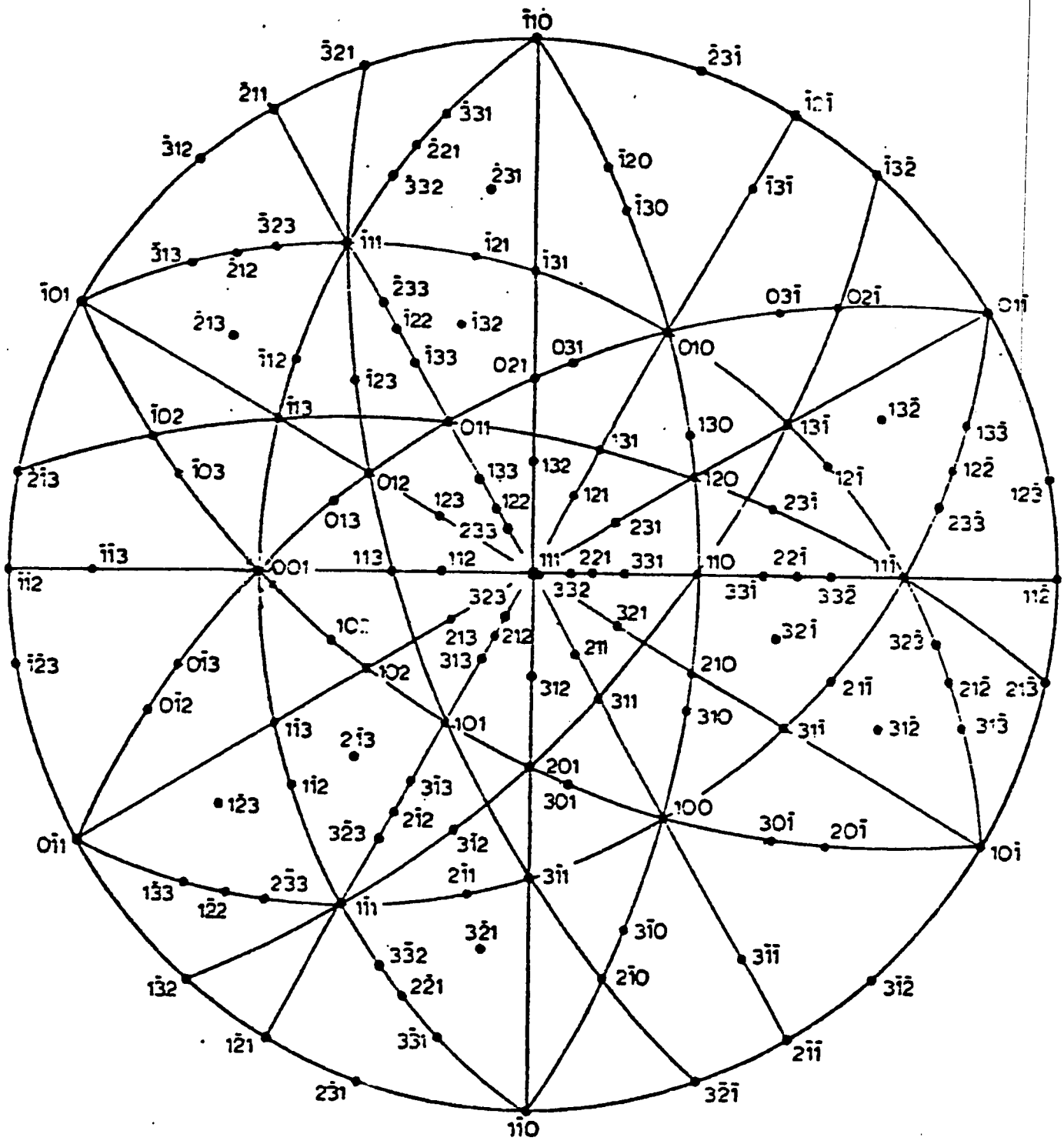

Fig.(IV-12): Stereographic projection for cubic crystals on (111) plane.

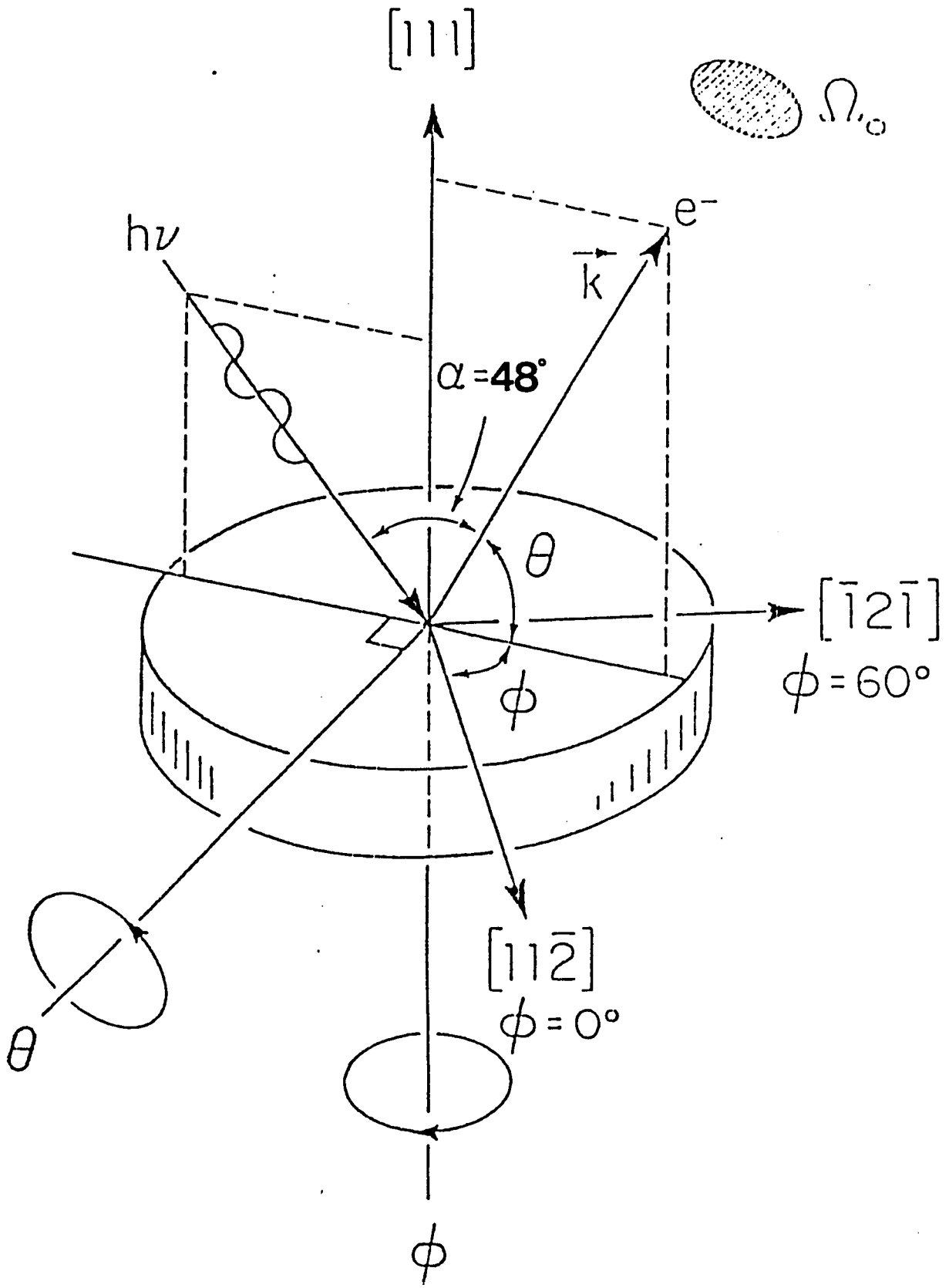

Fig.(IV-13): Schematic illustration of the experimental geometry with various pertinent angles defined . $\varphi = 0^{\circ}$ is defined to be along the $[11\bar{2}]$ direction and 0 is measured with respect to the surface, such that 90° correspond to emission perpendicular to the surface.

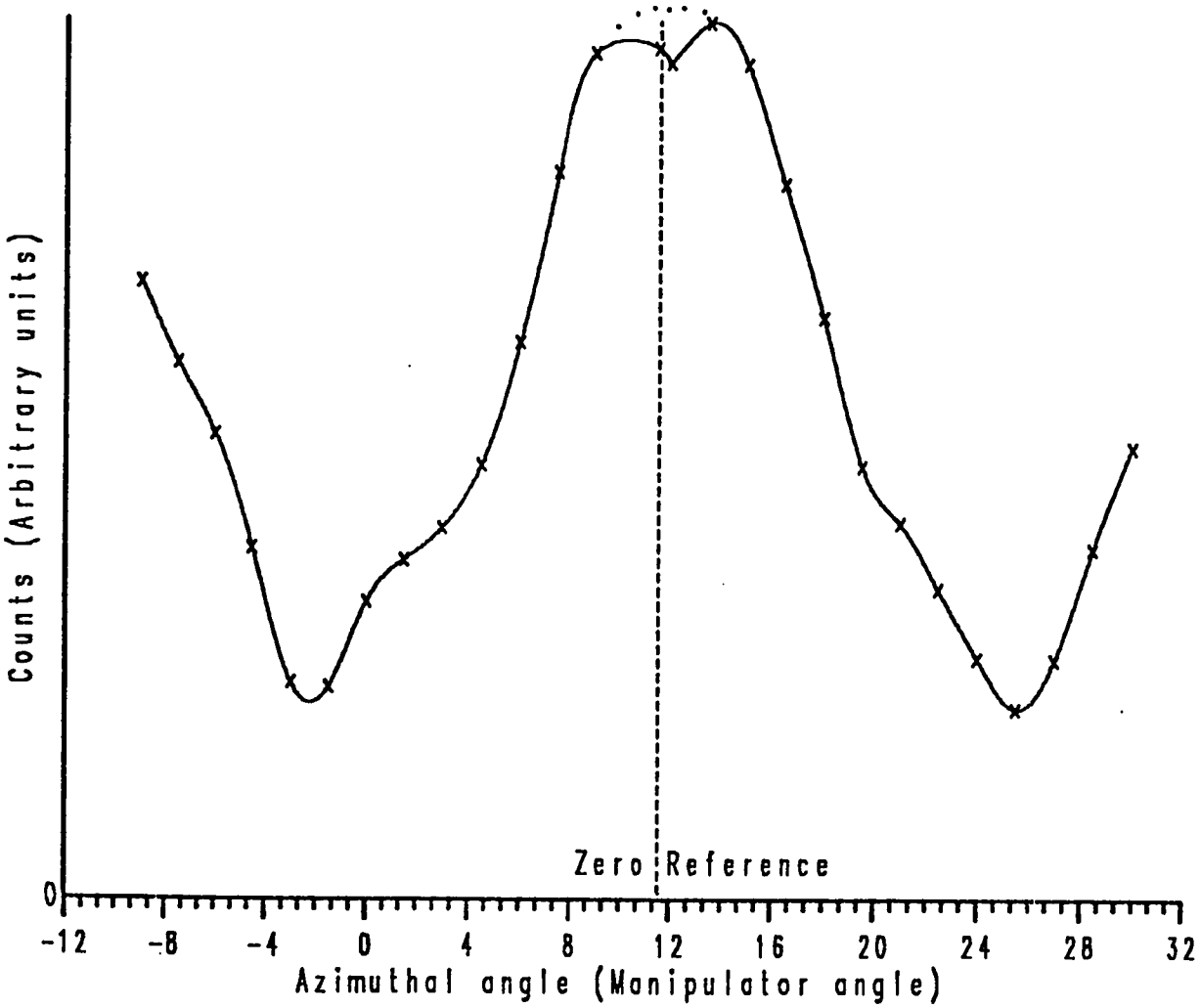

Fig.(IV-14): Raw experimental XPD data for 40° azimuthal scan of Ir4f photoelectron intensity at polar angle of 54.7° corresponding to (100) plane.

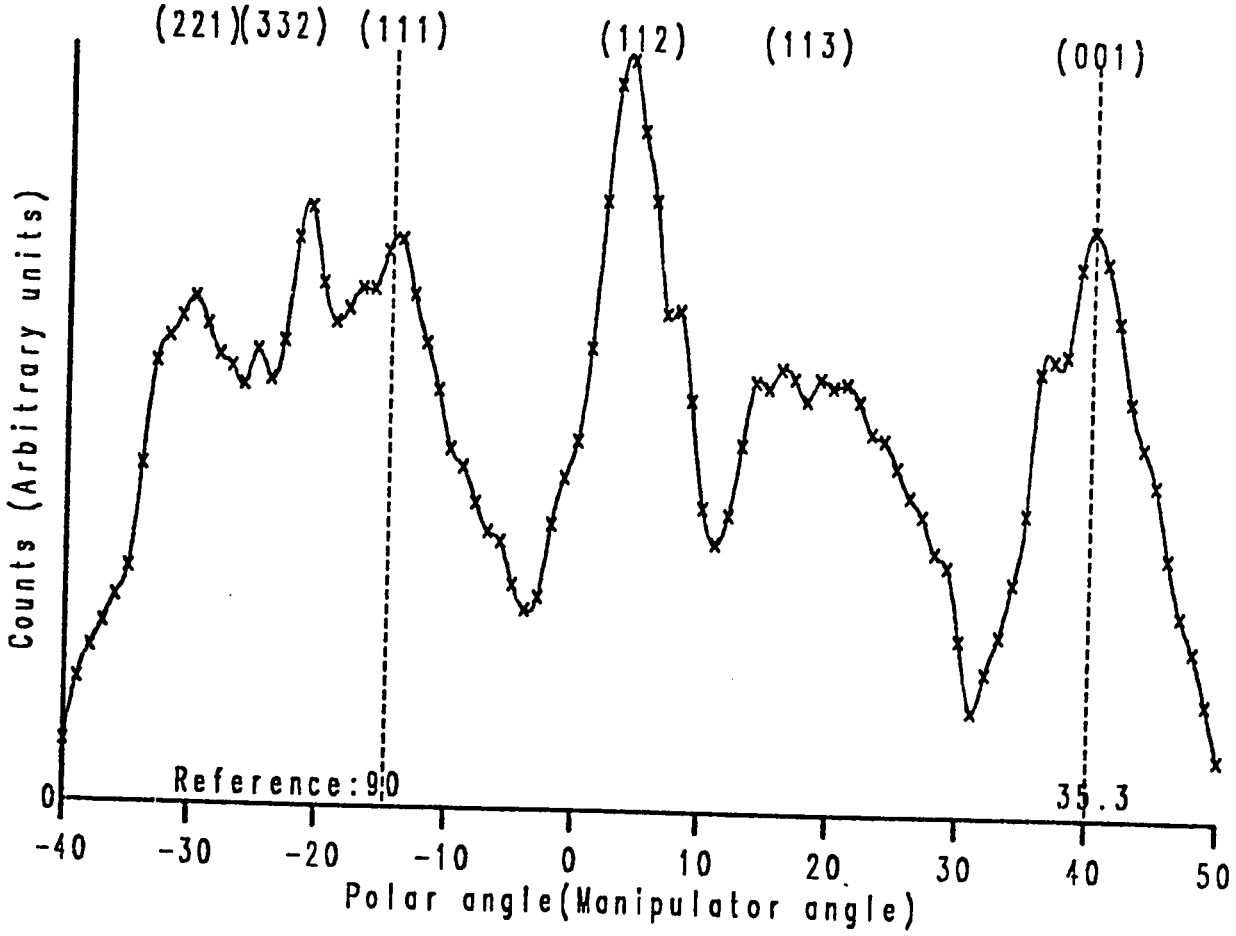

Fig.(IV-15): Raw experimental XPD data for 90° polar scan of Ir4f photoelectron intensity at azimuthal angle of 0° corresponding to the high symmetry [112] line.

along the high symmetry (11Z) line is shown. As seen from these high resolution XPD curves the angular separation of the peaks in the Ir4f have been compared to the interplanar angles of the low-index planes in the cubic lattice and as shown there is a good agreement. This method allows an anambiguous alignment of the crystal axes with an accuracy of less than 1.0°.

CHAPTER V

DATA ACQUISITION AND HANDLING

5.1 EXPERIMENTAL PROCEDURE:

Valence-band photoelectron spectra are taken at four different temperatures (120K, 295K, 480K and 630K) for high angular resolution measurements (with channel-plate in place) and for the lower angular resolution spectra with a single aperture of $\pm 6.0^{\circ}$ which is the standard acceptance angle for the instrument.

Before carrying on any experiment on the valence band structure, the contamination rate of the Iridium surface as a function of time, at different temperatures was measured. The run-time for experiments was set according to this rate. The cleanliness of the sample is monitored before and after each run by checking the Carbon and Oxygen 1s photoemission lines associated with the absorbed surface layer. For ambient temperature (295K) no contaminants were observed either before or after the valence measurements. In runs at high temperatures, the residual carbon and oxygen signals detected after their completion, correspond to only a small

fraction of a monolayer of contamination as calculated using the fractional monolayer coverage model [34]. This was found not to affect the reproducibility of spectral changes with temperature to within statistical errors. In low temperature scans, the run-time is set shorter than at other temperatures because contamination tend to accumulate quickly on the frozen sample. At this temperature the only detectable impurity after each run was oxygen, however, its amount was very small . It should be stated here that the photoemission cross sections of both oxygen and carbon in the valence level are very low compared to those of the Iridium peaks in the same region. Because of this fact and the high degree of bulk sensitivity in XPS experiments at relatively high polar angle (θ) values, the impurity levels detected should have a negligible effects on the valence band spectra.

Each experimental run for a particular emission direction is conducted more than once. The sample temperature is varied from run to run without a systematic way of increase or decrease. All the spectral variations noted with temperatures were reversible and reproducible.

The excitation X-ray gun was fed with the same electrical power to insure the same photons flux in all runs. For each direction studied, care was taken to move the sample in and out of the main chamber for cleaning procedures with the minimum translations. In most cases only the Z-translation was varied. For each repeated run the sample was positioned at the same coordinates as in the previous similar runs.

In each run a photoemission spectrum of Ir4f peaks is taken. The Fermi level in then specified in all spectra with respect to the $Ir4f_{7/2}$ binding energy, which is taken to be 60.8 eV [59].

5.2 DATA ACQUISITION PROCEDURE:

Data for all spectra were accumulated at fixed constant pass energy of the analyzer of 10 eV. The width of each scan is 16 eV with run-steps of 0.1 eV. The collection time of each step (channel) is one second. Each run, consists of many scans divided into scanning regions, lasted one or two hours. Data of all regions for all runs in each experimental set are added. All spectra at room and higher temperatures were accumulated to a minimum of $\sim 10^4$ counts full scale. At T = 120K the spectra were accumulated to $\sim 0.5\text{-}0.75\ 10^4$ counts full scale. The inelastic background at low energies is subtracted using the VGS 5000 data system software routines for that purpose. These are based on Shirley's methods [60] and the algorithm of Procter and Sherwood [61]. The data was subsequently smoothed using appropriate routines of the same data system software which contain 3, 5 or 7 point smoothing routines [62] and extended smoothing routines which are using either quadratic/cubic or quadratic/quintic function following the algorithm of Proctor et al. [63]. The smoothing method used for all our data was the quadratic/cubic method in which the values for the end points are extrapolated in such a way that no data points are lost. This is found not to alter the spectral features at all.

5.3 THEORETICAL DATA COMPUTATION:

5.3.1 Computation of ARP spectra:

For the computation of theoretical angle-resolved spectra from the Iridium single crystal a direct transition program with feed-back loop appropriate to face-centered crystals is used.

The input eigenvalues of the energy band $E_i(\vec{k})$ were found by a fully relativestic first-principles band structure calculation given by J. Noffke and L. Fritsche [64]. This band structure as reported in their work is shown in Figure (V-1). 89 k-points in the irreducible wedge of the Brillouin Zone (1/48 of the BZ) are used. The remaining eigenvalues in the total BZ are found by the use of symmetry properties [65].

Calculations are based on strict conservation of energy and wave vector, and include summations over a uniform two dimensional distribution of 380 points within a disk in BZ to account for angular broadening as shown in Figure (IV-1). The resulting theoretical curves are finally broadened with a Gaussian function of FWHM of 0.4 eV to account for experimental resolution.

5.3.2 Theoretical Separation of DT and NDT components from experimental data:

From Eq. (1-2)

$$I(E,T) = W(T)I_{DT}(E) + [1 - W(T)]I_{NDT}(E) \qquad (5\text{-}1)$$

Any two spectra at different temperatures, T_1 and T_2 can be used to isolate the $I_{DT}(E)$ and $I_{NDT}(E)$.

For each temperature W(T) is calculated from Eq. (1-1). Hence, writing the above equation for T_1 and T_2 :

$$I(E, T_1) = W(T_1)I_{DT}(E) + [1 - W(T_1)]I_{NDT}(E) \tag{5-2}$$

$$I(E, T_2) = W(T_2)I_{DT}(E) + [1 - W(T_2)]I_{NDT}(E) \tag{5-3}$$

we get:

$$I_{DT}(E) = \frac{[1 - W(T_2)]I(E, T_1) - [1 - W(T_1)]I(E, T_2)}{W(T_1) - W(T_2)} \tag{5-4}$$

$$I_{NDT}(E) = \frac{W(T_2)I(E, T_1) - W(T_1)I(E, T_2)}{W(T_2) - W(T_1)} \tag{5-5}$$

The DT and NDT components are then obtained from equations (5-4) and (5-5) using two sets of experimental data at two different temperatures.

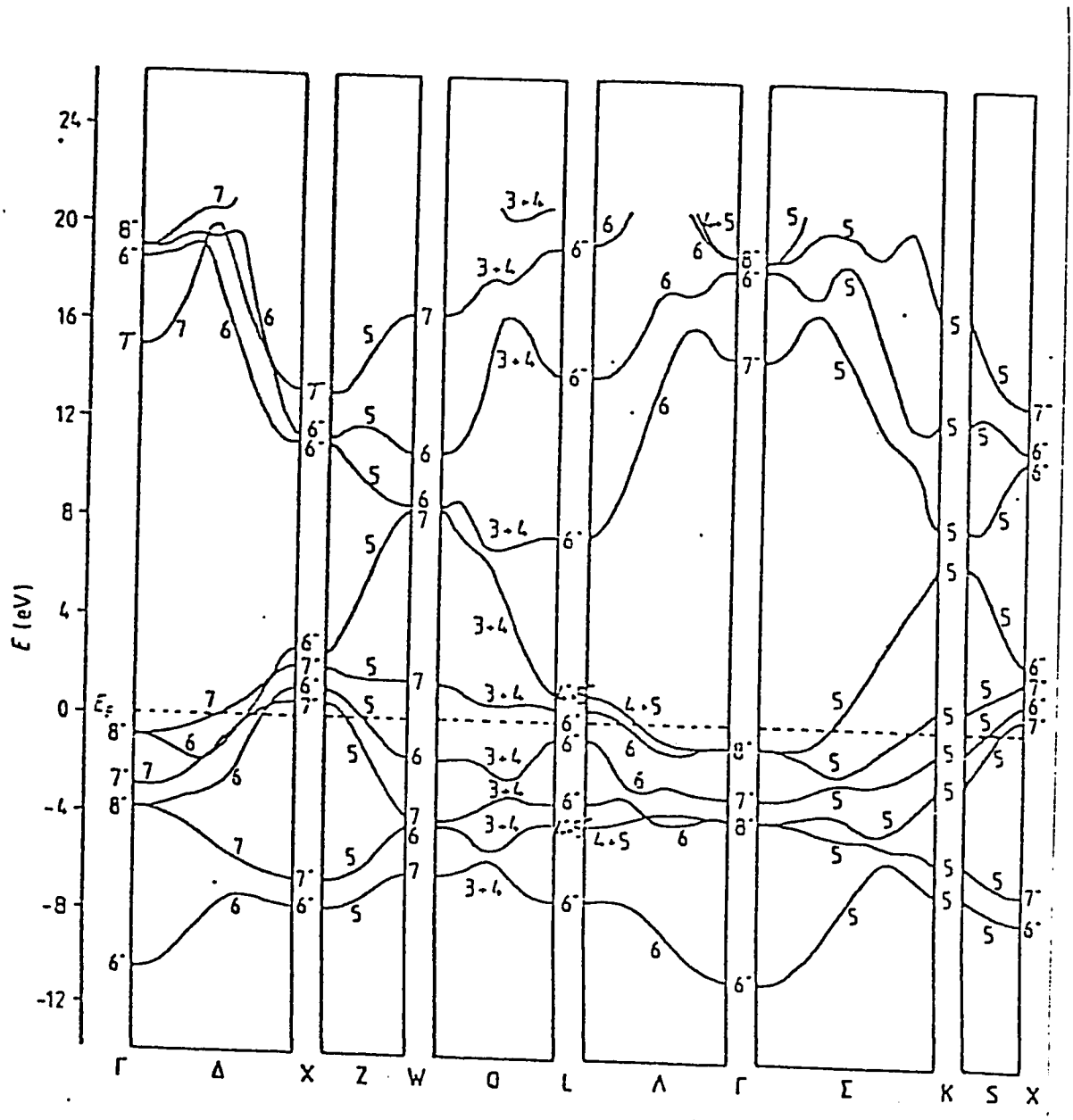

Fig.(V-1) Full relativistic band structure of Iridium metal along symmetry lines. The numbers refer to symmetry labels of the respective representations in single group notation.

CHAPTER VI

RESULTS AND DISCUSSION

6.1 TEMPERATURE DEPENDENCE OF THE VALENCE BAND SPECTRA:

The spectra we presented here have been normalized to the same constant maximum height. In figure (VI-1) through (VI-14), we show the experimental data for the valence band taken at specimen temperatures of 120K, 295K, 480K, and 630K for different polar angles θ and fixed azimuthal angle of $\varphi = 0^{\circ}$. Also given in these figures are the Debye-Waller factors (W) corresponding to each temperature. The experimental angular resolution is 1.1° for spectra in figures (VI-1) through (VI-7) and 6.0° for spectra in figures (VI-8) through (VI-14).

6.1.1 High angular resolution:

At high angular resolution , i.e. 1.1° , there are noticeable and important changes in the features of the spectra as temperature is varied and dramatic changes are observed in some spectra at the lowest temperature of 120K.

In figure (VI-1), the spectra were taken at normal emission, $\theta = 90°$. As the temperature is varied from 630K down to 295K, the peak at ~ 4 eV becomes more resolved and pronounced as compared to the peak at ~ 1.5 eV and a peak-like feature at ~ 6.5 eV becomes more broadened. At $T = 120K$ a striking change occurs to the peak at ~ 1.5 eV , it almost disappears and the valley which was at ~ 2.7 eV shifts to its place. Only a small peak at ~ 0.7 eV remains. A peak shoulder which was not present at higher temperatures spectra emerged at ~ 3 eV . The shape at ~ 6.5 eV . disappears at $T = 120K$ and seems to be shifted to larger energies, around ~ 7.5 eV .

Figure (VI-2), shows photoemission spectra at polar emission angle, $\theta = 80°$. In this region, the changes with respect to temperature looks consistent with the increase in the relative intensities of the peaks at ~ 4.2 eV and ~ 0.8 eV and a small peak feature in the valley between these two peaks at ~ 2.5 eV seems to be shifted to ~ 2 eV at $T = 120K$. Also the highest peak in the spectra which was at ~ 4.2 eV for high temperatures is shifted to ~ 4 eV at $T = 120K$. The tail of this peak at ~ 7 eV becomes more resolved as the temperature is decreased.

In figure (VI-3), the photoemission spectra were taken at polar emission angle, $\theta = 70°$. The main changes noted as temperature is varied from 295K to 630K are in the relative intensities of the peaks at ~ 4.1 eV and ~ 1.9 eV . Also, the shoulder at ~ 1 eV tends to disappear as temperature increases. At $T = 120K$, a striking change of the peak at

~2.1 eV occurs. This peak disappears at this low temperature and a peak at ~2.75 eV appears. The peak at ~4 eV and the shoulder at ~1 eV are more resolved. The feature at ~6.5 eV , like in the previous region, seems to be shifted to higher binding energies at ~7.3 eV at T = 120K.

Almost similar changes, the ones observed at $\theta = 70°$ in figure (VI-3), occur at $\theta = 60°$, in figure (VI-4) as temperature is varied. The relative intensities of the peaks at ~4 eV and ~1.5 eV changes as the temperature is increased from 295K to 630K. The shoulder at ~1 eV merges with the peak at ~1.5 eV at high temperatures. This large peak is cut short at T = 120K and the peak at ~4 eV is more resolved at this temperature. Similar change occurs, as previously, to the feature at ~6.5 eV .

The changes in the spectra in figure(VI-5) at $\theta = 50°$, with temperature are less dramatic than those in figure (VI-4). There is a change in the relative intensities of the peaks at ~4.1 eV and ~1.8 eV . The peak at ~1.8 eV is broadened progressively as the temperature is raised from 295K to 630K but at 120K it is not sharper than it was at 295K. The peak at ~4 eV is broadened at 120K and shifted to higher binding energies at ~4.5 eV. The feature at ~6.2 eV is increasingly resolved as temperature in decreased.

In figure (VI-6) with polar emission angle $\theta = 40°$, there are noticeable changes of the intensity of the peaks at ~1 eV and ~4 eV, a peak at ~2 eV is more apparent at T = 120K.

In the last region where $\theta = 35°$, only 5° less than the polar emission angle in the previous region, there are marked changes of the relative intensities of the peaks at ~ 4 eV and the peak at lower binding energy which is changing from a broad peak at ~ 1.5 eV for the spectrum at $T = 630$K to a peak at ~ 2.5 eV and a shoulder at ~ 0.6 eV. This peak at ~ 2.5 eV is shifted to lower energy of ~ 2 eV at $T = 120$K and its shoulder is still present but less resolved. The feature at ~ 6.5 eV is increasingly resolved as temperature is decreased.

Thus, all the spectra at high angular resolution show a very sensitive temperature dependence. There are also great changes in spectra of the same region at the lowest temperature (120K). This shows the important phonon effect on the XPS valence bands spectra which are present even at room temperature.

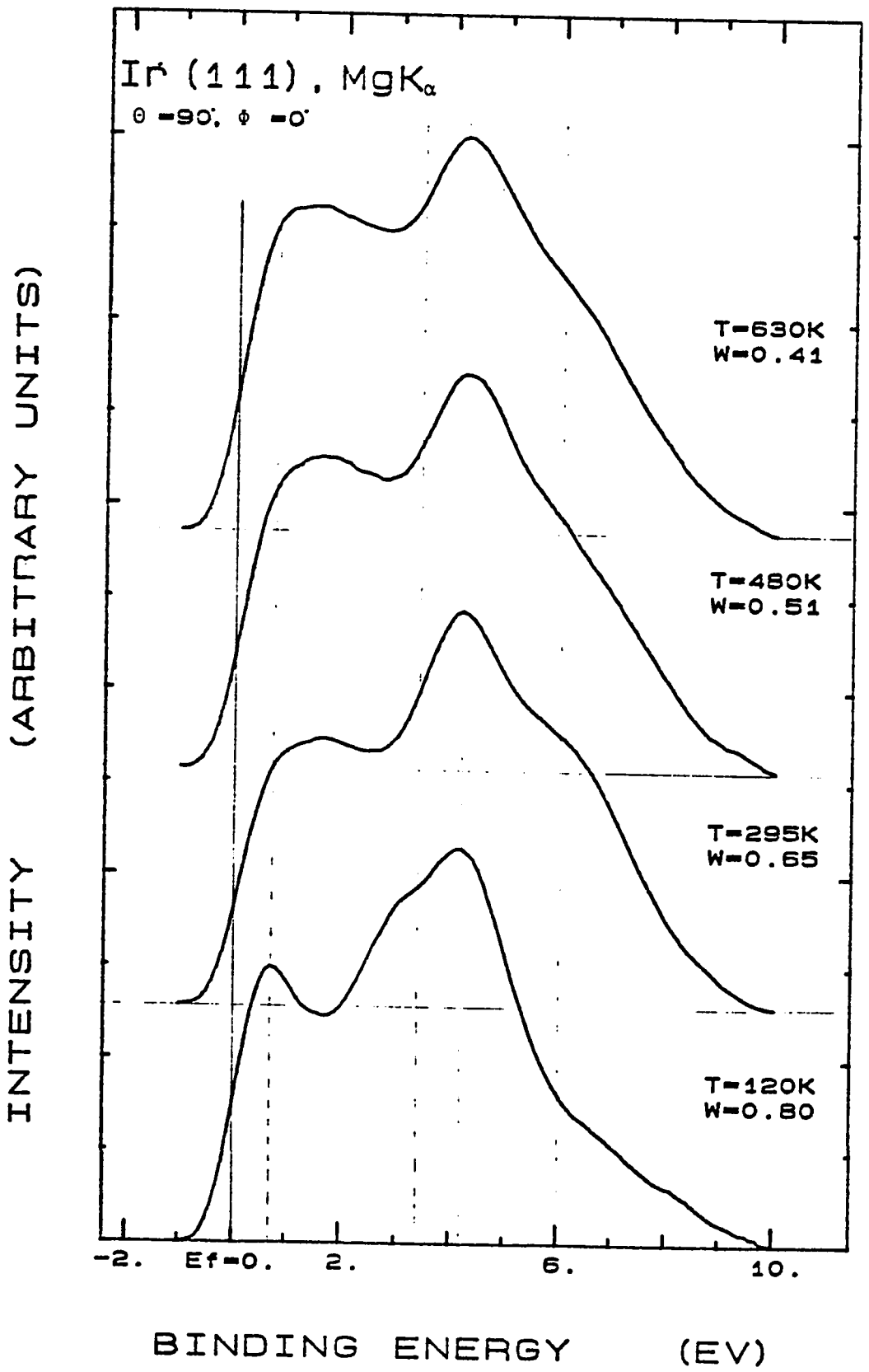

Fig. (*VI-1*): Temperature dependence of Iridium valence-band spectra taken at high angular resolution $\alpha = \pm 1.1°$ for emission angle $\theta = 90°$ and $\varphi = 0°$. The temperatures and their associated Debye-Waller factors (W) are given in the figure.

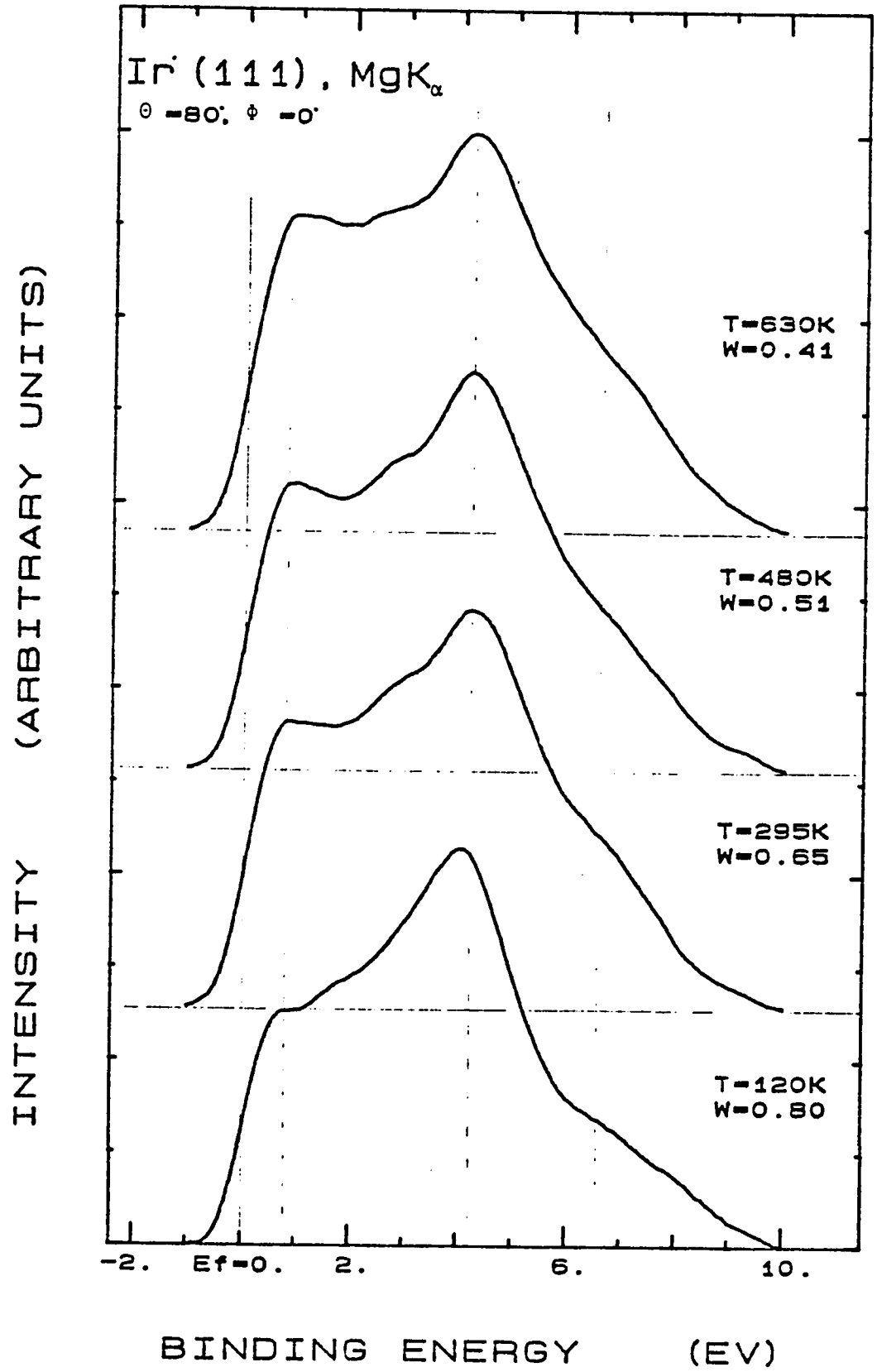

Fig. (*VI-2*): Temperature dependence of Iridium valence-band spectra taken at high angular resolution $\alpha = \pm 1.1°$ for emission angle $\theta = 80°$ and $\varphi = 0°$. The temperatures and their associated Debye-Waller factors (W) are given in the figure.

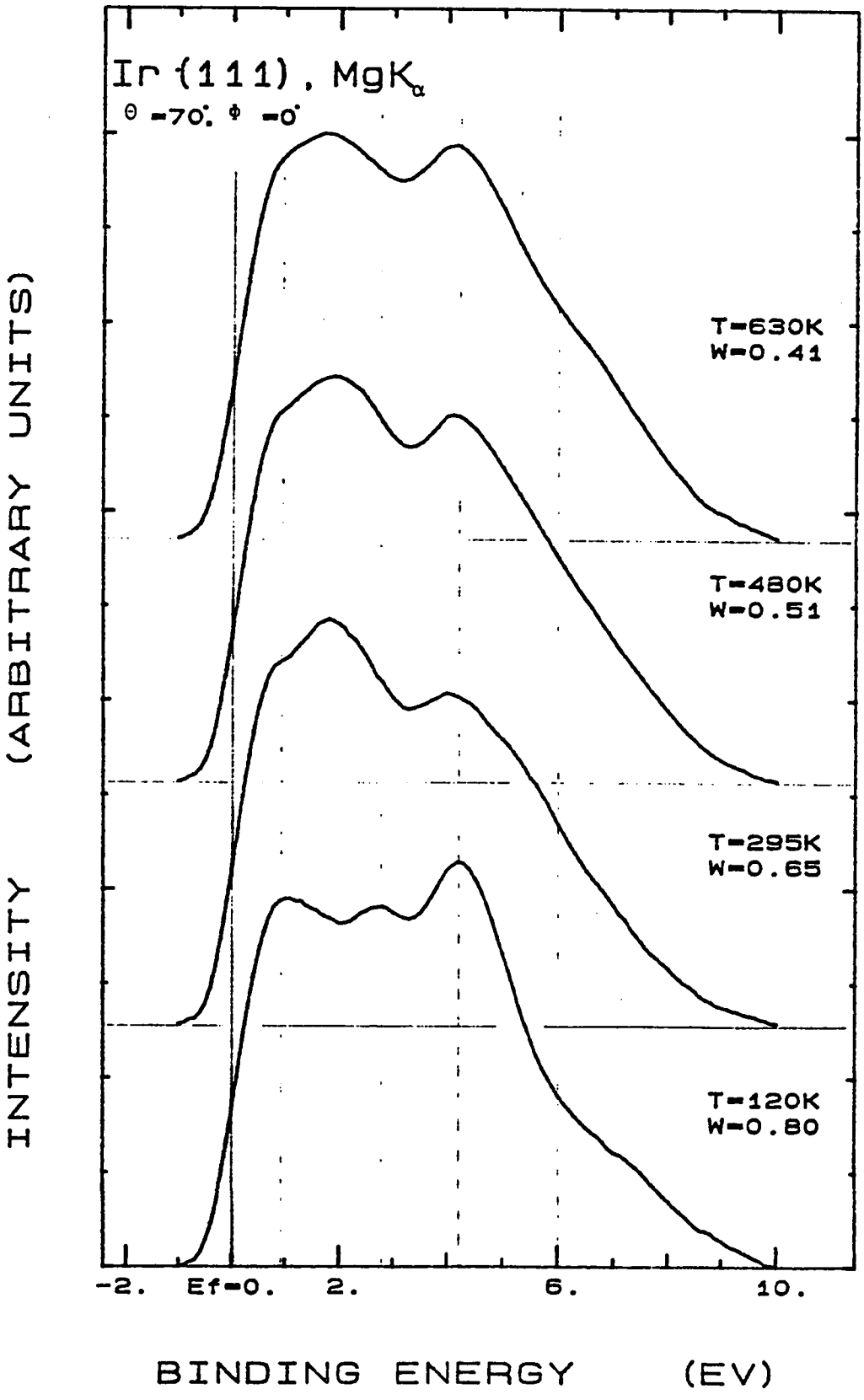

Fig. (*VI-3*): Temperature dependence of Iridium valence-band spectra taken at high angular resolution $\alpha = \pm 1.1°$ for emission angle $\theta = 70°$ and $\varphi = 0°$. The temperatures and their associated Debye-Waller factors (W) are given in the figure.

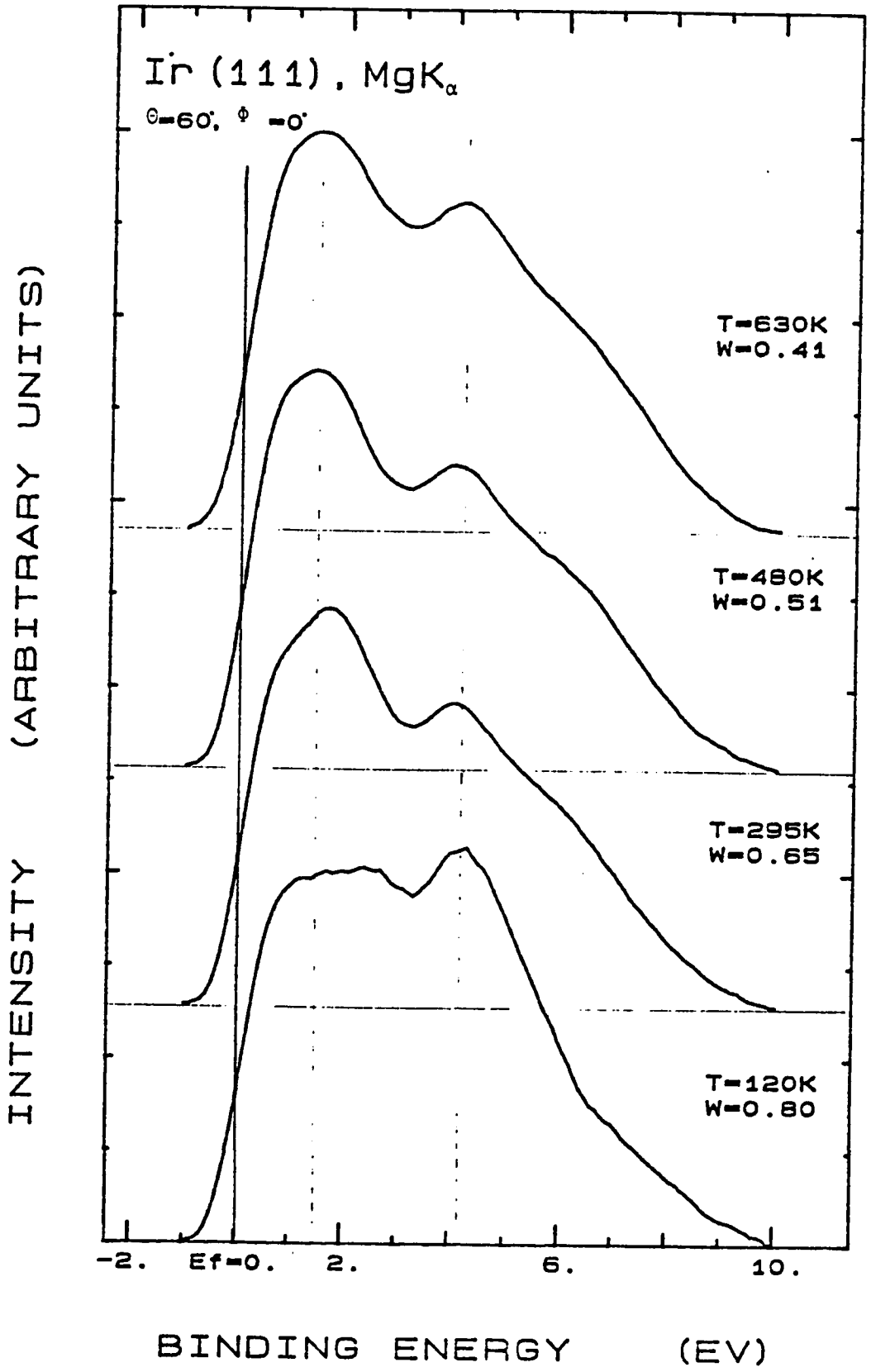

Fig. (*VI-4*): Temperature dependence of Iridium valence-band spectra taken at high angular resolution $\alpha = \pm 1.1°$ for emission angle $\theta = 60°$ and $\varphi = 0°$. The temperatures and their associated Debye-Waller factors (W) are given in the figure.

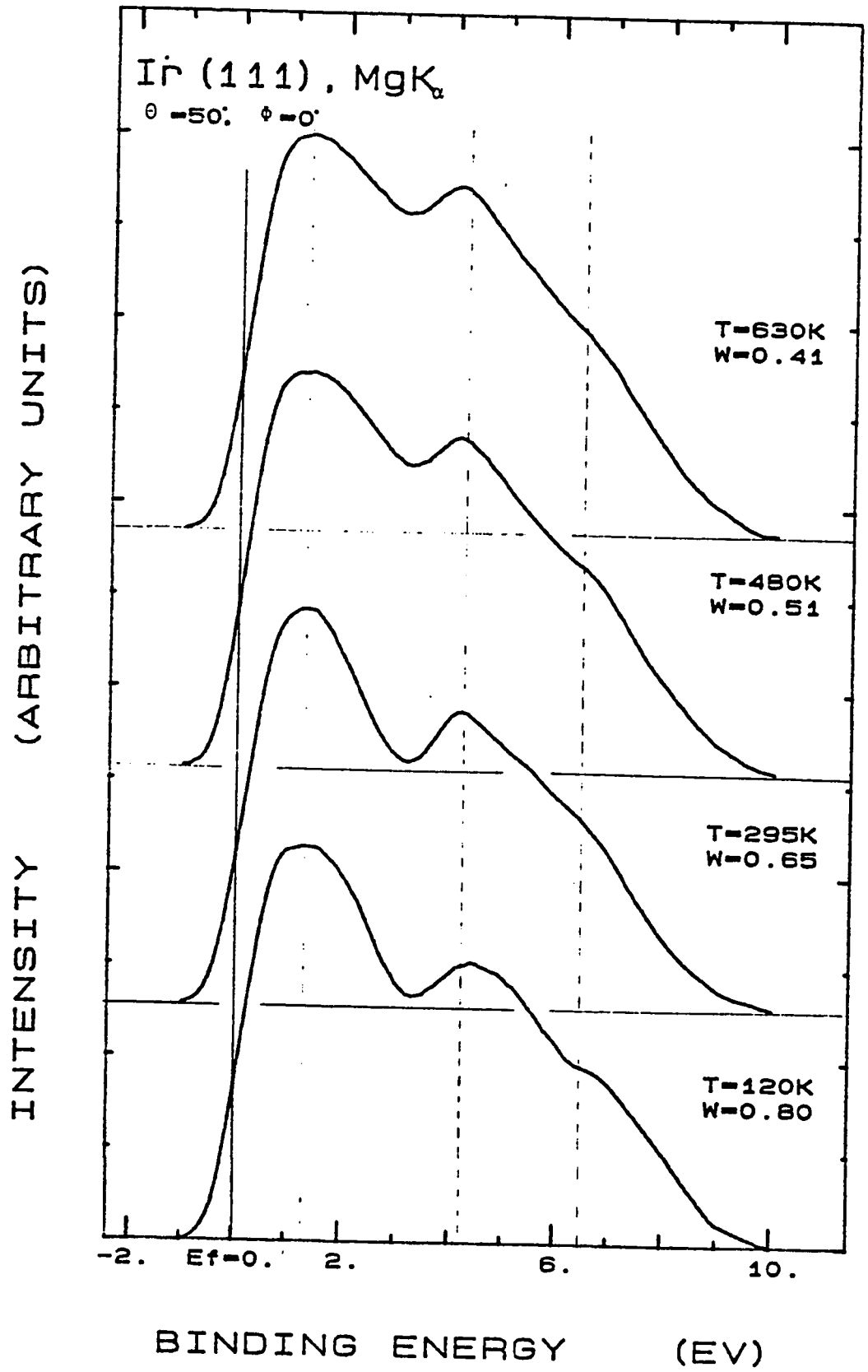

Fig. (*VI-5*): Temperature dependence of Iridium valence-band spectra taken at high angular resolution $\alpha = \pm 1.1°$ for emission angle $\theta = 50°$ and $\varphi = 0°$. The temperatures and their associated Debye-Waller factors (W) are given in the figure.

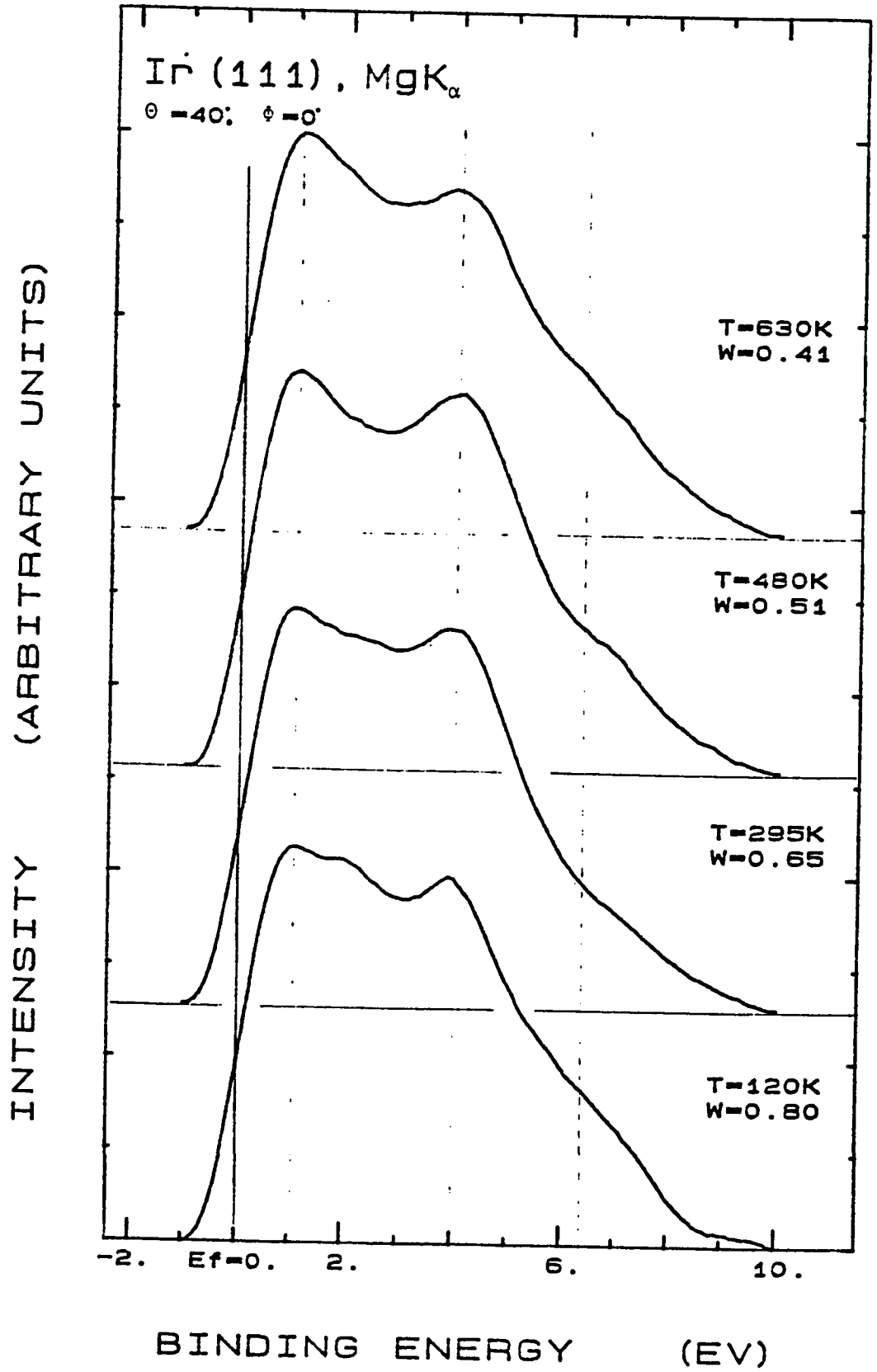

Fig. (*VI-6*): Temperature dependence of Iridium valence-band spectra taken at high angular resolution $\alpha = \pm 1.1°$ for emission angle $\theta = 40°$ and $\varphi = 0°$. The temperatures and their associated Debye-Waller factors (W) are given in the figure.

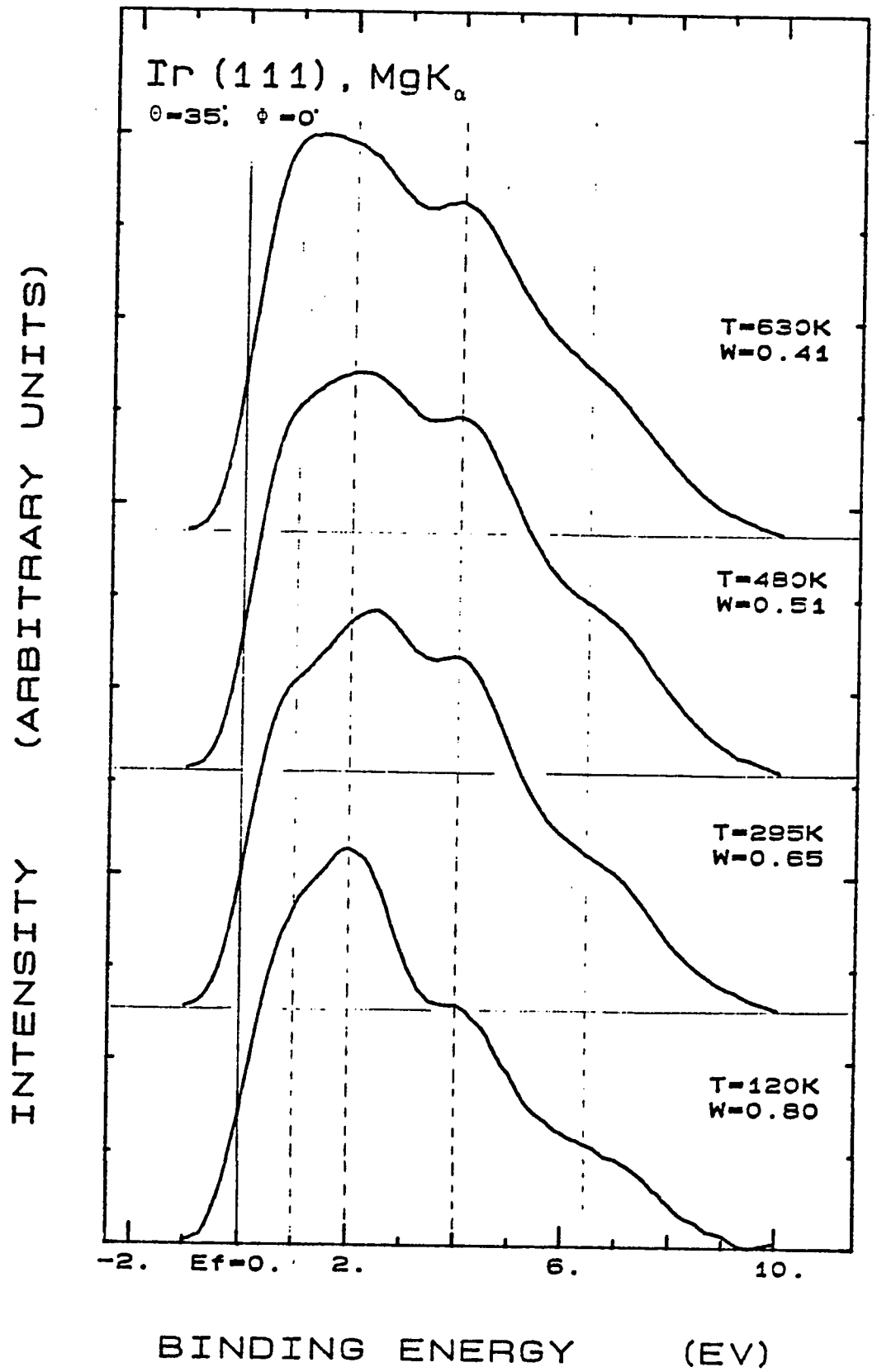

Fig. (*VI-7*): Temperature dependence of Iridium valence-band spectra taken at high angular resolution $\alpha = \pm 1.1°$ for emission angle $\theta = 35°$ and $\varphi = 0°$. The temperatures and their associated Debye-Waller factors (W) are given in the figure.

6.1.2 Low angular resolution:

In figures (VI-8) through (VI-14), we show photoemission spectra of the same regions as in figures (VI-1) through (VI-7) but with low angular resolution of 6.0°. All the spectra at this angular resolution, in general, have three components at ~1.5 eV, ~4 eV and ~6.5 eV. But no perceptible change is observed as temperature is varied from T = 120K to 630K in all the different regions investigated. These spectra resembles the density of states (DOS) as reported by N. V. Smith et al. [66]. All the features present in our spectra of low angular resolution are similar to those in the DOS (Figure (VI-15)) except at larger polar emission angles where the peak at ~1.5 eV is less resolved. This only difference happened at larger polar emission angles $\theta = 90^0$ and $\theta = 80^0$ could be attributable to surface specific effects caused by the enhanced surface sensitivity where the mean emission depth is lower as compared to that at smaller angles.

Hence, at angular resolution of 6.0°, the curves resembles the DOS, suggesting nearly complete averaging over the Brillouin zone. This explains the temperature independence of the valence band spectra at this low angular resolution.

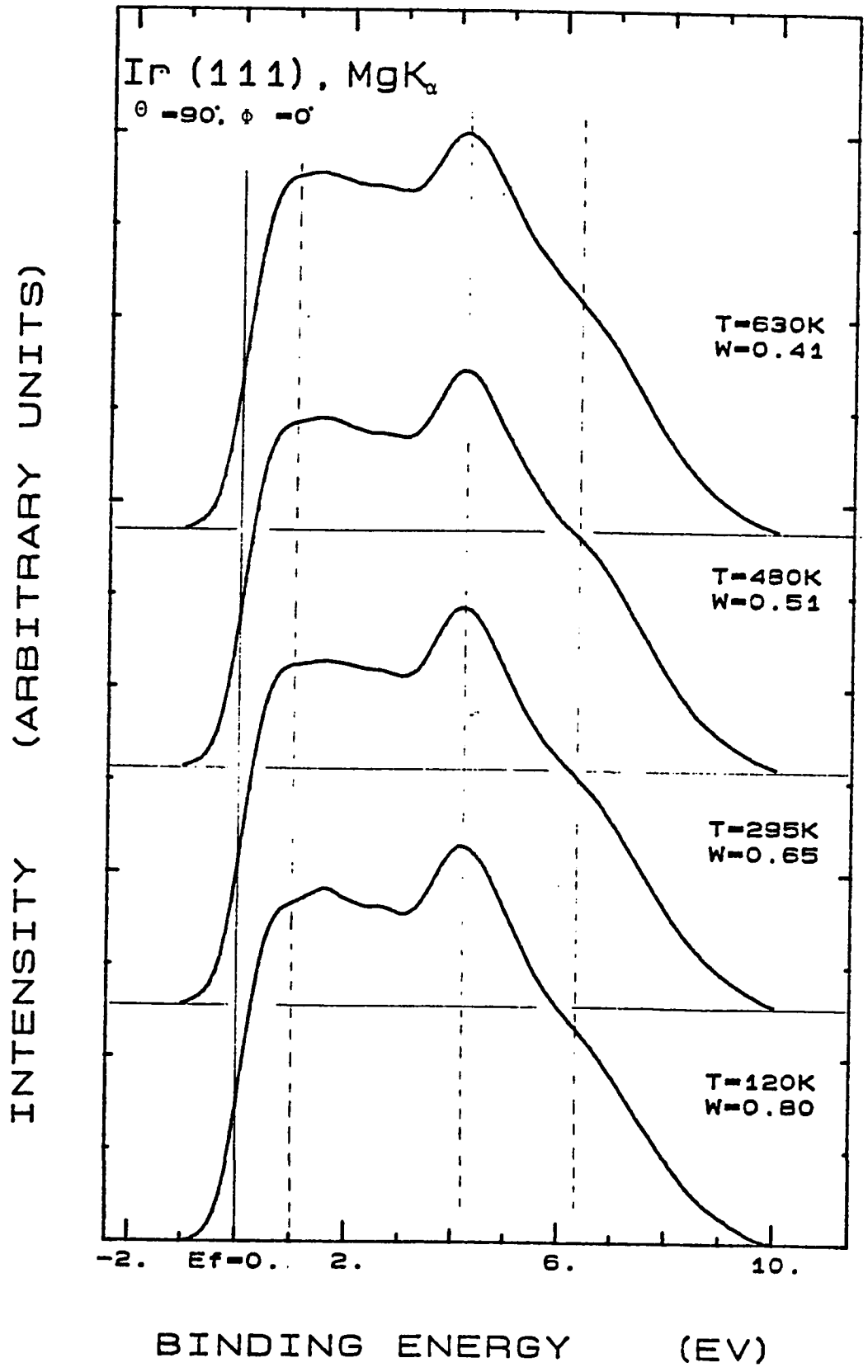

Fig. (*VI-8*): Temperature dependence of Iridium valence-band spectra taken at low angular resolution $\alpha = \pm 6.0°$ for emission angle $\theta = 90°$ and $\varphi = 0°$. The temperatures and their associated Debye-Waller factors (W) are given in the figure .

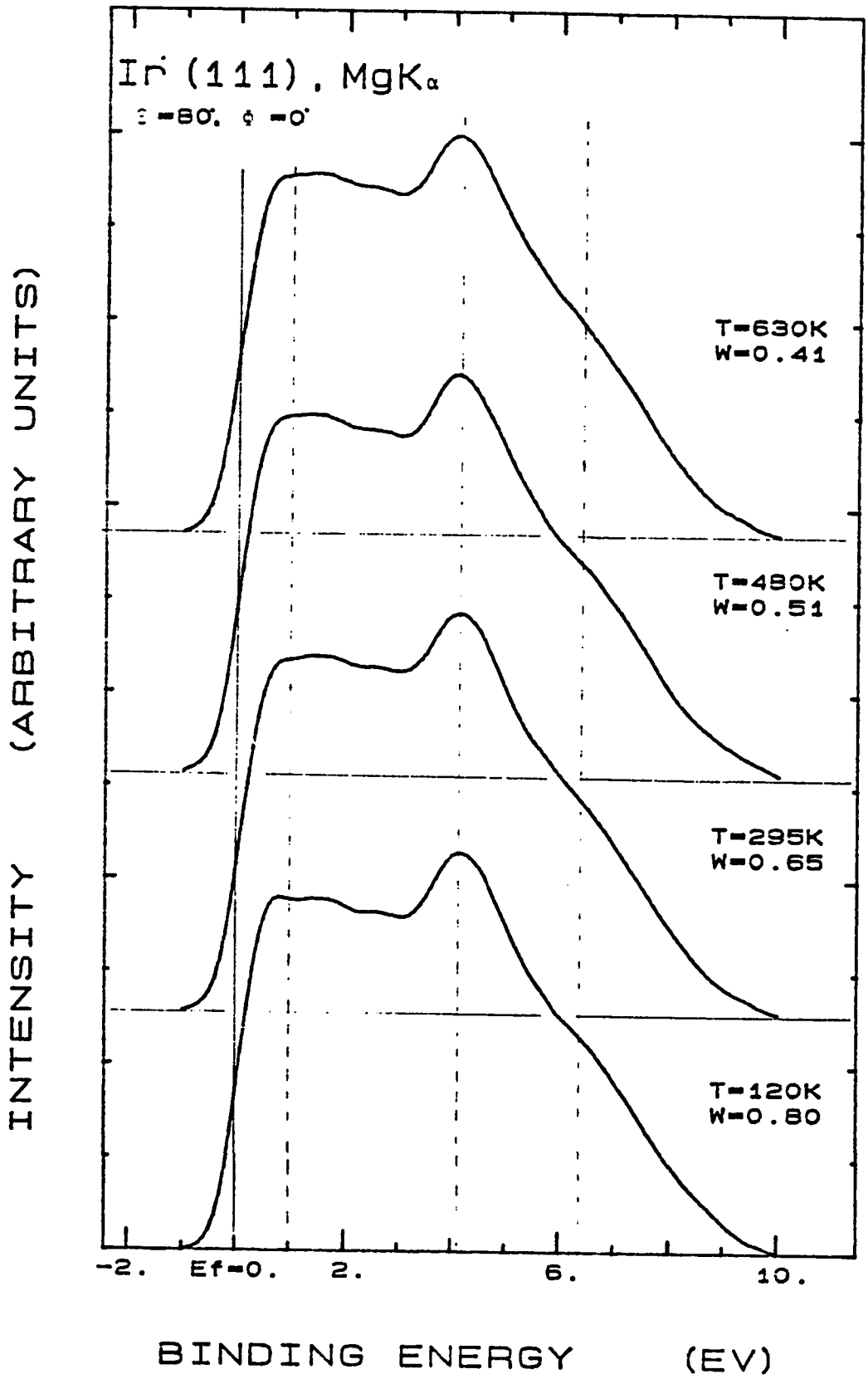

Fig. (*VI-9*): Temperature dependence of Iridium valence-band spectra taken at low angular resolution $\alpha = \pm 6.0°$ for emission angle $\theta = 80°$ and $\varphi = 0°$. The temperatures and their associated Debye-Waller factors (W) are given in the figure .

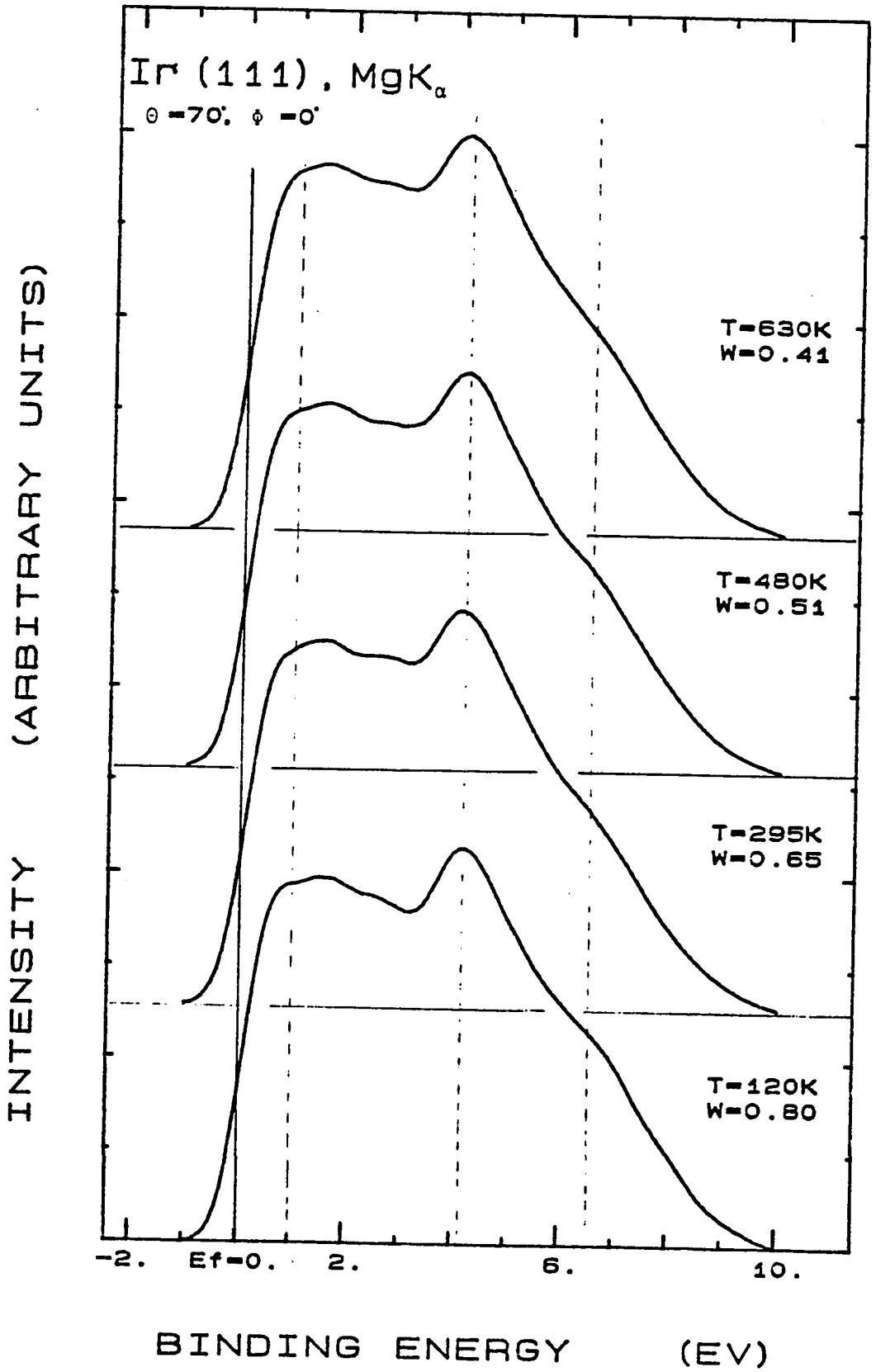

Fig. (*VI-10*): Temperature dependence of Iridium valence-band spectra taken at low angular resolution $\alpha = \pm 6.0°$ for emission angle $\theta = 70°$ and $\varphi = 0°$. The temperatures and their associated Debye-Waller factors (W) are given in the figure .

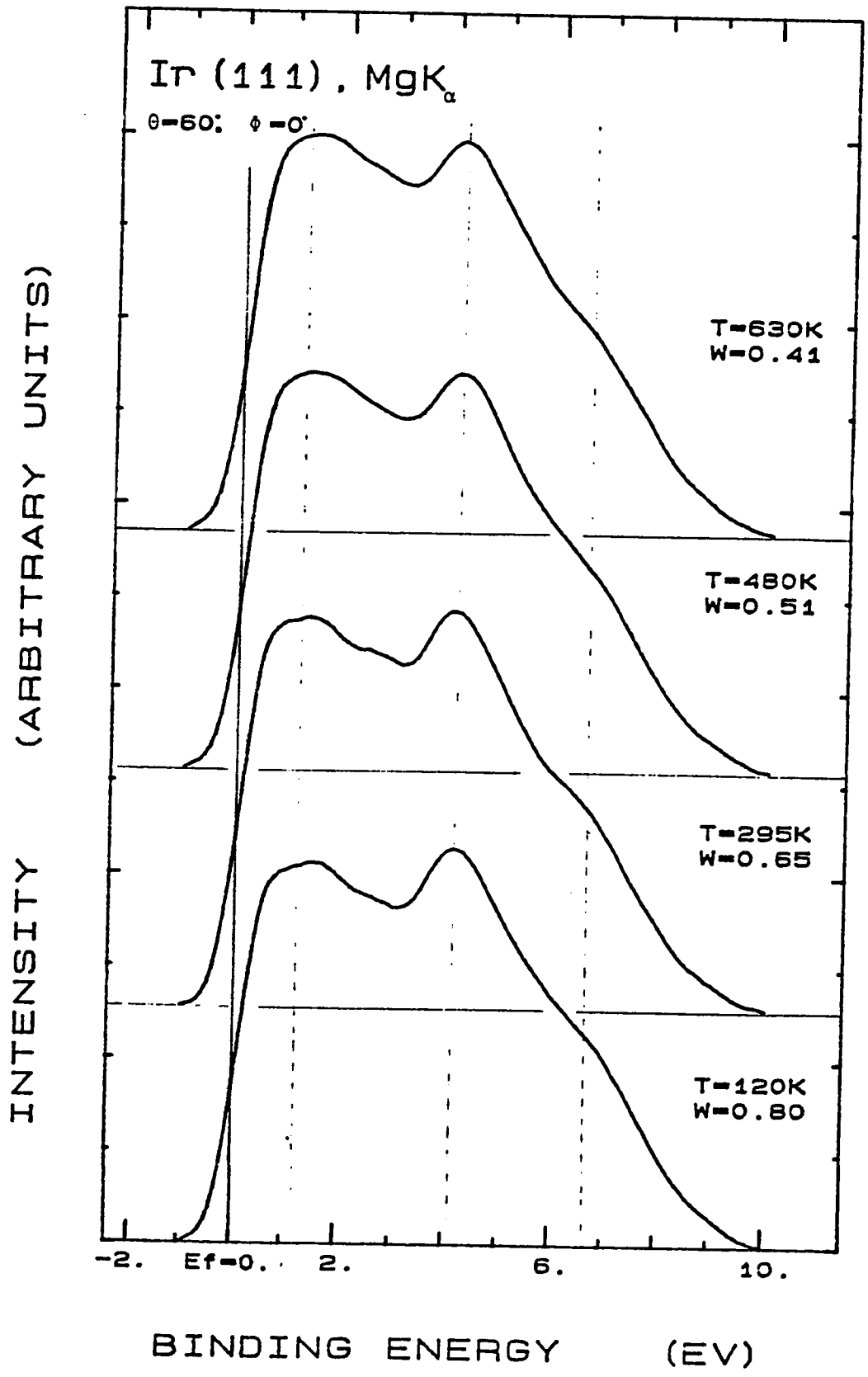

Fig. (*VI-11*): Temperature dependence of Iridium valence-band spectra taken at low angular resolution $\alpha = \pm 6.0°$ for emission angle $\theta = 60°$ and $\varphi = 0°$. The temperatures and their associated Debye-Waller factors (W) are given in the figure.

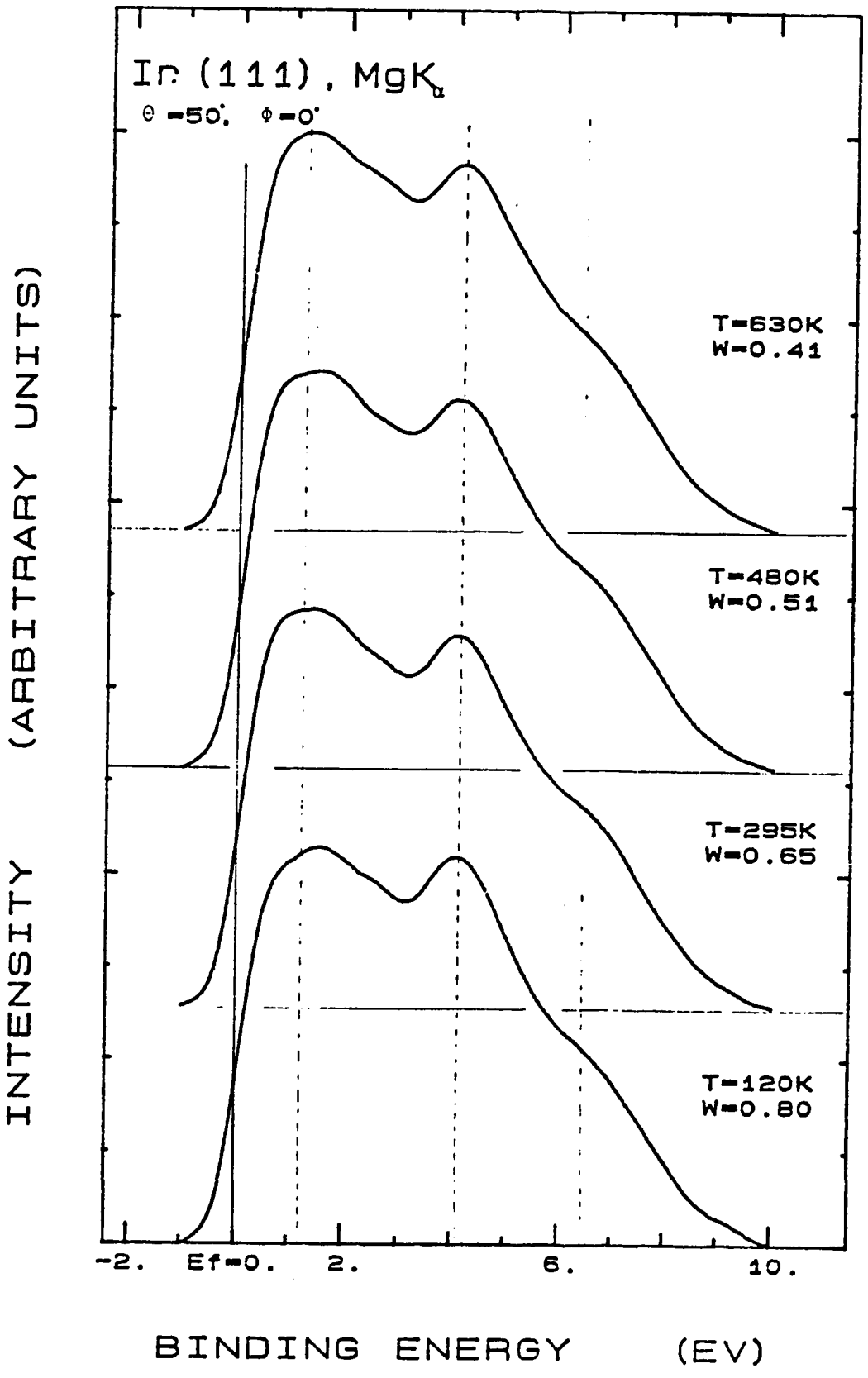

Fig. (*VI-12*): Temperature dependence of Iridium valence-band spectra taken at low angular resolution $\alpha = \pm 6.0°$ for emission angle $\theta = 50°$ and $\varphi = 0°$. The temperatures and their associated Debye-Waller factors (W) are given in the figure .

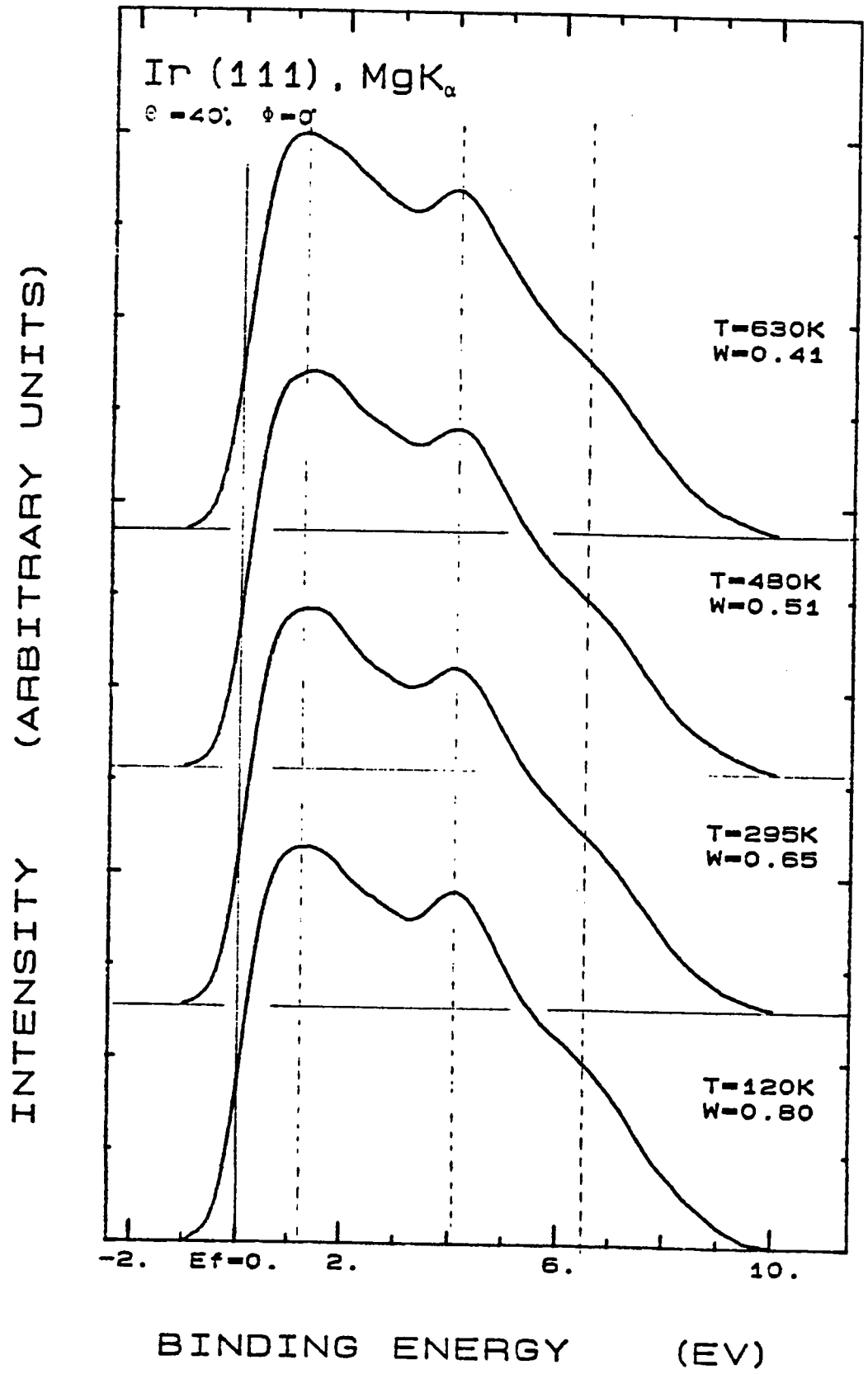

Fig. (*VI-13*): Temperature dependence of Iridium valence-band spectra taken at low angular resolution $\alpha = \pm 6.0°$ for emission angle $\theta = 40°$ and $\varphi = 0°$. The temperatures and their associated Debye-Waller factors (W) are given in the figure .

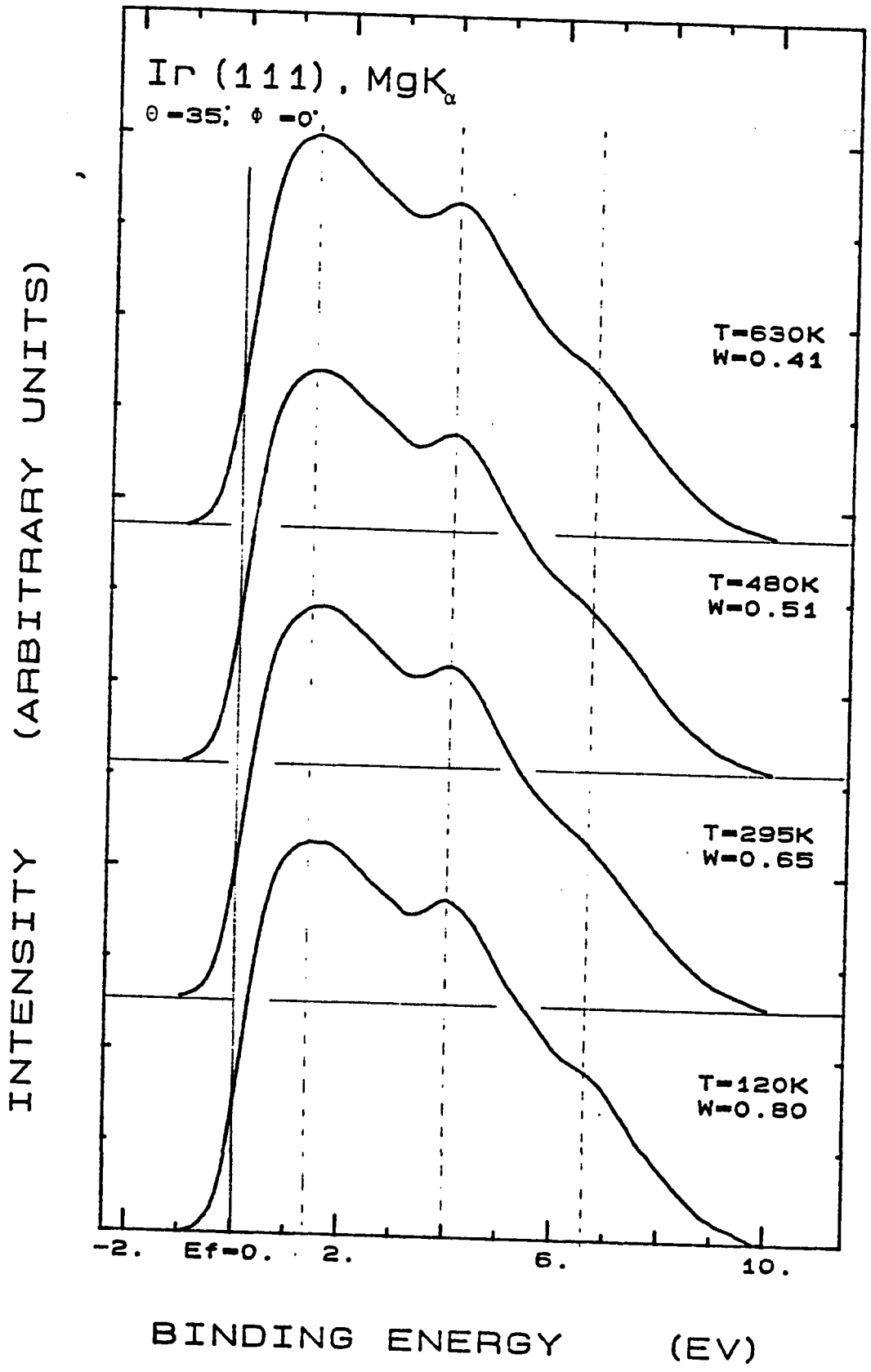

Fig. (*VI-14*): Temperature dependence of Iridium valence-band spectra taken at low angular resolution $\alpha = \pm 6.0°$ for emission angle $\theta = 35°$ and $\varphi = 0°$. The temperatures and their associated Debye-Waller factors (W) are given in the figure .

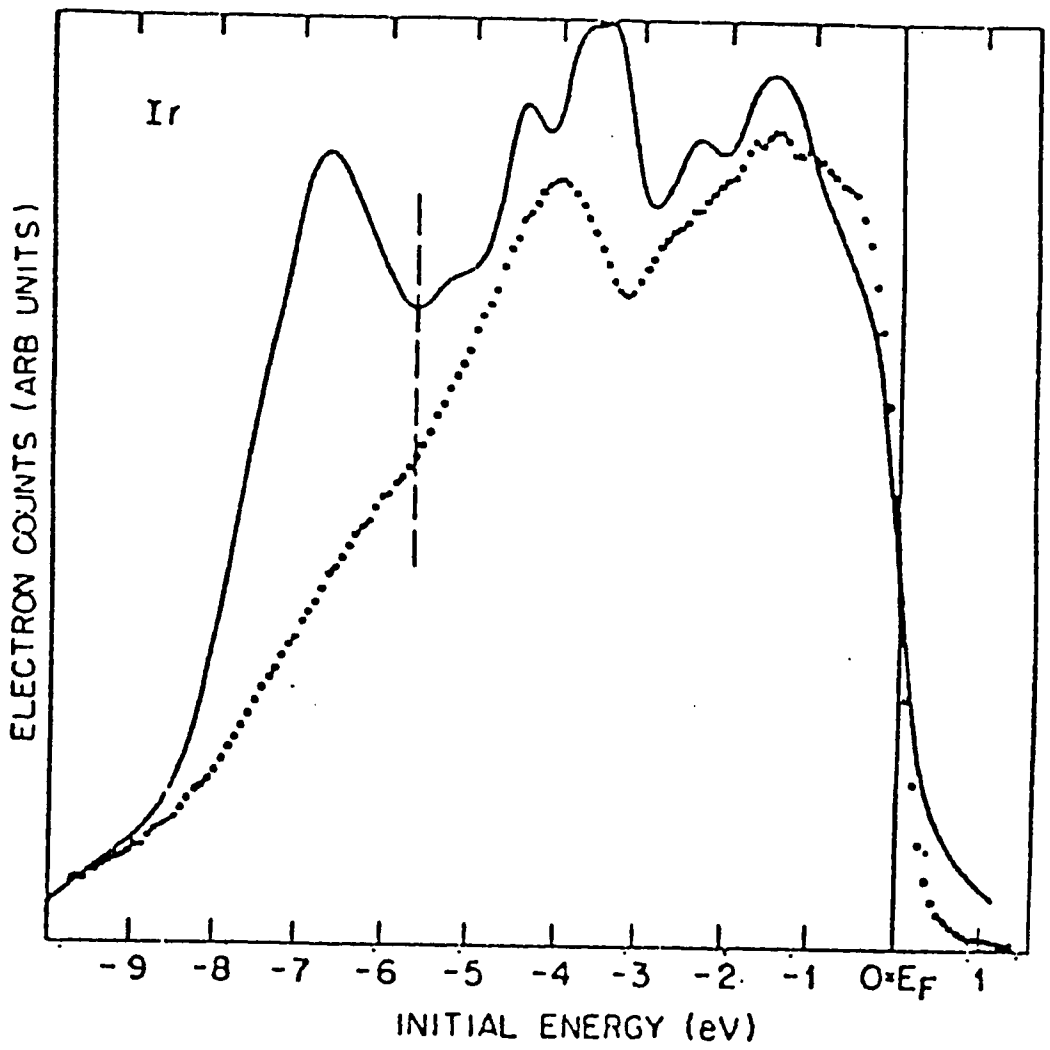

Fig. (*VI-15*): Experimental XPS data on Ir (closed circles) compared with a smoothed version of the occupied DOS [66].

6.2 VALIDITY OF SHEVCHIK'S NDT MODEL:

As previously discussed in chapter II, Shevchik's NDT model results in Eq. (2-13) where each spectrum at any particular temperature is a sum of temperature independent component $I_{DT}(E)$ and a NDT component $I_{NDT}(E)$ weighted by the Debye-Waller factor (W(T)) and (1-W(T)) respectively. Hence any two spectra at different temperatures T_1 and T_2 can be used to isolate these components. The components extracted in such a way should be the same and do not depend on the pair of temperatures T_1 and T_2 utilized. The accuracy is expected to improve as the temperature difference between T_1 and T_2 increases.

This method was first tested experimentally by Hussain et al. [3,5] for AR-XPS measurements on Tungsten. They obtained a full self consistent decomposition into DT and NDT components for all pairs of spectra obtained at two different temperatures with angular resolutions of 3.0°. The same method was tested by White et. al. [10] on the same element but with a higher angular resolution of 1.0°. Furthermore White et al. found that the the DT component isolated via this method may still contain significant NDT contributions.

In our study on Iridium, we applied this method to seven distinctly different directions. Figures (VI-16) through (VI-22) illustrate such decomposition into DT and NDT components. It is found to yield almost fully consistent results for all the DT components and to some extent for

the NDT components extracted from spectra at two different temperatures corresponding to a large difference in the Debye-Waller factors. It is also found that there are some discrepancies in both components when the extraction is done with a pair of spectra at close temperatures.

The DT components extracted from each region resemble spectra taken at the lowest temperature. The DT components are only slightly sharpened compared to the corresponding lowest temperature spectra. The NDT components when extracted from spectra at large difference in temperatures resemble, but not completely, the corresponding high temperature spectra.

The close resemblance of the DT component and the lowest temperature spectra is expected as a result of this NDT model, since W at T=120K for Iridium is 0.8 therefore 80% of the spectrum are DT and only 20% are NDT. Results by Hussain et al. [3,5] and White et al. [10] have shown a similarity between the NDT components and the DOS. This is not the case here where we find the NDT components to differ from one region to the other and not resemble the DOS. This could be explained by the largest temperature used in their study which is 1000K compared to only 630K used in our study. The Debye-Waller factor for Tungsten at 1000K is only 0.14, hence 86% from the highest temperature spectra are expected to be NDT. In our case this factor is only 59% which suggests that the spectrum at 630K still contains non negligible DT components (41%). But if it were true that the NDT component should resemble the

DOS, Then we should have reached the same result as theirs since the largest difference in the Debye-Waller factors we used here is similar to theirs which is ~0.4. The same resemblance between NDT and DOS has been noted by Jezequel et al.[67] in their UPS work on Pb at excitations of 70 eV but in a later work on Cu by White et al. [14,32] at excitations $41 \leq h\nu \leq 106$ eV the NDT are found to be different from the DOS.

This controversy in results together with the discrepancies noted in our work and in previous works in the extraction of DT and NDT components via Eq.(2-13) using pairs of temperatures of small difference call to question the validity of Shevchik's NDT model.

From our present study, and previous works [3,5,10,14,32,67], we find that the self consistency in extracting DT and NDT components via this model had been successful only when experimenting with small angular resolutions. Figures (VI-23) and (VI-24), show an example of such self consistency obtained from spectra taken at an angular resolution of 6.0°. This was tested for all pairs of spectra of each region at low angular resolution (Figures (VI-7) through (VI-14)) and was found to yield similar consistencies. The same result, as noted before, is also obtainable when very large difference of temperatures is used and also when the change of the valence band spectra differs slightly with temperature from a lower temperature to the next higher temperature, i.e., when no dramatic changes in the spectra occur at low temperatures.

The unsuccess of this model could be attributed to the simple assumption of uncorrelated motion of the atoms which results in the description of the motion of all atoms in the bulk, and at the surface, by a single mean-squared displacement $<U^2>$. A trial was made by Jezequel et al.[67] to calculate Debye-waller factors with $<U^2>$ for each layer deduced from LEED measurements. White et al. [14,32] calculated W by weighting the bulk $<U^2>$ of each layer by $\exp[-z/\Lambda_e]$ where z is the perpendicular layer distance. Such trials showed that the temperature dependence of DT's could be reasonably described in such a way and suggest that the vibrational motion of the atoms is correlated.

Correlated vibrations of the atoms via phonons is expected to introduce non-direct transition intensity strongly localized around the direct transition, - contrary to the uncorrelated vibrations assumption - a result analogous to that for both electron [31] and X-ray [28,30] diffraction. This has also been concluded by Shevchik [7] via a theoretical analysis of angle resolved photoemission based upon a tight-binding initial state, APW final states, and sums over first-order phonon processes. The qualitative physical explanation for this, as reported by White et al. [14,32], is that " the most probable sets of phonon excitations are those for which local clusters of atoms are highly correlated in their motion (that is, for small phonon wave vector), thus preserving the original short-range translational symmetry and leading to transitions with approximatly DT character ".

Correlated vibrations are included in Sagurton's model (see Chapter II). The lack of success of Shevchik's model could be explained in terms of this latter analysis where the NDT component is found to depend on temperature and the temperature dependence of DT intensity is still described by the Debye-Waller factor Eq.(2-15).

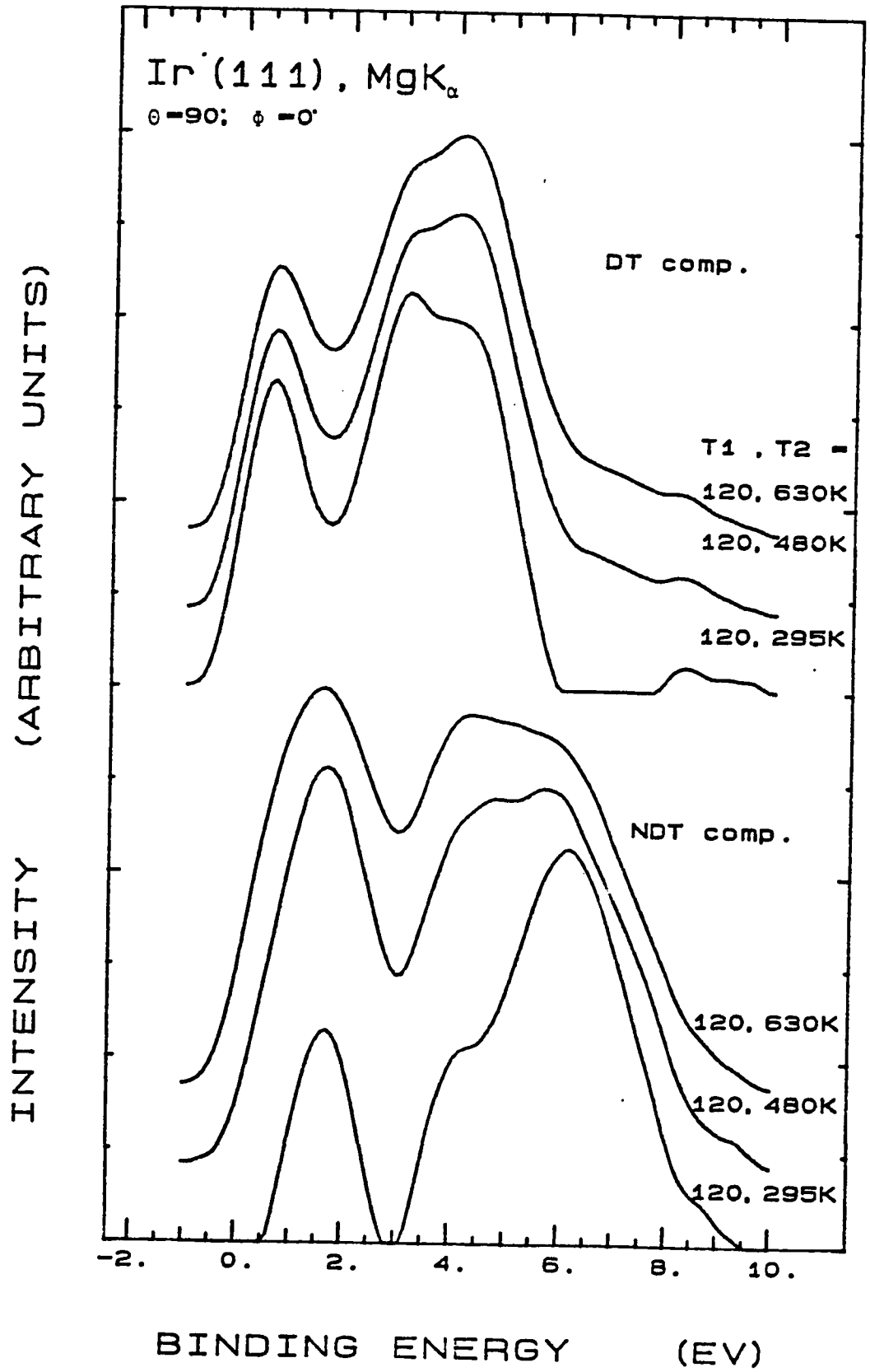

Fig. (*VI-16*): Direct and non-direct components isolated using various pairs of temperature dependent spectra obtained at $\theta = 90°$, $\varphi = 0°$ and high angular resolution $\alpha = \pm 1.1°$.

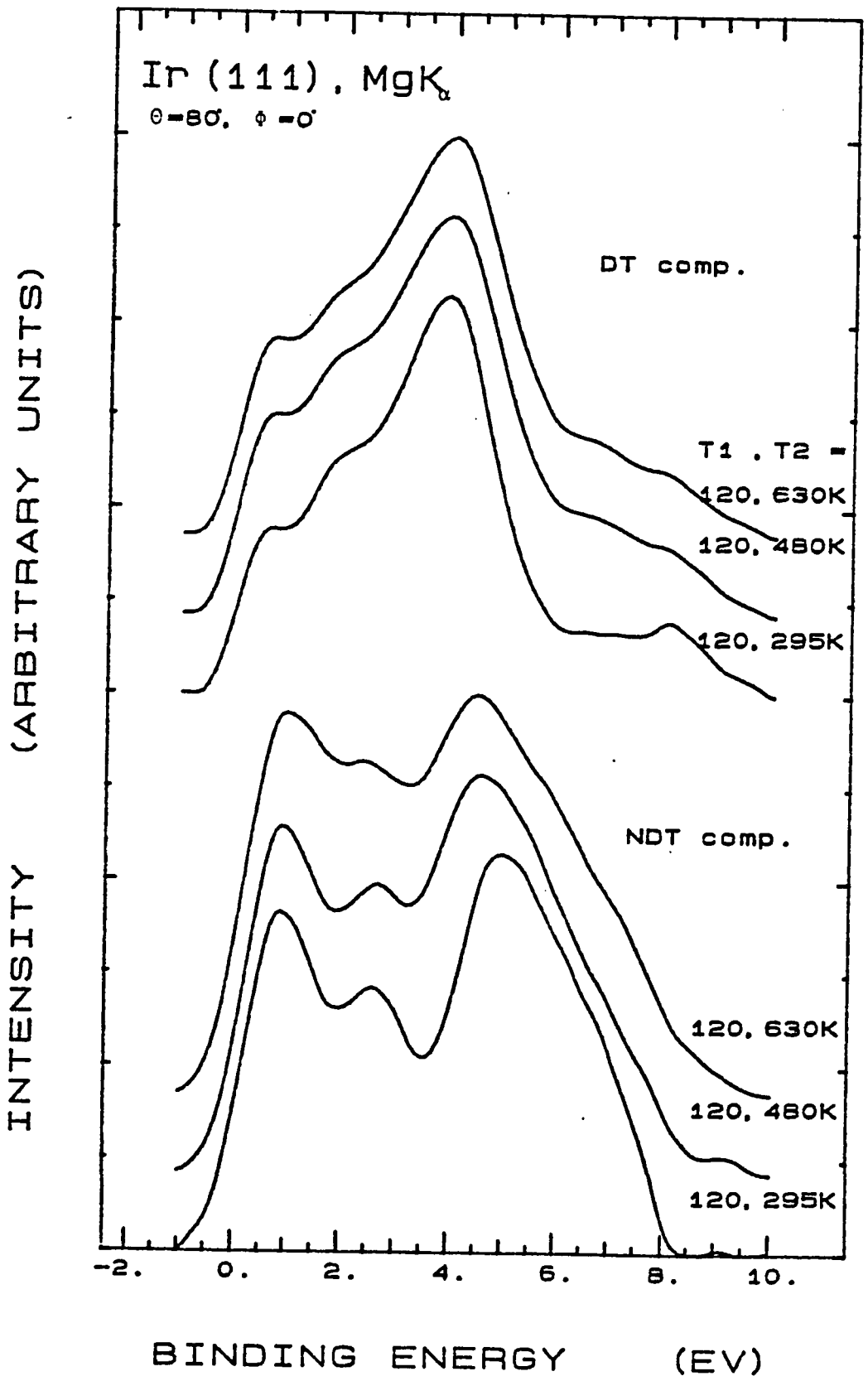

Fig. (*VI-17*): Direct and non-direct components isolated using various pairs of temperature dependent spectra obtained at $\theta = 80°$, $\varphi = 0°$ and high angular resolution $\alpha = \pm 1.1°$.

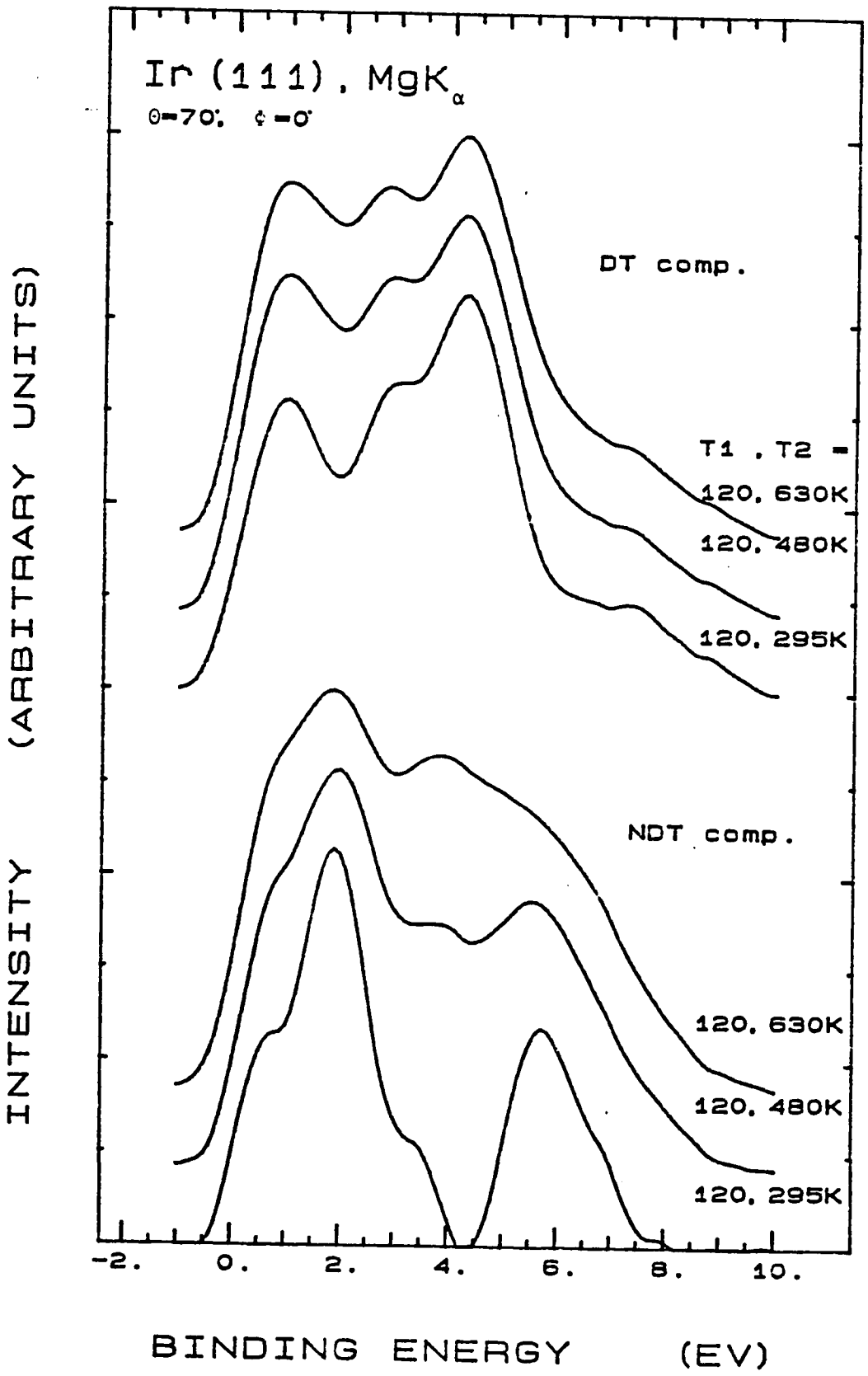

Fig. (*VI-18*): Direct and non-direct components isolated using various pairs of temperature dependent spectra obtained at $\theta = 70°$, $\varphi = 0°$ and high angular resolution $\alpha = \pm 1.1°$.

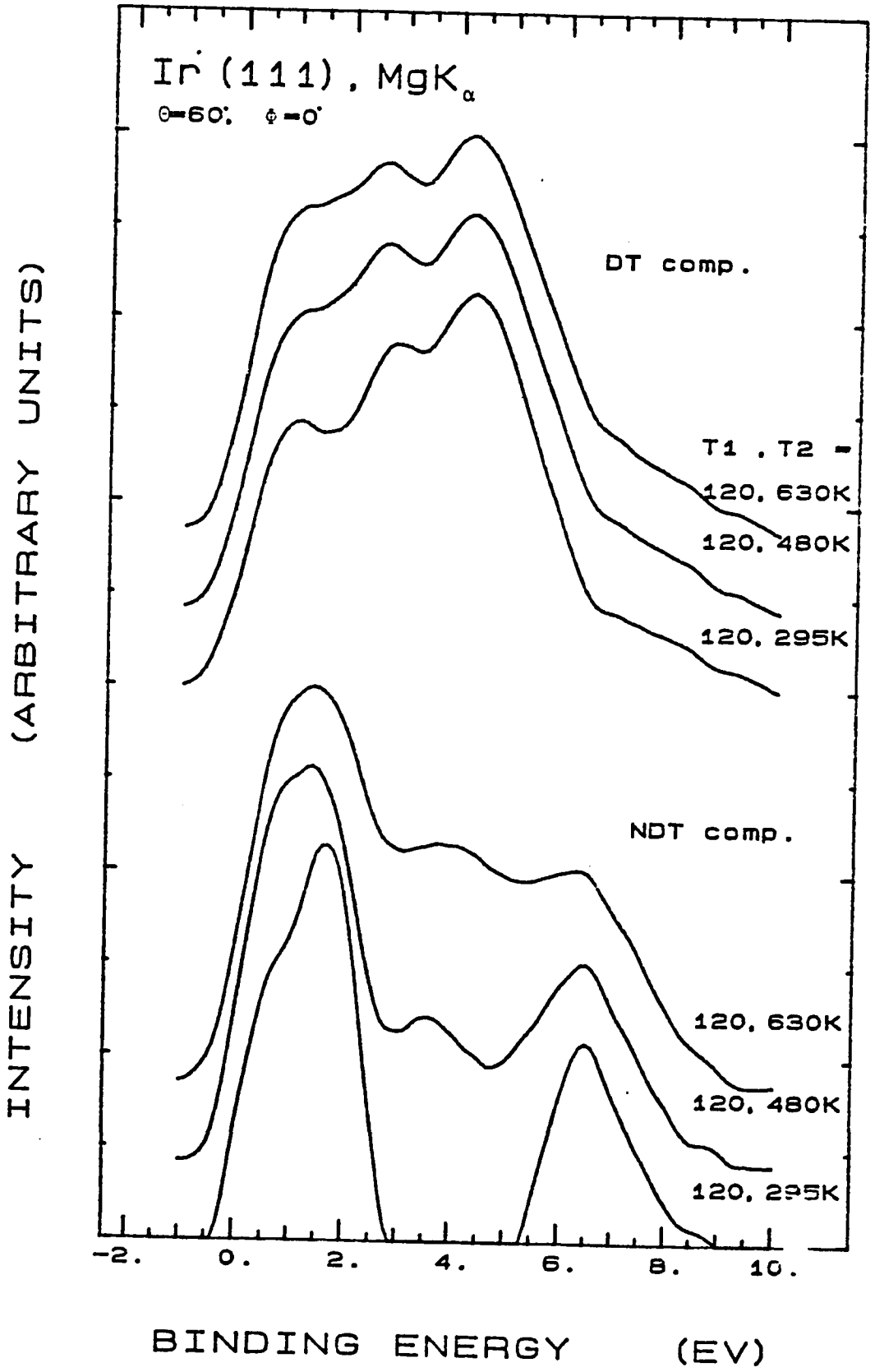

Fig. (*VI-19*): Direct and non-direct components isolated using various pairs of temperature dependent spectra obtained at $\theta = 60°$, $\varphi = 0°$ and high angular resolution $\alpha = \pm 1.1°$.

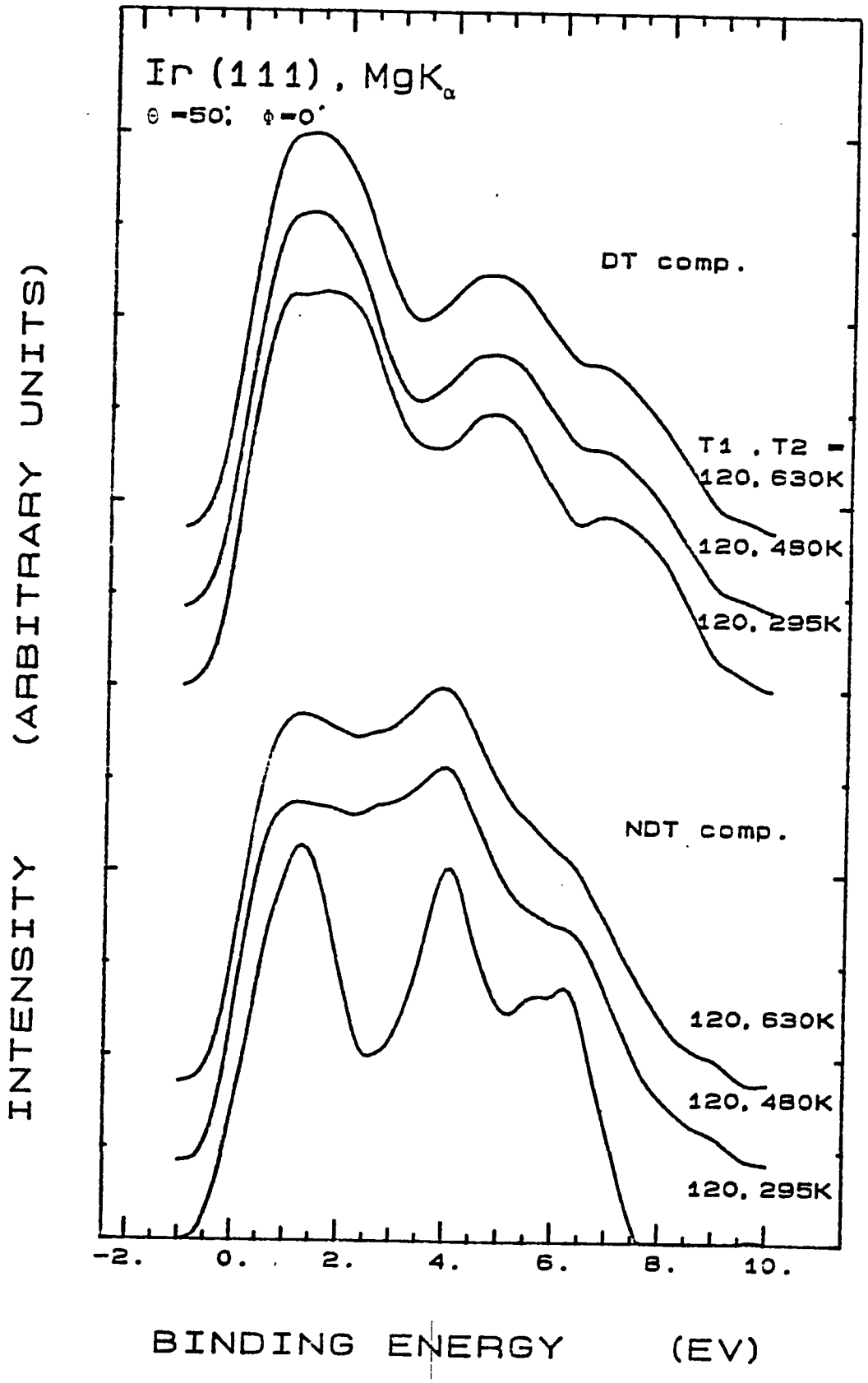

Fig. (*VI-20*): Direct and non-direct components isolated using various pairs of temperature-dependent spectra obtained at $\theta = 50°$, $\varphi = 0°$ and high angular resolution $\alpha = \pm 1.1°$.

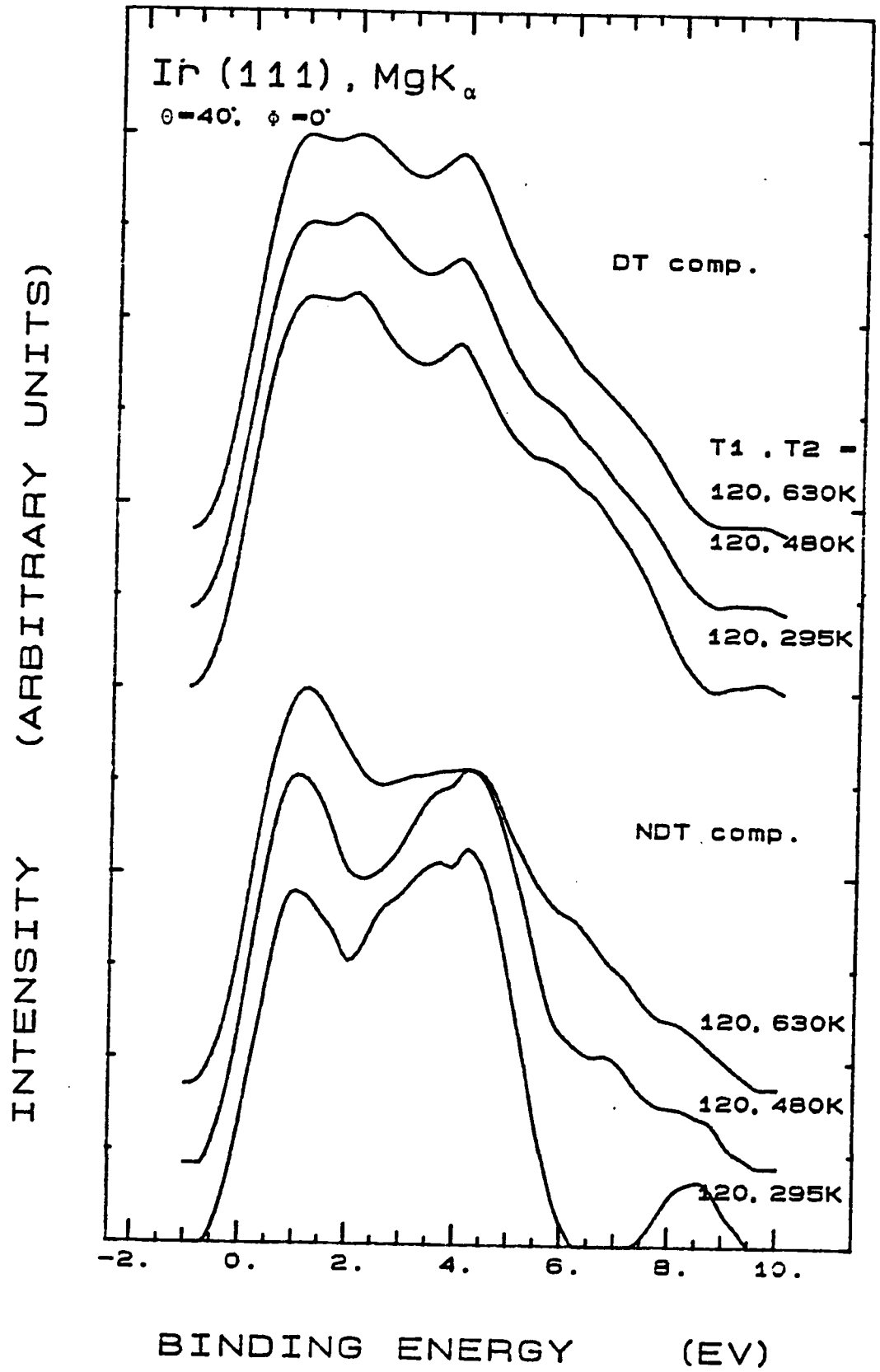

Fig. (*VI-21*): Direct and non-direct components isolated using various pairs of temperature dependent spectra obtained at $\theta = 40°$, $\varphi = 0°$ and high angular resolution $\alpha = \pm 1.1°$.

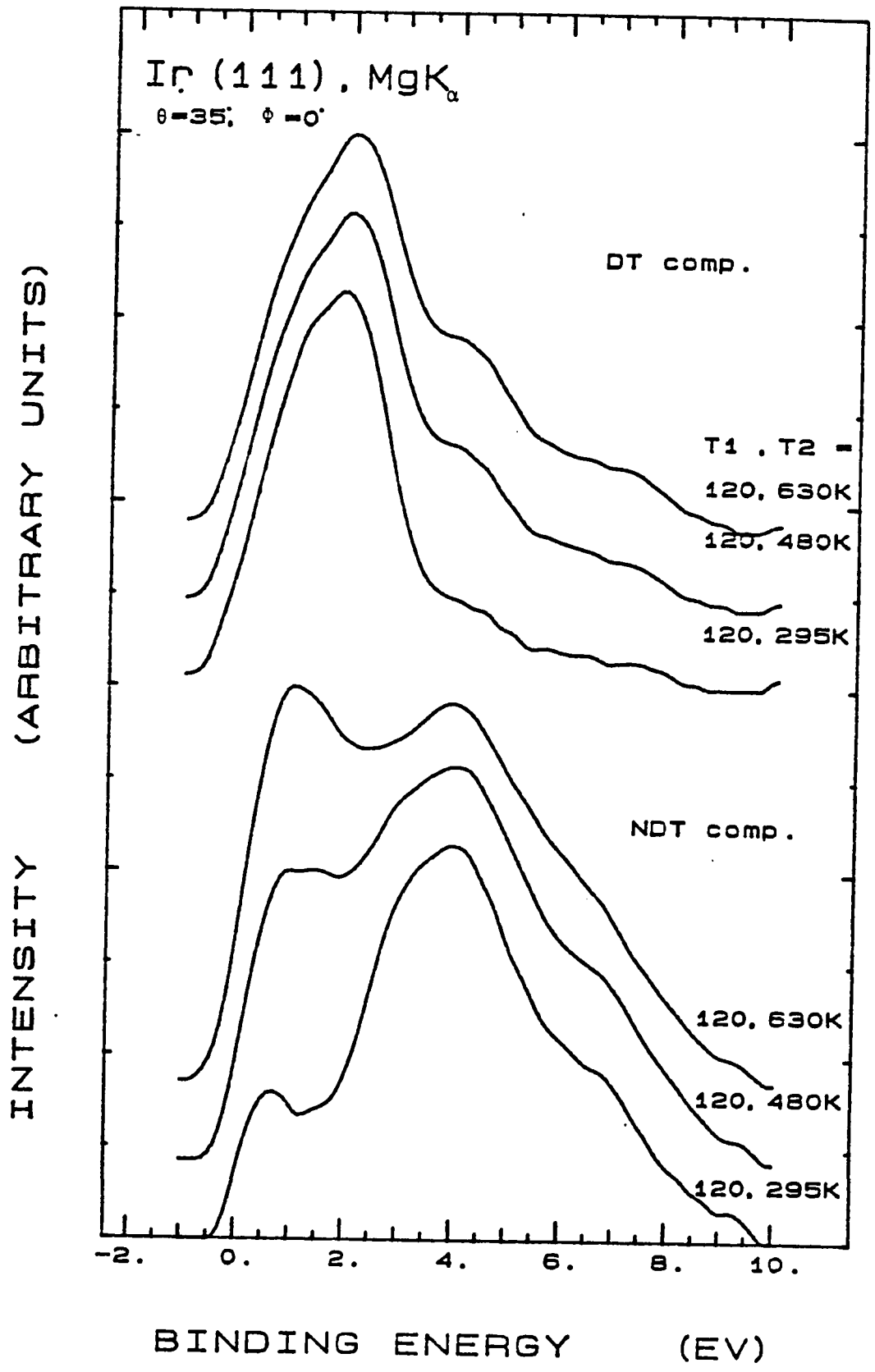

Fig. (*VI-22*): Direct and non-direct components isolated using various pairs of temperature dependent spectra obtained at $\theta = 35°$, $\varphi = 0°$ and high angular resolution $\alpha = \pm 1.1°$.

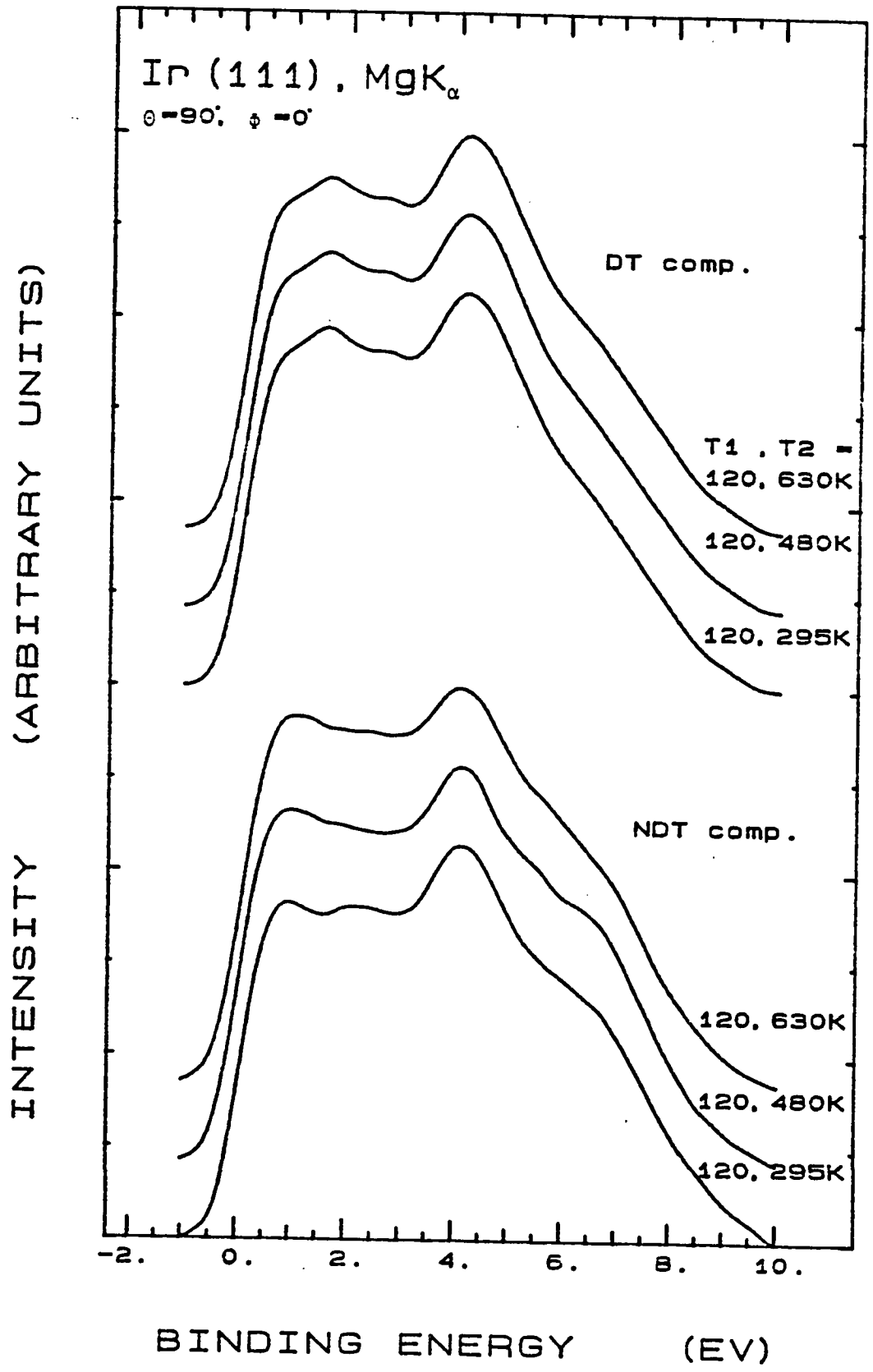

Fig. (*VI-23*): Direct and non-direct components isolated using various pairs of temperature dependent spectra obtained at $\theta = 90°$, $\varphi = 0°$ and low angular resolution $\alpha = \pm 6.0°$.

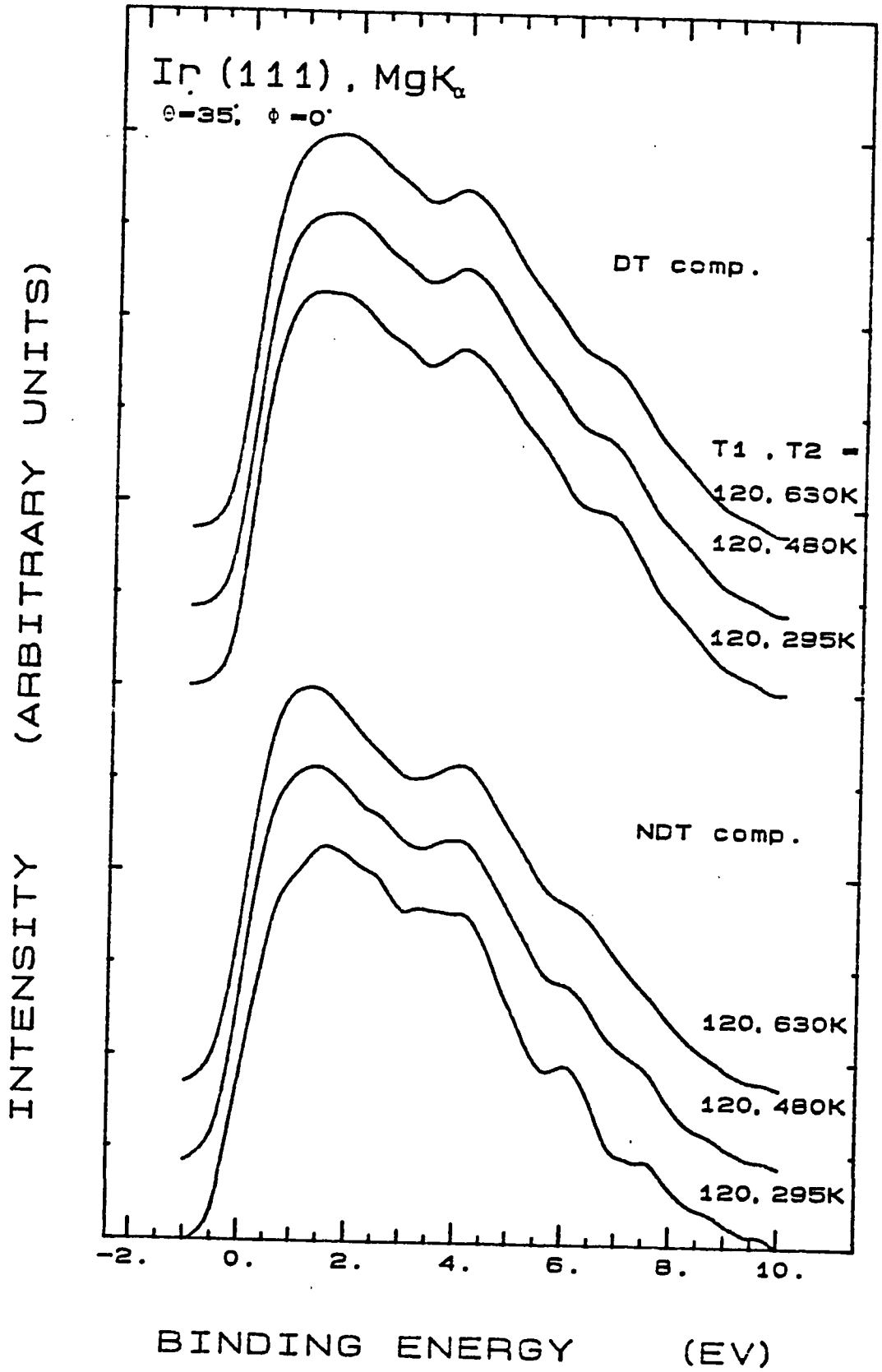

Fig. (*VI-24*): Direct and non-direct components isolated using various pairs of temperature dependent spectra obtained at $\theta = 40°$, $\varphi = 0°$ and low angular resolution $\alpha = \pm 6.0°$.

6.3 THEORETICAL COMPARISON:

In Figures (VI-25) through (VI-29) we show the temperature dependent Mg K_α excited experimental spectra from Ir(111) at (a)T = 630K or 295K and (b) at T = 120K, along with (c) the DT component extracted from the spectra in (a) and (b), and (d) the theoretical curve predicted by a pure DT model (see Chapter II) including the angular resolution broadening in $\vec{k}$. Also given in these figures are the corresponding emission angles for each region and the angular resolution α. All spectra are normalized to the same constant maximum height.

For the normal emission, $\theta = 90°$, Figure (VI-25), DT's originate from near the L point. Four peaks of almost equal intensities are predicted theoretically, these are labeled a,b,c and d at ~0.95, 3.4, 4.3 and 7.5 eV below Fermi level respectively. All four predicted peaks are found experimentally at T = 120K but with different intensities and with a small shift in the energy for the lowest binding energy peak (peak a) which is found at ~0.7 eV in (b) and (c). The energy positions of the two peaks b and c in the experimental spectrum at T = 120K, are at the same binding energy as predicted from the DT model in (d) with a small difference in their relative intensities but considerably broadened. This broadening is less in the experimental DT component than it is for the experimental data at 120K which suggests, when compared with (d), that there are still some NDT components included in the DT component in (c). At high binding energies where the theory predicts a pronounced peak, the experimental spectrum (b) only shows less pronounced feature.

The differences noted in peak intensities between theory and experiment could be explained by the fact that the transition matrix elements were assumed constant in the DT model. For example, the peak d has an sp wave kind character [6,64] and thus low cross-section at high excitation energy. This is in contrast to d-like character for peaks a, b and c which have larger cross-sections. As for the difference in the peak position of the lowest binding energy peak at 0.75 eV in (b) and (c) form theory in (d), there is a controversy about its real placement from previous works. This peak represent the first L point below the Fermi level which is labeled as L_{6^-} in the band structure (Figure (V-1)). Anderson [68] found the L_{6^-} peak to be at 0.54 eV, Arbman et al. [69] at 0.61eV and Van der Veen [6] at 1.0 eV in a more recent and precise mapping of the energy bands of Ir using synchrotron radiation in the range $8 \leq h\nu \leq 30$eV. It is also important to mention the finding by Van der Veen of peak which does not disperse with photon energy lying above the L_{6^-} point at 0.4eV. This feature was attributed to emission from sp like surface resonance state similar to surface states of some noble metals. In our case the cross section of such surface state or resonance is very small because of the high excitation energy used. Thus, one can attribute the difference in peak 'a' position in (c) and (d) to a discrepancy in the theoretical Ir band-structure.

From this region, we also note the big difference between the theoretical DT spectrum and room or higher temperatures spectra in figure (VI-1). Only the spectrum at T=120K shows all the predicted peaks especially the split between peaks b and c. This shows the importance of

phonon effects on the Iridium valence bands and suggests that any valence band mapping with high excitation energies should be done at cryogenic temperatures.

Figure (VI-26) where the polar emission angle is 10° smaller than in the previous region, almost all the features found experimentally are predicted by theory. We note here the similarity in the intensity of peak d at ~4eV which exhibit only a small shift in position that could be attributed to the theoretical Ir band structure. The other features are not well resolved experimentally but we can detect their positions that are similar to the ones predicted by theory but their relative intensities are not the same. Again one could attribute this discrepancy to the neglected matrix elements. The intensity of peak a and the relative position of the Fermi leved in (b) or (c) compared to (d) could be explained, like in the previous region by some discrepancies in the theoretical Ir band-structure.

Figure (VI-27) at polar angle of 70° shows good qualitative agreement between the shape predicted from theory and the DT component extracted from (a) and (b), the changes in the relative intensities of all components as well as in the energy positions of peaks a, b, d, and c. Only peak c is predicted with a shift of ~0.4eV toward lower binding energies. Peak c is also the highest peak in the experimental spectrum at T = 120K.

The striking resemblance of (c) and (d), together with similar resemblances in the previous regions, suggests that although a non-self consistency is found in Shevchik's NDT theory, the DT component

deconvoluted via his model gives a first approximation of the real DT component. The discrepancy found in the energy position of peak c could be attributed to the theoretical band structure of Ir. We also note here the differences between theory and experimental spectra taken at room temperature.

Figure (VI-28) further indicates the strikingly good agreement between theory and the DT component extracted from the two spectra (a) and (b). Again, peak c is shifted from experiment with the same amount as in the previous region. Peaks d and e are less resolved in the DT component spectrum. We note in this region the flat peak instead of two peaks a and b in the experimental spectrum at T=120K and the big differences between spectra (a) at room temperature and (d) theory. The nonappearance of peaks d and e in the lowest temperature spectrum (b) shows that even at T=120K there are still important NDT components. The DT component from Shevchik's model gives a good assessment of all the theoretical DT features.

As the emission angle decreases, we noted some discrepancies between the theoretical DT spectrum and the experimental spectra or the extracted DT component. Figure (VI-29) shows an example of such discrepancies at $\theta = 40°$. Although peaks a, b, c, and d can be seen from the experimental spectra, there are other features, in the experimental spectra that are not predicted by the theory. These are the appropriate Fermi level position, the valley between peaks a and b which is completly filled in the experimental

spectra and a feature at ~6eV which is not predicted theoretically. One could attribute these discrepancies to either strong phonon effects in such regions that are near the (001) direction or to discrepancies in the theoretical Ir energy bands. In such low emission angles we should also consider the effect of surface refraction as the photoelectron goes through the surface barrier. Such effect, although, is more significant at emission angles below ~10°-15° (with respect to the sample surface), could affect the photoemission valence-band spectra.

We should mention here that our present work is the first verification of the theoretical valence band data reported by J. Noffke et al. The authors compared their results with previous experiments on the Ir valence band at some high symmetry points only. Another effect which is not included in the DT model used, is the smearing effect in k_f which limits the wave function to a region of the order of the mean free path Λ_e along its propagation direction. This broadening may become significantly important as the surface sensitivity increases. Such an effect, although is negligible in XPS (see Chapter II) and found not to affect the theoretical broadening for Tungsten [10], do not seem to have the same role in the case of Iridium. The Iridium valence band might be sensitive to such longitudinal broadening along the k_f direction and thus should be included in the theoretical calculations in future work on the same element.

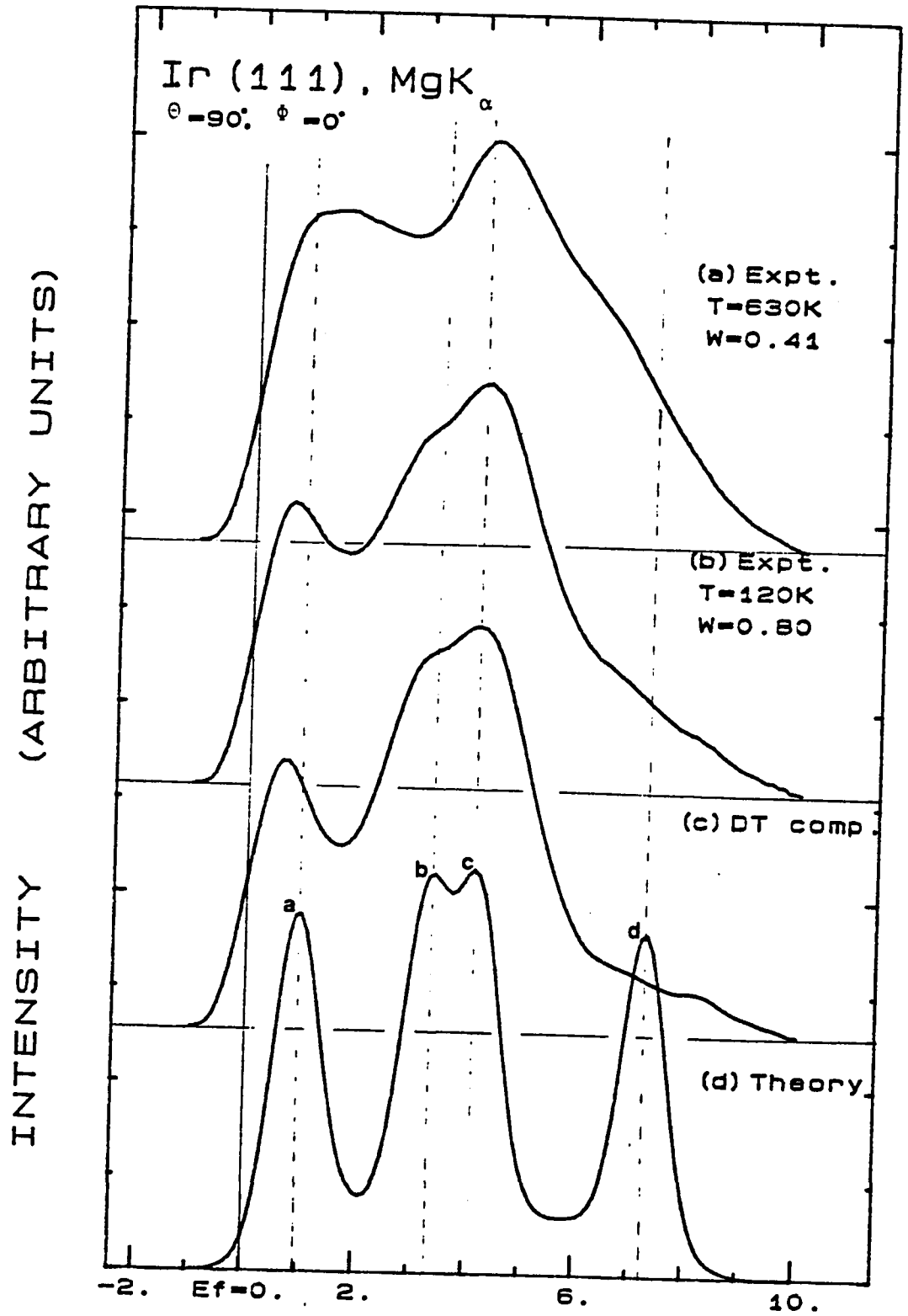

Fig. (*VI-25*): Temperature dependent Mg K_α excited experimental spectra from Ir(111) at $\theta = 90°$, $\varphi = 0°$ and $\alpha = \pm 1.1°$, obtained at temperatures (a) T = 630K and (b) at T = 120K. (c) the DT component extracted from the spectra in (a) and (b). (d) the theoretical curve predicted by a pure DT model allowing only angular resolution broadening in $\vec{k}$. Simple DT's here originate from near the L point .

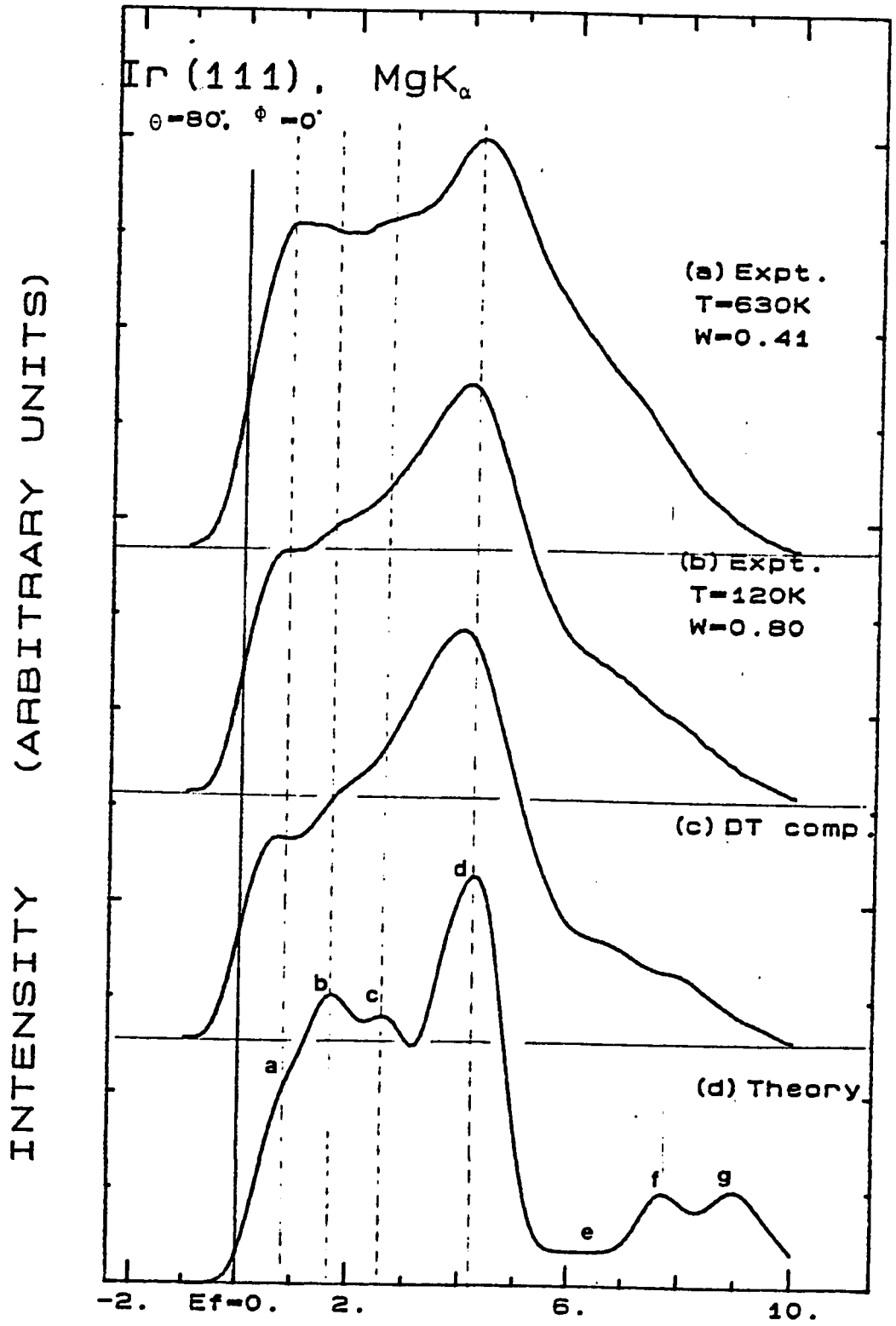

Fig. (*VI-26*): Temperature dependent Mg K_α excited experimental spectra from Ir(111) at $\theta = 80°$, $\varphi = 0°$ and $\alpha = \pm 1.1°$, obtained at temperatures (a) T = 630K and (b) at T = 120K. (c) the DT component extracted from the spectra in (a) and (b). (d) the theoretical curve predicted by a pure DT model allowing only angular resolution broadening in E.

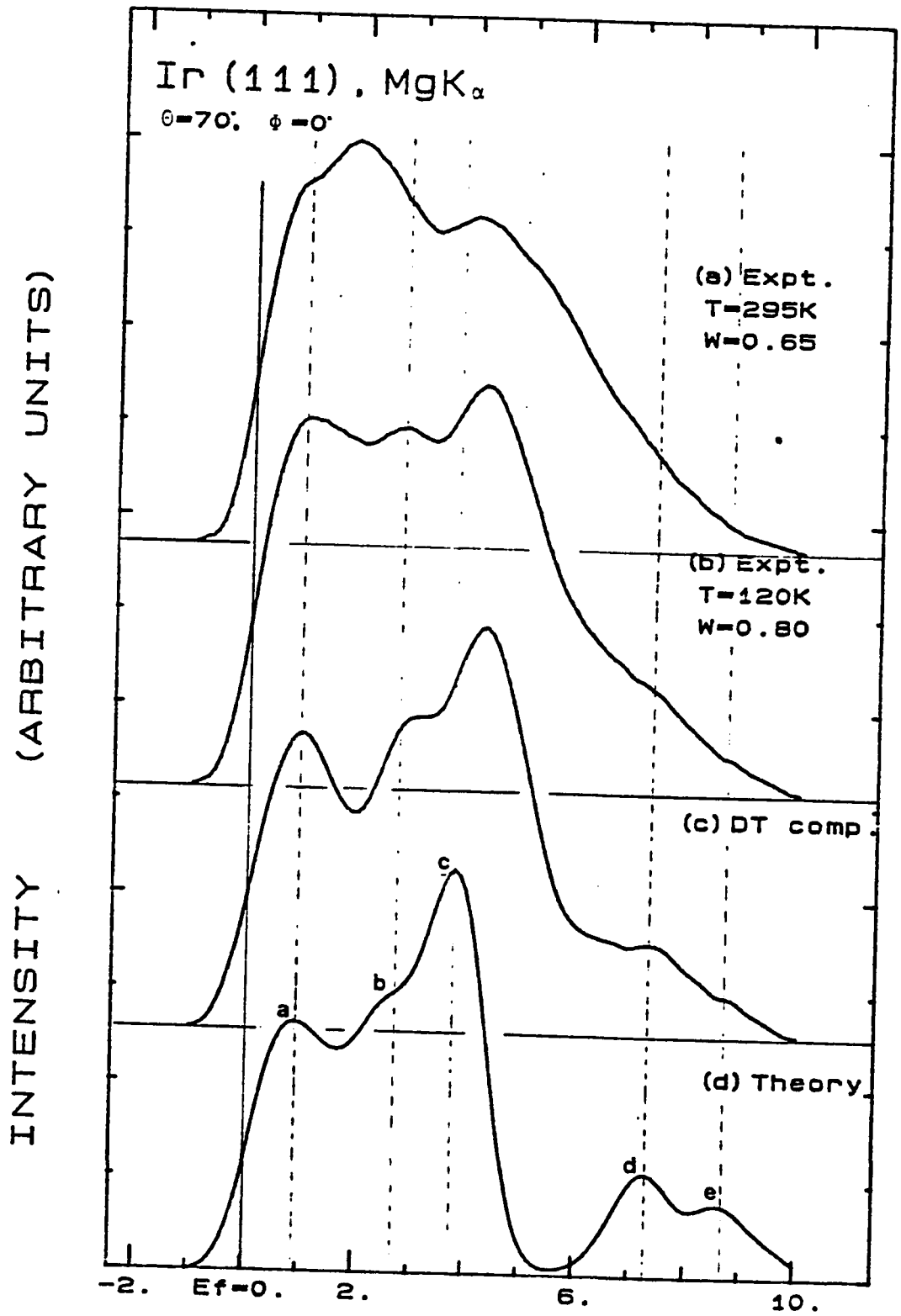

Fig. (VI-27): Temperature dependent Mg K_α excited experimental spectra from Ir(111) at $\theta = 70°$, $\varphi = 0°$ and $\alpha = \pm 1.1°$, obtained at temperatures (a) T = 295K and (b) at T = 120K. (c) the DT component extracted from the spectra in (a) and (b). (d) the theoretical curve predicted by a pure DT model allowing only angular resolution broadening in K.

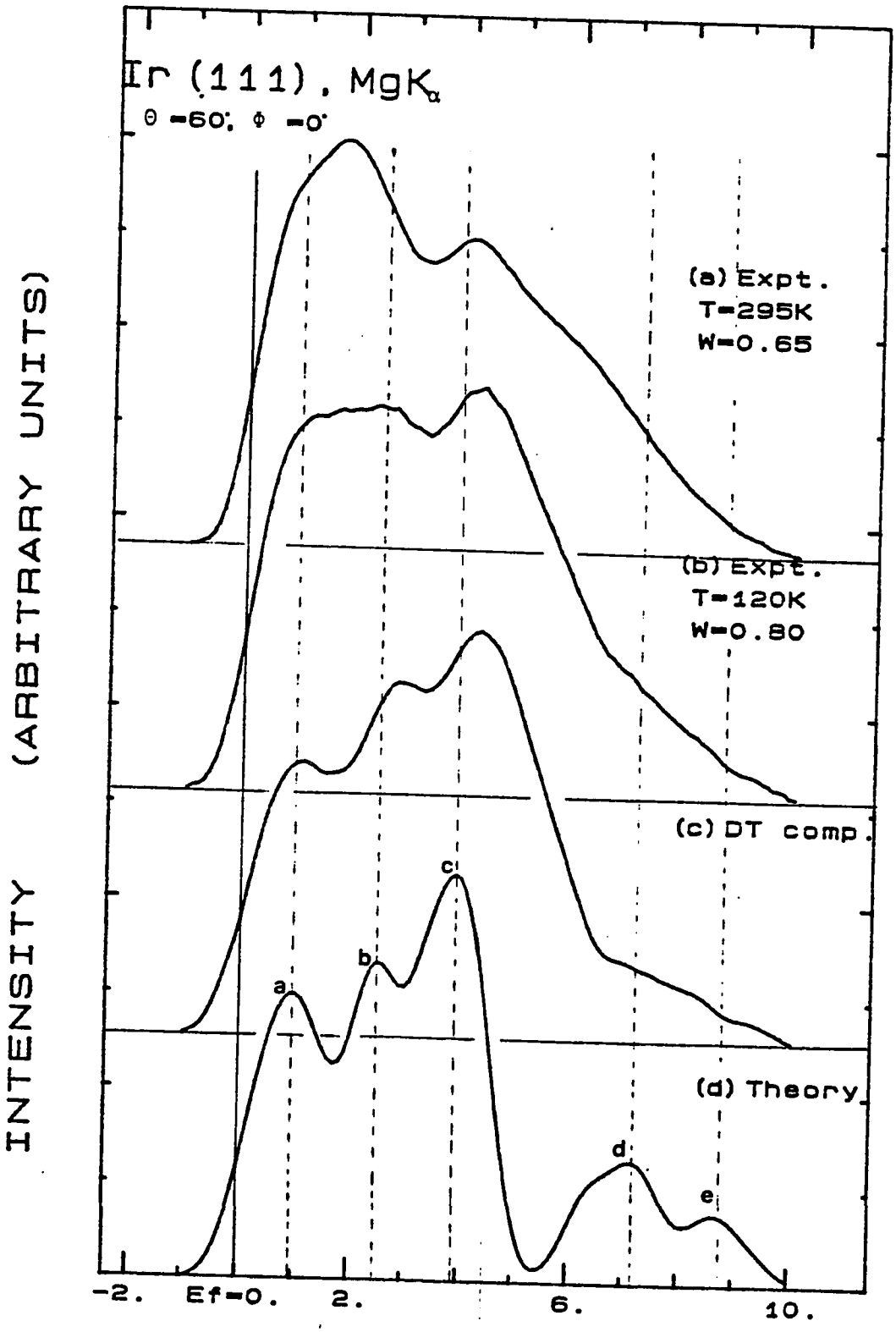

Fig. (*VI-28*): Temperature dependent Mg K_α excited experimental spectra from Ir(111) at $\theta = 60°$, $\varphi = 0°$ and $\alpha = \pm 1.1°$, obtained at temperatures (a) T=295K and (b) at T=120K. (c) the DT component extracted from the spectra in (a) and (b). (d) the theoretical curve predicted by a pure DT model allowing only angular resolution broadening in $\vec{k}$.

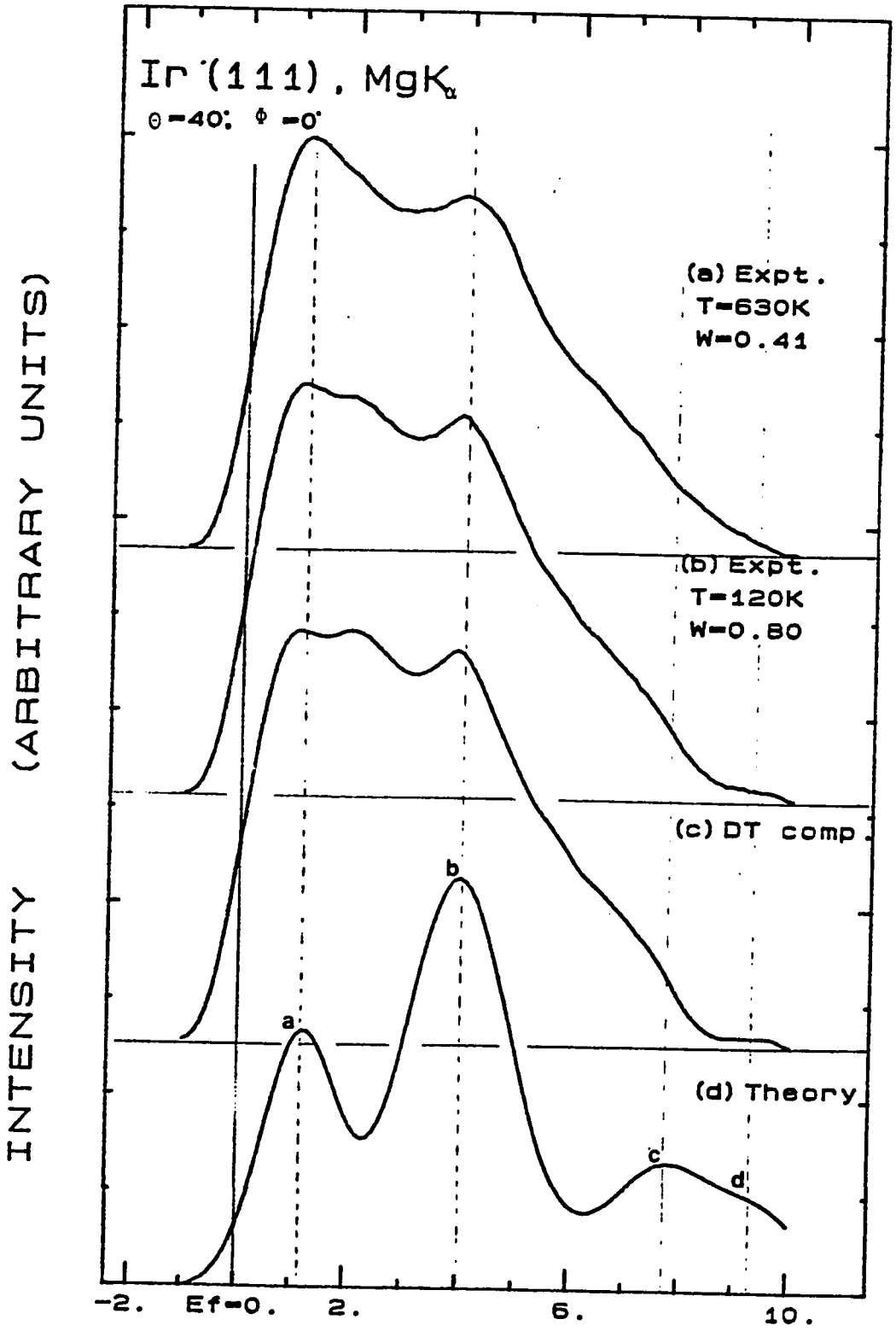

Fig. (VI-29): Temperature dependent Mg K_α excited experimental spectra from Ir(111) at $\theta = 40°$, $\varphi = 0°$ and $\alpha = \pm 1.1°$, obtained at temperatures (a) T = 630K and (b) at T = 120K. (c) the DT component extracted from the spectra in (a) and (b). (d) the theoretical curve predicted by a pure DT model allowing only angular resolution broadening in

CHAPTER VII

CONCLUSIONS

In conclusion, we have found that Iridium valence-bands are very sensitive to temperature variation. Spectra taken at T=120K show dramatic changes when compared to higher temperature spectra. Only spectra taken at this low temperature show similar changes to the ones predicted by theory. Therefore, any accurate mapping of the energy bands of Iridium should be done at cryogenic temperatures.

The decomposition of the temperature dependent valence band spectra into direct end non-direct components via the non-direct transition model of Shevchik is found not to give full self consistency in all the results. Non-direct transition components, deconvoluted via this model are found to be different from the density of state of the crystal contrary to prior reported work. The DT components, however, are found to give good quantitative fit of the theoretical curves obtained from a simple DT model. These results are in accordance with the more accurate theoretical model by Sagurton where the temperature dependence of the DT intensity is also

described by Debye-Waller factor and the NDT component is temperature dependent. Our work suggests that the DT component extracted via Shevchik's model should not be much different from the one predicted by Sagurton and could be taken as a first approximation of the real DT component.

In order to better understand the NDT due to phonon effects, it is of interest in future studies to follow the temperature dependence of the valence band spectra step by step from liquid Helium temperatures to very high temperatures. This would permit verification of Sagurton's model conclusion on the peaking of NDT around DT.

The simple direct-transition model, based on a free-electron final state dispersion relation and constant matrix elements for all allowed transitions, is found to give a first order description of the changes of the lowest temperature spectra. However, inclusion of matrix elements and elastic scattering broadening effects might give better description of all spectral features.

Appendix I

Debye-waller factor

Debye-Waller factor arose originally in connection with X-ray diffraction. It governs the temperature and energy dependence of the intensity of elastically scattered radiation by a crystal lattice. It is thus a measure of the effect of thermal motion in reducing the apparent distortion of the lattice. It is given by:

$$W(T) = EXP\,(-\Delta\vec{k}^2 < U^2(T) >)$$

where $\Delta\vec{k}$ is the difference between the incident (initial) and scattered (final) wave-vectors which is taken to be equal to a vector $\vec{g}$ in the reciprocal lattice vector which is involved in direct transition. $< U^2(T) >$ is the temperature dependent mean squared atomic displacement of the atoms from their ideal position as a result of thermal motion. For a cubic lattice $< U^2(T) >$ is given by (R. C. James, The Optical Principles of Diffraction of X-rays) :

$$< U^2(T) > = \frac{3\hbar^2}{mk_B}\,\frac{T}{\Theta^2_D}\,[\Phi(\frac{\Theta_D}{T}) + \frac{1}{4}\,\frac{\Theta_D}{T}]$$

where :

m is the mass of a lattice point

Θ_D is the Debye temperature

and $\Phi(x)$ is the Debye integral :

$$\Phi(x) = \frac{1}{x} \int_0^x \frac{y}{e^y - 1} dy$$

REFERENCES

1. E. G. M. Cordona and L. Ley (Eds),
Photoemission in solids, vols 1 and 2, Springer-Verlag, Berlin, (1981).

2. D. A. Shirley, J. Stohr, P. S. Wehner, R. S. Williams, and G. Apai,
Phys. Scripta 16 , (1977) 398.

3. Z. Hussain, C. S. Fadley, S. Kono, and L. F. Wagner,
Phys. Rev. B 22 , (1980) 3750.

4. Z. Hussain, E. Umbach, J. J. Barton, J. G. Tobin and D. A. Shirley,
Phys. Rev. B 25 , (1982) 672.

5. Z. Hussain, S. Kono, R. E. Connelly, and C. S. Fadley,
Phys. Rev. Letters, 44 , (1980) 895.

6. J. F. Van der Veen, F. J. Himpsel, and D. E. Eastman
Phys. Rev. B 22 (1980) 4226.

7. N. J. Shevchik,
J. Phys. C 10 , (1977) L 555;
Phys. Rev. B 16 , (1977) 3428 ;
Phys. Rev. B 20 , (1979) 3020 .

8. R. S. Williams, P. S. Wehner, J. Stohr, and D. A. Shirley,
Phys. Rev. Letters, 39 , (1977) 302.

9. Z. Hussain, S. Kono, L. G. Petersson, C. S. Fadley, and L. F. Wagner,
Phys. Rev. B 23 , (1981) 724.

10. R. C. White, C. S. Fadely, M. Sagurton and Z. Hussain,
Phys. Rev. B 34 , (1986) 5226.

11. R. J. Baird, C. S. Fadely, and L. F. Wagner,
Faraday Discuss. Chem. Soc. 60 , (1975) 143

12. R. J. Baird, C. S. Fadely, and L. F. Wagner,
Phys. Rev. Letters, 37 , (1976) 111

13. M. Sagurton,
(unpublished results, a brief summary of this work is presented in Ref.14)

14. R. C. White, C. S. Fadely, M. Sagurton, P. Roubin, D. Chandersis, J. Lecante, C. Gunillot, and Z. Hussain,
Phys. Rev. B 35 , (1987) 1147.

15. C. N. Berglund and W. E. Spicer,
Phys. Rev. 136 A (1964) 1030.

16. B. Feuerbucher, B. Fitton, and R. F. Willis, eds,
Photoemission and the Electronic Properties of Surfaces Wiley, NY (1978)

17. E. W. Plummer and W. Eberhardt, eds,
Angle-Resolved Photoemission, Advances in Chemical Phys. 49 , (1981) 533

18. N. V. Smith,
Phys. Rev. B 3 , (1971) 1892.

19. D. E. Eastman in ***Electron Spectroscopy.*** Proc. of the Int. conf. Asilomar (Calif.). (ed. D.A.Shirley). (Sept. 1971), North Holland, Amsterdam (1972).

20. C. S. Fadley,
Prog. Surf. Sci, 16 , (1984) 275.

21. G. D. Mahan,
Phys. Rev. B 2 , (1970) 4334.

22. P. J. Feibelman and D. E. Eastman,
Phys. Rev. B 10 , (1974) 4932.

23. L. F. Wagner, Z. Hussain, and C. S. Fadley,
Solid State commun., 21 , (1977) 257.

24. L. G. Petersson, Z. Hussain, S. Kono, and C. S. Fadley,
Solid State commun., 34 , (1980) 549.

25. J. Stohr, P. S. Wehner, R. S. Williams, G. Apai, and D. A. Shirely,
Phys. Rev. B 17 , (1978) 587.

26. T. C. Chiang, J. A. Knapp, M. Kono, and D. E. Eastman,
Phys. Rev. B 21 , (1980) 3513.

27. H. Martensson,
Phys. Rev. B 27 , (1983) 4492.

28. B. F. Warren,
X-Ray Diffraction, Addison Wesley, NY, (1969) 159-169.

29. J. B. Pendry,
Low Energy Electron Diffraction, Academic Press, NY, (1974)

30. R. W. James,
The Optical Principles of The Diffraction of X-rays
University Press, Glasgow, (1954) 193-228.

31. J. T. Mckinney, E. R. Jones, and M. B. Webb,
Phys. Rev. 160 , (1967) 523.

32. R. C. White, C. S. Fadely, M. Sagurton, P.Roubin, D. Chandesris, J. Lecante, C. Guillot and Z. Hussain
Solid State commun., 59 , N. 9, (1986)

33. C. Kittel,
Introduction to solid state physics, 6th edn. Wiley, NY (1986)

34. C. S. Fadley,
Review in *Electron Spectroscopy: Theory, Techniques and Applications*, C.R.Brundle and A.D.Baker, eds. Academic Press, London (1978) vol.2, ch.1.

35. C. S. Fadley,
Review of Angle Resolved X-ray Photoelectron Spectroscopy in Prog. in Surf. Sci., edt. S.G.Davidson, Pergamon Press, New York, 16 (1985) , N. 3.

36. A. Einstein,
Ann.Phys. 17 , (1905) 132.

37. M. P. Seah and W. A. Dench,
surf. Interface Anal, 1 , (1979) 2.

38. J. A. Strozier Jr..D. W. Jesper,and F. Jona,
Surface Physics of Materials, edited by J. M. Blakely, Academic Press, New York (1975).

39. M. A. Van Hove and S. Y. Tong,
Surface crystallography by LEED, Springer Verlag, Berlin (1979).

40. M. Sagurton, E. L. Bullock, and C. S. Fadley,
Surf. Sci. 182 , (1987) 274.

41. J. J. Barton and D. A. Shirley,
Phys. Rev. B 32 , (1985) 1892.

42. J. J. Barton, S. W. Robey and D. A. Shirley,
Phys. Rev. B 34 , (1986) 778.

43. S. D. Kevan, D. H. Rosenblatt, D. Denly, B. C. Lu and D. A. Shirley,
Phys. Rev. Lett. 41 (1978) 1565.

44. S. Kono, C. S. Fadly, N. F. T. Hall and Z. Hussain,
Phys. Rev. Lett. 41 (1978) 117.

45. C. S. Fadley, S. Kono, L. G. Petersson, S. M. Goldberg, N.F.G.Hall, J.T.Lloyd and Z.Hussain,
Surf. Sci. 89 , (1979) 52.

46. R. J. Baird, C. S. Fadley, and L. F. Wagner,
Phys. Rev. B 15 , (1977) 666.

47. *A Modern Photoelectron spectrometer With Multi-Techniques Surface Analysis Capability.* A report prepared by Electron spectroscopy Group in Department of Physics, University of Petroleum and Minerals, Dhahran, K. S. A (1986)

48. C. E. Kuyatt and J. A. Simpson,
Rev.Sci.Instrum, 38 (1967) 103.

M. P. Seah,
Review in *Surf. Interface Anal.*, 2 (1980) 222

R. C. G. Leckey,
J. Electron Spectrosc. Relat. Phenom., 43 (1987) 183.

49. M. T. Anthony and M.P.Seah,
Surf.Interface Anal., 6 (1984) 95

50. D. Briggs and P. M. Seah,
Practical Surface Analysis by Auger and X-ray Photoelectron Spectroscopy, John Willey & Sons, Chichester, U.K.(1983).

51. V. V. Nemoshkalenko and V. G. Aleshin,
Electron spectroscopy of crystals, Plenum, New York, (1979).

52. M. Owari, M. Kudo, Y. Nihei and H. Kamada,
J.Electron Spectrosc. Relat. Phenom., 22 (1981)

53. S. D. Kevan,
Rev. Sci. Instrum., 54 (1983)1441.

54. G. K. Ovrebo and J. L. Erskine,
J.Electron spectrosc. Relat. Phenom., 24 (1981)189.

55. R. C. White, C. S. Fadley and R. Trehan,
J. Electron spectrosc. Relat. Phenom., 41 (1986)95.

56. C. M. Chan, S. L. Cunningham, M. A. Van Hove, W. E. Weinberg. and S. P. Withrow
Surf. Sci., 66 , (1977), 394.

57. J. T. Grant,
Surf. Sci. 25 , (1971) 451

58. J. Kuppers and A. Plagge,
J. Vac. Technol., 13 , (1976) 258

59. J. C. Faggle and N. Martensson, *Core-level Binding Energies in Metals*, J. Electronic Spectrosc. Relat. Phenom. 21 , (1980) 275 G. E. Muilenberg (Edt.). Perkin-Elmer Corporation.

60. D. A. Shirley,
Phys. Rev. B 5 ,(1972) 4709

61. A. Procter and P. M. A. Sherwood
Analytical Chemistry 54 ;(1982) 13

62. A. Savitzky and M. J. E. Golay
Anal. Chem. 36 ; (1964) 1627-1639 corrected in:
J. Steiner, Y. Termonia, and J. Deltour
Analytical Chemistry 44 ; (1972)1906-1909

63. A. Procter and P. M. A. Sherwood
Analytical Chemistry 52 : (1980)2315-2321

64. J. Noffke and L. Fritsche,
J. Phys. F. (Met. Phys.), 12 (1982) 921-33

65. G. A. Burdick,
Phys. Rev. 129 , (1963) 138.

66. N. V. Smith, G. K. Werthim, S. Hufner, and M. M. Traum
Phys. Rev. B 10 (1974) 3197.

67. G. Jezequel, A. Barski, P. Steiner, F.Solal, P. Roubin, R. Pinchaux and Y. Petroff
Phys. Rev. B 30 (1984) 4833.

68. O. K. Anderen
Phys. Rev. B 2 (1970) 883.

69. G. O. Arbman and S. Hornfelt
J. Phys. B 2 (1972) 1033.